

The Pennsylvania State University
The Graduate School

**STUDY OF UTILIZING INDUCTION HEATING TO MODULATE THE
BURNING RATE OF SOLID FUELS AND PROPELLANTS**

A Thesis in
Mechanical Engineering

by
Kirstin A. Walz

© 2024 Kirstin A. Walz

Submitted in Partial Fulfillment
of the Requirements
for the Degree of

Master of Science

May 2024

The thesis of Kirstin A. Walz was reviewed and approved by the following:

Dr. Richard Yetter
Professor of Mechanical Engineering
Thesis Advisor

Dr. Jacqueline O'Connor
Professor of Mechanical Engineering

Mary Frecker
Riess Chair of Engineering, Director of the Penn State Center for
Biodevices, and Professor
Head of the Mechanical Engineering Department

ABSTRACT

Solid rocket motors exhibit predetermined thrust profiles governed by propellant composition, burning surface geometry, and motor conditions. There is a desire to have throttleable solid rocket motors for trajectory optimization, multi-purpose capabilities, and improved energy management by controlling thrust and pressure. Currently employed methods modulate thrust output via mechanically operated pintle valves. However, these techniques are limited by control system accuracy and response time. Another means of modulating solid propellant burning rate is wired propellants, which offer custom or improved performance, but the mission profile's adaptability and heating uniformity could be improved. Some efforts have been made to investigate the application of an electric field to both gas phase flames and solid phase propellants/fuels to modulate burning rate. Results have found both increases and decreases, however, the mechanisms behind the changes in burning rate are not yet fully understood. Other active research initiatives investigate using microwave frequencies to enable burning rate modulation in propellant strands. However, microwave penetration depth is limited due to the high frequency and microwave coupling mechanism, thus limiting the heating uniformity at larger scales. This study investigates the use of induction heating (IH) to dynamically control solid propellant burning rate. Induction heaters utilize magnetic fields generated by a coil driven by a radio wave frequency (RF) alternating current. IH has two heating mechanisms relevant to this application: magnetic hysteresis heating and the Joule effect (eddy current heating). Both mechanisms are investigated by this study. Fuel and propellant samples with embedded magnetic nanoparticles (MNPs) were developed to observe the effects of magnetic hysteresis. Samples with embedded wires were used to look at eddy current heating. Thermal imaging was used to measure surface temperature of the fuel samples and raw MNP powders to characterize the relative magnetic hysteresis heating potential of a few select MNP susceptors. Results showed that the 30nm magnetite (Fe_3O_4) particles provide the most relative heating via magnetic hysteresis, and 0.64mm diameter aluminum wires provide the most significant relative heating via the Joule effect. Further analysis of the magnetic hysteresis heating data shows that susceptor particle size can control the sample heating rate. The sample's initially high heating rate slowed as temperature increased because the smaller particles reached a limit where their Néel relaxation time became less than the induction heater frequency, resulting in reduced heating efficiency. Propellant samples with embedded MNPs, heated via magnetic hysteresis, were found to exhibit a change in sample density due to the introduction of porosity thought to be caused by the dissociation of urethane bonds. Burning rate tests were performed on the propellant samples with embedded MNPs to observe dynamic changes in the burning rate when IH was applied. The results of burning rate testing found an average increase in burning rate of 131% through the heated section of the propellant sample. This result proves a significant change in burning rate can be achieved after ignition of a solid propellant grain has

occurred. It is proposed that the large increase in burning rate is attributed to both the temperature sensitivity of the propellant and the increased burning surface area due to the induced porosity.

TABLE OF CONTENTS

LIST OF FIGURES	vii
LIST OF TABLES	xii
LIST OF ABBREVIATIONS	xiii
ACKNOWLEDGMENTS	xiv
 CHAPTER 1: INTRODUCTION.....	 1
1.1 MOTIVATION	1
1.2 OBJECTIVES.....	2
1.3 THESIS ORGANIZATION	2
 CHAPTER 2: LITERATURE REVIEW.....	 4
2.1 OVERVIEW OF SOLID PROPELLANTS AND FUELS.....	4
2.1.1 Solid Propellant Grain Classification and Manufacturing	4
2.1.2 Solid Fuel Grain Applications and Manufacturing	5
2.1.3 Burning Rate Pressure and Temperature Sensitivity.....	5
2.2 CURRENT ATTEMPTS AT CONTROLLING OR THROTTLING SOLID FUELS AND PROPELLANTS.....	8
2.2.1 Pintle Valves	8
2.2.2 Wired Fuels and Propellants	10
2.2.3 Applied Electric Field	11
2.2.4 Microwave Enhancement.....	13
2.3 INDUCTION HEATING THEORY	14
2.4 COMSOL MODELING	18
 CHAPTER 3: METHODS	 19
3.1 SAMPLE PREPARATION	19
3.1.1 Characterization of Magnetic Nanoparticles (MNP).....	19
3.1.2 Fuel Sample Formulations	21
3.1.3 Propellant Sample Formulations	22
3.1.4 Mixing and Casting Process.....	23
3.2 EXPERIMENTAL SETUP.....	26
3.2.1 Heating Test Setup	26
3.2.2 MNP Propellant Burning Rate Experimental Setup.....	29
3.3 COMSOL MODEL SETUP.....	31
3.3.1 Magnetic Field Generated by MTI Coil.....	31
3.3.2 Magnetic Field Generated by UltraFlex Coil.....	32
3.3.3 Heat Transfer Through Fuel Samples	33
 CHAPTER 4: RESULTS AND DISCUSSION	 36
4.1 COMSOL MODEL.....	36
4.1.1 Magnetic Field Strength Produced by MTI Induction Heater.....	36
4.1.2 Magnetic Field Strength Produced by the UltraFlex Induction Heater.....	37

4.1.3	Hysteresis Fuel Sample Heat Transfer Model.....	40
4.2	MNP RAW POWDER CHARACTERIZATION HEATING TESTS	42
4.3	FUEL AND PROPELLANT SAMPLE HEATING TESTS	44
4.3.1	MNP Fuel Hysteresis Heating Tests	44
4.3.2	Wired Fuel Eddy Current Heating Tests	51
4.3.3	MNP Propellant Hysteresis Heating Tests	51
4.3.4	Wired Propellant Eddy Current Heating Tests.....	53
4.4	MNP PROPELLANT BURNING RATE TESTING	54
CHAPTER 5: CONCLUSION AND FUTURE WORK.....		57
5.1	CONCLUSION	57
5.2	FUTURE WORK	58
REFERENCES.....		60
 APPENDICES		
APPENDIX A: MATERIAL CHARACTERIZATION.....		66
A.1	XRD ANALYSIS FOR MAGNETIC SUSCEPTORS	66
A.2	PARTICLE SIZE ANALYSIS	68
A.3	DC SQUID MAGNETOMETER DATA.....	74
APPENDIX B: AP ENCAPSULATION STUDY.....		78
APPENDIX C: STANDARD OPERATING PROCEDURES		81
C.1	MTI 25KW DESKTOP INDUCTION HEATER SOP	82
C.2	ULTRAFLEX SB3/1200 INDUCTION HEATER SOP	97
C.3	MIXING AND CASTING PROCEDURES	104
	C.3.1 Procedure for Mixing and Casting Fuel Samples	104
	C.3.2 Procedure for Mixing and Casting Propellant Samples.....	105
C.4	PROCEDURE FOR MANUFACTURING HTPB FILMS WITH AP ENCAPSULATIONS.....	108
APPENDIX D: SAMPLE FORMULATION MIX SHEET.....		110
APPENDIX E: FIBER OPTIC BREAK WIRE BURNING RATE MEASUREMENT		
TECHNIQUE		112

LIST OF FIGURES

Figure 2.1: Northrop Grumman's 1,800 gallon mixer. [27]	5
Figure 2.2: From Sutton and Biblarz, provided burning rates versus chamber pressure for several solid propellant formulations at multiple ambient grain temperatures [26]. The added red box highlights the results for APCP and aluminized-APCP as this is the formulation used in this study.....	6
Figure 2.3: From Kubota, temperature sensitivity characteristics of APCP [29].	7
Figure 2.4: From Kubota, effect of catalyst particle size on the burning rate and the pressure exponent of APCP [29].....	8
Figure 2.5: Representation of basic pintle nozzle design.....	9
Figure 2.6: From ArianeGroup, pressure control loop for a pintle system [1].	10
Figure 2.7: From Isert et al. "Propellant burning away from a copper wire at 13.8 MPa with 80 ms between exposures. The propellant burns radially after ignition." [4].....	11
Figure 2.8: Visual representation of the different regimes based on particle size. The first critical diameter shown is the divide between multi-domain and single domain particles. The second is the line between the ferromagnetic and superparamagnetic regimes [42].	15
Figure 2.9: Visual guide to the difference between Néel relaxation and Brownian relaxation. It is shown that Néel relaxation is the movement of the magnetic dipole inside a particle while Brownian relaxation is the movement of the particle itself [42].	16
Figure 3.1: TEM image of NanoAmor 30nm magnetite with post processing in ImageJ to estimate particle size diameter. The raw image is monochromatic, the yellow circles were added in processing.	20
Figure 3.2: Estimated particle size distribution of NanoAmor 30nm magnetite particles using TEM images and ImageJ.	21
Figure 3.3: HTPB fuel samples with embedded copper wire. Diameters from left to right (0.10, 0.25, 0.40, 0.51, 0.64)mm.	22
Figure 3.4: Magnetite (Fe ₃ O ₄) MNP propellant samples (Left) and aluminum wired propellant samples during casting (Right).	23
Figure 3.5: Block sample mold prepped for casting (left). Sample mold taken apart after sample removal (right). Samples are cut from the cured block.....	24
Figure 3.6: LabRAM intensity versus time and temperature versus time data from Claydon's thesis for mixing polymer bond explosives. These show the general trends for each phase of the mixing process, but the exact behavior will differ depending on the formulation being mixed [53].	25
Figure 3.7: Intensity versus time data from the LabRAM during the beginning of the mixing procedure (top) and the end of the mixing procedure (bottom). The three phases of the process are marked.	26
Figure 3.8: MTI SP25 Desktop induction heater.	27
Figure 3.9: Simple model of general heating test setup with the MTI SP25 Induction Heater.	27
Figure 3.10: Heating station with coil portion of the UltraFlex SB-3/1200 heater. This heater also comes with a power supply and water cooler.	28

Figure 3.11: Simple model of general heating test setup with the UltraFlex SB-3/1200 Induction Heater.	28
Figure 3.12: SolidWorks model of the test stand with a sample in place and the UltraFlex coil.	30
Figure 3.13: Cross sectional image of the test setup from the SolidWorks model.	30
Figure 3.14: MTI coil COMSOL model geometry.	31
Figure 3.15: COMSOL model of UltraFlex coil geometry and the surrounding box representing the air domain.	33
Figure 3.16: Hysteresis fuel sample COMSOL model geometry.	34
Figure 4.1: COMSOL simulation of magnetic flux density and magnetic field lines for MTI coil.....	36
Figure 4.2: Side and back views of magnetic field lines of UltraFlex coil on 6A setting with 789kHz frequency. Note: this is a wire frame diagram of the coil.	38
Figure 4.3: Side and back views of magnetic field lines of UltraFlex coil on 15A setting with 789kHz frequency. Note: this is a wire frame diagram of the coil.	38
Figure 4.4: Centerline of the UltraFlex coil used for gathering the data displayed in the following two figures.	39
Figure 4.5: Magnetic field strength along the centerline for the 6A setting of the UltraFlex coil for multiple frequencies.....	39
Figure 4.6: Magnetic field strength along the centerline for the 15A setting of the UltraFlex coil for multiple frequencies.....	40
Figure 4.7: Surface temperature model setup for simulated 2.5wt% heating in the UltraFlex Coil for 15s on the 15A setting. The dimensions of the sample, location of the coil, and boundary condition variable values are included.....	41
Figure 4.8: Surface temperature model at different time steps for the simulation of the 2.5wt% magnetite hysteresis fuel samples assuming the 15A, 15s UltraFlex heater settings.	41
Figure 4.9: Cobalt ferrite (left) and zinc ferrite (right) neat powder thermal characterization in MTI induction heater. Note: The jumping temperature behavior of cobalt and zinc ferrites is a product of initial camera placement and resolution.	43
Figure 4.10: Neat powder heating of magnetite in higher frequency UltraFlex heater at 6A (left) and the MTI heater at 200A and 800A (right). The UltraFlex test was halted at three seconds to avoid melting the sample holder.	43
Figure 4.11: Surface Temperature and Heating Rate vs Time for 15A/15s Hysteresis Fuel Samples	44
Figure 4.12: Magnetic hysteresis heating of HTPB fuel samples in UltraFlex Induction Heater.....	46
Figure 4.13: Magnetic hysteresis of 30nm magnetite in 50Oe field, taken with a DC SQUID magnetometer.....	47
Figure 4.14: Anisotropic constant values derived from literature for magnetite nanoparticles [43-44], [71-72].	49
Figure 4.15: Néel relaxation times for various particle sizes and temperatures using the anisotropic energy constant from Demotière.....	50

Figure 4.16: Néel relaxation times for various particle sizes and temperatures using the anisotropic energy constant from Mohapatra.	50
Figure 4.17: Thermal decomposition of HTPB fuel strand via heating from induction heated 0.64mm copper wire. Encircled in the center figure is the development of a gas interface along the solid wire due to decomposition. Encircled on the right is the escaping jet of HTPB decomposition products.	51
Figure 4.18: Combustion of 5wt% magnetite hysteresis based heated propellant. Note: The flame structure is of the burning PMMA barrier sheet that was around the propellant sample.	52
Figure 4.19: A) Surface of non-heated propellant sample. B) Surface of heated propellant sample. C) Heated propellant sample shows bulging in the center. D) Porosity inside heated propellant sample, shows that the AP and Al appear to be unaffected which supports the assumption that the urethane bonds in the binder are breaking down and isocyanate vapors are produced.	53
Figure 4.20: Ignition of 0.64mm aluminum wired propellant along the wire/propellant interface.	54
Figure 4.21: Results of dynamic burning rate testing of 2.5wt% magnetite propellant samples (average of three samples).	55
Figure A.1.1: XRD results for zinc ferrite from NanoAmor®.	66
Figure A.1.2: XRD results for cobalt ferrite from NanoAmor®	67
Figure A.1.3: XRD results for magnetite from NanoAmor®	67
Figure A.2.1: Particle size distribution results for magnetite on Malvern Zetasizer Nano ZS provided by MCL.	68
Figure A.2.2: Particle size distribution results for cobalt ferrite on Malvern Zetasizer Nano ZS provided by MCL.	69
Figure A.2.3: Particle size distribution results for zinc ferrite on Malvern Zetasizer Nano ZS provided by MCL.	69
Figure A.2.4: Particle size distribution results for magnetite on Mastersizer 3000 provided by MCL.	70
Figure A.2.5: Particle size distribution results for cobalt ferrite on Mastersizer 3000 provided by MCL.	70
Figure A.2.6: Particle size distribution results for zinc ferrite on Mastersizer 3000 provided by MCL.	71
Figure A.2.7: Transmission electron microscope (TEM) images used to estimate particle size distribution of NanoAmor® 30nm Fe ₃ O ₄ MNPs. The yellow circles were added during image processing with ImageJ to measure the diameter of 127 particles across the four images.	72
Figure A.2.8: Estimated particle size distribution of NanoAmor® 30nm Fe ₃ O ₄ MNPs based on TEM images and processing with ImageJ.	73
Figure A.3.1: DC SQUID Magnetometer data for 30nm magnetite in 70000Oe field.	74
Figure A.3.2: DC SQUID Magnetometer data for 30nm magnetite in a 500Oe field.	75
Figure A.3.3: DC SQUID Magnetometer data for 30nm magnetite in a 200Oe field.	75
Figure A.3.4: DC SQUID Magnetometer data for 30nm magnetite in a 100Oe field.	76
Figure A.3.5: DC SQUID Magnetometer data for 30nm magnetite in a 50Oe field.	76

Figure A.3.6: Combine figure of hysteresis curves produced by 50, 100, 200, and 500Oe fields for 30nm magnetite.....	77
Figure B.1: Thermal profile of AP encapsulated magnetite in HTPB films. Films contain 40% AP encapsulated magnetite.	79
Figure B.2: Results from STA performed by MCL on iron oxide and AP particles.	80
Figure B.3: More results from STA (TGA and DSC) analysis performed by MCL on iron oxide and AP particles.	80
Figure C.1.4: A. Location of induction heater outlet inside room 127, by the door between rooms 127 and 128. B. A close-up of the outlet, the correct plug is labeled "induction heater."	85
Figure C.1.5: Back panel of the MTI SP25 Desktop Induction Heater. [1].....	87
Figure C.1.6: Front panel of the MTI SP25 Desktop Induction Heater. [1]	88
Figure C.1.7: The red box is around the water valve for turning on and off the cooling water for the induction heater.....	89
Figure C.1.8: This flow meter will read 2, when the metal cylinder inside is aligned with the 2.....	89
Figure C.1.9: A. Foot pedal with safety block in place. B. Foot pedal with safety block removed.....	90
Figure C.1.10: Current adjustment knobs and current display screen.	90
Figure C.1.11: A. Shows the correct attachment for the foot pedal. B. Shows the switch for automatic vs manual operating mode.....	91
Figure C.1.12: Induction heater timer and operation indicator lights. [1]	91
Figure C.1.13: Time setting section of the heater. [1]	92
Figure C.1.14: TIMConnect Software. The red arrow is pointing to the record button.....	93
Figure C.1.15: TIMConnect Software. The red arrow is pointing to the stop recording button. This will automatically bring up a window to save the .ravi file.	94
Figure C.3.1: Pink ESD container with both lids. The normal lid has no holes the vacuum lid has two holes.	105
Figure C.3.2: Pink ESD container secured on the LabRAM with the lid in place. The vacuum port is in place, but this piece is not necessary unless mixing under vacuum.....	106
Figure C.3.3: ESD container secured on the LabRAM with vacuum port correctly attached. The lid to the LabRAM is not placed on top in this image.	107
Figure D.1: Portion of mix sheet for calculating and recording the mass of each ingredient. The numbers displayed are from batch number 42.....	110
Figure D.2: Portion of mix sheet used for calculating Cure Ratio, Mix Density, Solids Loading, O/F Ratio, and %TMD. This is from the mix sheet for batch 42.....	110
Figure D.3: Portion of the mix sheet used for recording the size and volume of the sample and mold. The values displayed are from batch 42.....	111
Figure D.4: This is the portion of the mix sheet that stores all necessary properties of the ingredients, and any notes about the mix. These are the values used for batch 42.	111

Figure E.1: Propellant strand burning rate configuration.....	112
Figure E.2: Response from break wires captured by LabVIEW. The lead break wires show high signal when broken and the fiber optic wires show a low signal when broken.....	113

LIST OF TABLES

Table 3.1: Magnetic Properties of Chosen Susceptors.....	19
Table 3.2: Propellant Formulation Metrics	22
Table 3.3: Material Properties for MTI Coil COMSOL Model.....	32
Table 3.4: Material Properties for Hysteresis Fuel Sample COMSOL Model.	34
Table 4.1: Magnetic Flux Density and Magnetic Field Strength Values of the MTI Coil for Various Excitation Currents	37
Table 4.2: Surface Temperature and Heating Power at 15sec (Experimental and COMSOL Results)	42
Table 4.3: Heating Data from Hysteresis Fuel Sample Testing.....	44
Table 4.4: Heating Power Comparison	47
Table 4.5: Temperature Sensitivity Values from Literature of AP Composite Propellants with Catalysts	56
Table B.1: Results of AP with Encapsulated Iron Oxide Heating Tests.....	78

LIST OF ABBREVIATIONS

Abbreviation	Meaning
AC	Alternating current
AFSOR	Air Force Office of Scientific Research
Al	Aluminum
AP	Ammonium perchlorate
APCP	Ammonium perchlorate composite propellant
ASRM	Advanced Solid Rocket Motor
DB	Double-base
DC	Direct current
DSC	Differential scanning calorimetry
ESD	Electrostatic discharge
ESSCI	Eastern States Section of the Combustion Institute
GO	Graphene oxide
Gui	Graphical user interface
HPCL	High Pressure Combustion Laboratory
HTPB	Hydroxyl-terminated polybutadiene
IH	Induction heating
IPDI	Isophorone diisocyanate
MCL	Materials Characterization Laboratory
MDI	Methylene diphenyl diisocyanate
MNP	Magnetic nanoparticles
MURI	Multidisciplinary University Research Initiative
PLA	Poly(lactic acid)
PMMA	Poly(methyl methacrylate)
PTFE	Polytetrafluoroethylene
RF	Radio wave frequency
SAR	Specific absorption rate
SOP	Standard operating procedure
SQUID	Superconducting quantum interference device
TDI	2,4-toluene diisocyanate
TGA	Thermogravimetric
TEM	Transmission electron microscope
WMIP	Weak microwave induced plasma

ACKNOWLEDGMENTS

First, I'd like to thank Dr. Richard Yetter and Dr. Eric Boyer for their support and advice during the pursuit of my master's degree. I have learned a lot from working at the HPCL, the hands-on experience I've gained is invaluable. I am beyond grateful to have had the opportunity to work in this lab.

I would also like to thank my lab mates, David Ramirez, David Drewniak, Dillon Over, and Nicolas Chai for their guidance and support. You guys made this journey enjoyable and kept me sane. A special thanks to David Ramirez for putting up with me on all our joint projects. I wouldn't have graduated without your help. You have taught me so much and I am very appreciative that I got to work with you.

I'd like to thank my family for all their love and support. To my Dad, I would not be where I am today without the passion for engineering you instilled in me as a kid. You've always pushed me to work hard, learn from my mistakes, and pursue my dreams. You are a role model to me, and I am beyond thankful you are my Dad. To my Mom, over the years you've shown me how to work hard while being kind, patient, and caring. These traits have been more than helpful throughout my life. I know you are always there for me. Thank you for being a great Mom. To my sisters, Brooke and Julia, I am so proud of you both and your accomplishments. Brooke, I strive to be as determined and motivated as you are every day. You've also taught me the importance of not forgetting to have fun along the way. Julia, you have shown me time and time again that people are stronger than they think they are (both mentally and physically). You inspire me to believe in myself and trust in my own abilities because you are the living proof of "I can do anything I set my mind to".

Finally, I would like to acknowledge the support from the Air Force Office of Scientific Research (AFOSR) Multidisciplinary University Research Initiative (MURI) grant number FA9550-19-1-0008. However, any findings and conclusions in this work do not necessarily reflect the views of the funding agency.

Chapter 1

INTRODUCTION

1.1 Motivation

Solid rocket motors exhibit predetermined thrust profiles governed by propellant composition, burning surface geometry, and motor conditions. There is a desire to have throttleable solid rocket motors for trajectory optimization, multi-purpose or multi-mission capabilities, and improved energy management by controlling thrust and pressure [1]. Current systems employed by the ArianeGroup use pintle valves to control thrust output mechanically [1]. However, these technologies have limitations related to system response time and errors in controlling the pintle location [1-2]. Research efforts have been made to actively change the burning characteristics of a propellant or fuel grain instead of mechanically modifying the thrust output. Wired propellants use embedded wires to locally enhance heat transfer through a propellant grain which results in increasing the burning surface area, therefore increasing the burning rate. These offer custom or improved performance, but the adaptability of the mission profile still needs to be improved [3-4]. Another avenue investigates the use of microwaves to heat propellant, leveraging the propellant's temperature sensitivity, to modify burning rate [5-9]. A limitation of microwaves is uneven heating caused by low penetration depth [5-9]. Other studies explore using an electric field to control the burning behavior of solid fuels and propellants [10-16]. Results found that an applied electric field can both increase and decrease the burning rate, but there remains debate on the mechanism behind the observed changes [10-16].

This study explores the application of induction heating (IH), a form of electromagnetic heating, to modulate the burning rate of solid fuels and propellants. Inspiration for this idea comes from the medical field's use of IH as part of a cancer treatment called magnetic hyperthermia [17-19]. The medical procedure aims to generate localized heating on a tumor to kill cancerous cells via necrosis, which is accomplished by injecting the tumor with magnetic nanoparticles (MNPs), then exposing the area to an oscillating magnetic field [17-19]. Thermal energy is generated by hysteresis heating of the MNPs. With this IH mechanism, heating occurs when magnetic dipoles within magnetic susceptors exhibit irreversible frictional losses during magnetic field alignment [20]. The efficiency of the hysteresis heating mechanism is impacted by additional behaviors observed in MNPs, Néel and Brownian relaxation. The medical field carefully selects MNP size and material to optimize heating within the biomedical restrictions on alternating magnetic field strength and frequency which prioritizes patient safety [17-19]. However, different susceptor selections can result in more significant heating that is applicable to modulating the burning rate of solid fuels and propellants. Another IH mechanism of interest is eddy current heating (Joule effect), which is a

form of resistive heating that occurs when an electrically conductive material is exposed to an oscillating magnetic field [20-23]. It requires a susceptor large enough to form conducting loops for current to flow through, such as a wire.

This thesis investigates the application of magnetic hysteresis and the Joule effect to dynamically modulate the burning rate of solid fuels and propellants. The main goal of this work is to understand each mechanism's heating potential and observe which variables most significantly control heating. A portion of this work was presented in March 2024 at the Eastern States Section of the Combustion Institute (ESSCI) Spring Meeting [24] and is discussed in a working paper by Ramirez et al [25].

1.2 Objectives

This study explores utilizing IH to dynamically modify the burning rate of solid fuels and propellants. The following objectives are discussed in this paper.

- Characterization of chosen susceptors.
- Development of a lab scale method for mixing and casting fuel/propellant samples with magnetic nanoparticles (MNPs) and embedded wires.
- Characterization of the heating power for samples with embedded MNPs.
- Establishment of the key parameters that control heating with each IH mechanism.
- Demonstration of dynamic changes in the burning rate of solid propellant samples with embedded MNPs using IH.

1.3 Thesis Organization

Chapter 2 is a literature review that will provide more information on the theory and concepts used in this study. First is a review of the current state of solid fuels and propellants. Then, there is a discussion of the current methods (employed systems and research initiatives) used to create throttleable or controllable solid fuels and propellants. Next, the heating mechanisms of and theory behind IH are explained. Finally, there is a discussion of the capabilities and limitations of COMSOL Multiphysics 6.0. This software was used to simulate the magnetic fields generated by the induction coils and model heat transfer through the fuel samples.

Chapter 3 discusses the experimental setups and methods employed by this study. All material characterization methods are described here. There is also a detailed discussion on developing the sample preparation process. A discussion of each type of test performed follows this. Finally, Chapter 3 discusses the development of each of the COMSOL models. Chapter 4 discusses the results from all testing and simulations, including heating tests, burning rate tests, models of the magnetic field generated by the

induction heater's coil, and heat transfer models of the fuel samples. Finally, Chapter 5 will discuss the conclusions and proposed future work. Additional information regarding material characterization, a brief study of iron oxide nanoparticles encapsulated by ammonium perchlorate (AP) crystals, procedures, data sheets, and a novel fiber optic burning rate measurement technique can be found in the appendices.

Chapter 2

LITERATURE REVIEW

2.1 Overview of Solid Propellants and Fuels

2.1.1 Solid Propellant Grain Classification and Manufacturing

Solid propellants are generally sorted into two categories: double-base (DB) and composite [26]. DB is the original type of solid propellant. DB is a homogenous grain made from a solid ingredient (typically nitrocellulose) that absorbs liquid nitroglycerine [26]. The development of composite propellants began with the exploration of using polymers as binders. Composite propellants are heterogeneous grains typically consisting of powdered fuel and oxidizer crystals held together by a plastic or synthetic rubber binder [26]. A standard formulation uses aluminum (Al) as the fuel, AP as the oxidizer, and hydroxyl-terminated polybutadiene (HTPB) as the binder [26]. The solid propellant samples investigated in this study are composites; therefore, the rest of this discussion will focus on that classification.

Manufacturing a composite grain begins with mixing all ingredients into a pourable, viscous slurry, similar to cake batter. The mixing process can be done in various ways depending on application and batch size. For example, small-scale solid propellant batches are typically mixed in a pint-sized stand mixer (similar to a Kitchen Aid mixer). Industry also uses larger mixers that are up to the size of a room. Figure 2.1 shows a picture of Northrop Grumman's 1,800-gallon propellant mixer [27]. On a fundamental research level, lab-scale batches can be mixed by hand. Mixing machines, such as LabRAM or FlackTek, are used for small-scale, lab-scale, and industry-sized batches, depending on the size of the machine. Once the mixture is homogenous, it is poured into a mold. The pouring process is called casting. It is vital to outgas the mixture during mixing or casting to avoid bubbles in the propellant [26], [28]. Bubbles create issues by adding unexpected burning surface area to the grain [26], [28]. Outgassing is best accomplished by mixing and casting in a vacuum environment.



Figure 2.1: Northrop Grumman's 1,800 gallon mixer. [27]

Finally, the mixture is baked until it has cured. Typically, the final grain feels like a hard rubber, similar to an eraser. The bake temperature and cure time depend on propellant composition, shape, and size. McCreary provides detailed information on the manufacturing of composite propellant grains [28]. This study used a lab-scale composite propellant manufacturing process following McCreary [28]. The specifics of this method and its development are discussed in section 3.1.4.

2.1.2 Solid Fuel Grain Applications and Manufacturing

Hybrid rocket motors and some high-speed air-breathing propulsion systems use solid fuel grains. These systems typically consist of a solid fuel and a liquid or gaseous oxidizer [26]. Some common fuels are HTPB (which is used as a binder in propellants) and paraffin wax [26]. Manufacturing a solid fuel grain is similar to a solid fuel grain. The fuel resin and any solid additive such as metal hydrides or Al are mixed and outgassed. Then cast into a mold and outgassed again. Finally, the grain is baked in an oven to cure.

2.1.3 Burning Rate Pressure and Temperature Sensitivity

Solid propellants have temperature and pressure sensitivities that affect the burning rate. Saint-Robert's (or Vieille's) Law governs pressure sensitivity (Equation 2.1) where r is the burning rate (mm/s or in/s), P is the chamber pressure (MPa or psi), n is the burning rate exponent (also called pressure exponent or combustion index), and a is the temperature coefficient [26], [29], which is an empirical value that is a function of ambient grain temperature.

$$r = aP^n \left[\frac{\text{mm}}{\text{s}} \right] \text{ or } \left[\frac{\text{in}}{\text{s}} \right] \quad \text{Equation 2.1}$$

The burning rate sensitivities of some standard solid propellant formulations have been characterized (Figure 2.2). In general, as chamber pressure increases, the burning rate will increase and if ambient grain temperature increases, the burning rate will increase (Figure 2.2).

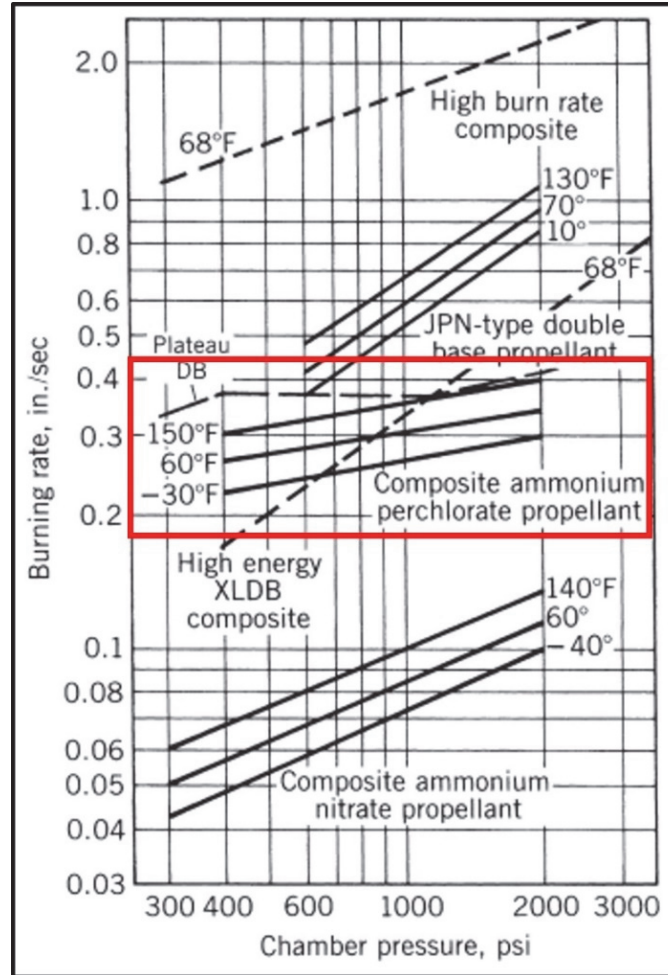


Figure 2.2: From Sutton and Biblarz, provided burning rates versus chamber pressure for several solid propellant formulations at multiple ambient grain temperatures [26]. The added red box highlights the results for APCP and aluminized-APCP as this is the formulation used in this study.

Burning rate can also be affected by temperature. Temperature sensitivity is expressed as two coefficients: the temperature sensitivity of the burning rate, σ_P ($1/^\circ\text{C}$) (Equation 2.2) and the temperature sensitivity of pressure, π_K ($1/^\circ\text{C}$) (Equation 2.3) [26], [29]. σ_P represents the change of burning rate per degree of ambient temperature change at a fixed chamber pressure, P , where r is the burning rate and T_b is the propellant ambient temperature [26]. π_K expresses the change in chamber pressure per degree change in ambient temperature for a fixed geometric factor K (ratio of burning surface area to nozzle throat area)

where p is chamber pressure and T_b is the ambient temperature of the propellant [26]. It can be gathered from Equations 2.2 and 2.3 that a propellant has the most significant temperature sensitivity with low burning rates and low pressures.

$$\sigma_P = \left(\frac{\partial \ln r}{\partial T_b} \right)_P = \frac{1}{r} \left(\frac{\partial r}{\partial T_b} \right)_P \left[\frac{1}{^\circ\text{C}} \right] \quad \text{Equation 2.2}$$

$$\pi_K = \left(\frac{\partial \ln p}{\partial T_b} \right)_K = \frac{1}{p} \left(\frac{\partial p}{\partial T_b} \right)_K \left[\frac{1}{^\circ\text{C}} \right] \quad \text{Equation 2.3}$$

For ammonium perchlorate composite propellants (APCP), like those explored by this study, temperature sensitivity is impacted by AP particle size and catalyst addition because the burning rate increases with a decrease in particle size or the addition of a catalyst. Kubota provides a visual representation of this dependency (Figure 2.3) where, for constant pressure and temperature, as the burning rate increases, the temperature sensitivity (σ_P) decreases [29]. This relationship is essential to recognize for this study because it aims to leverage the temperature sensitivity of an AP composite propellant to control the burning rate via IH. MNPs, such as ferric oxides (Fe_2O_3 and Fe_3O_4 , catalysts for APCP [29-31]), will be added to propellant and fuel samples to generate heat. The effect of catalysts on the thermal decomposition of AP and the burning rate of APCP has been previously characterized [30-33]. Kubota provides information on the ferric oxide catalyst, Fe_2O_3 (Figure 2.4). In this study, added MNPs will only be analyzed for their heating capabilities, not catalytic effect.

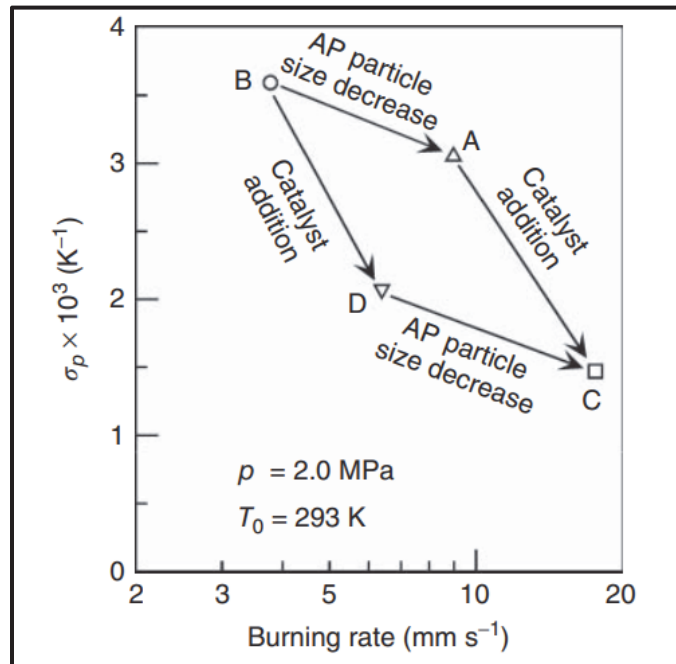


Figure 2.3: From Kubota, temperature sensitivity characteristics of APCP [29].

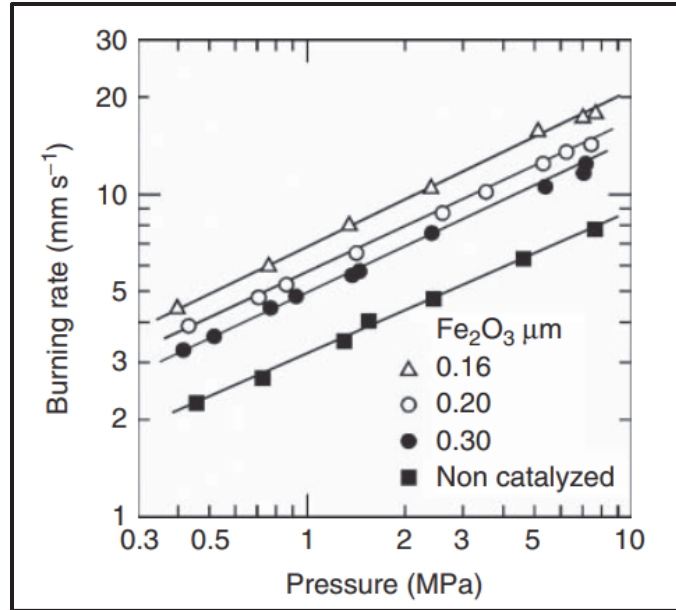


Figure 2.4: From Kubota, effect of catalyst particle size on the burning rate and the pressure exponent of APCP [29].

2.2 Current Attempts at Controlling or Throttling Solid Fuels and Propellants

2.2.1 Pintle Valves

In industry, mechanically operated thrust control systems such as pintle valves are utilized to throttle solid rocket motors [1]. Pintle systems control thrust output by changing the throat area with a moveable tapered plug (called a pintle) (Figure 2.5) [34-35]. The pintle can take different shapes and sizes depending on the nozzle design. Some have a pointed tip (Figure 2.5), while others have a rounded circular or parabolic head; the diameter is driven by throat and nozzle size. Pintles are typically made of carbon-carbon or carbon-silicon carbide due to these materials' high erosion and oxidation resistance [1]. Simulations model the effectiveness of the different pintle designs by looking at changes in output thrust, chamber pressure, pressure response time, pressure recovery coefficient, and mass flow rate [34]. These characteristics are important to understand because the stability of a rocket motor is highly dependent on chamber pressure, and the goal of the pintle system is to control output thrust.

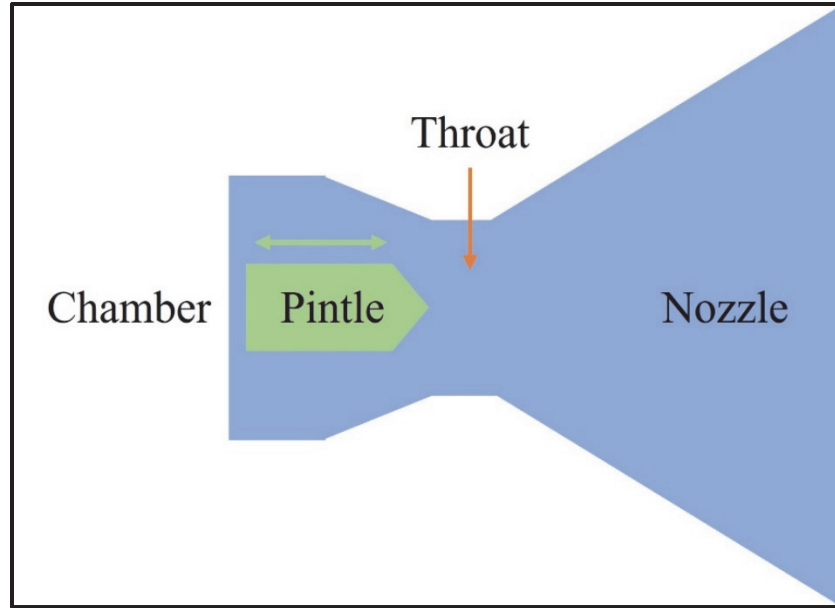


Figure 2.5: Representation of basic pintle nozzle design.

In currently employed systems, a pressure control loop manages pintle movement (Figure 2.6), which allows for corrections to pintle location to maintain thrust vector requirement as the throat area is modified by erosion [1]. This form of control is mandatory for propellants with a high pressure exponent because slight variations in the throat area lead to changes in chamber pressure [1]. The pressure loop control of a pintle system somewhat mitigates the pressure variations [1]. The control operates as shown in Figure 2.6 [1]. The system first takes in a desired thrust vector (F_c) and then computes the suitable chamber pressure (P_c) and throat area (S_{th}) [1]. Simultaneously, a mean pressure (P_m) is calculated from measured pressure values (P_r) inside the chamber [1]. The mean pressure is compared to the suitable chamber pressure to find the error (ϵ), which is converted to a throat area adjustment (ΔS) via a PID corrector [1]. Finally, the actuator orders (U_c) are derived from the corrected throat area (S_c), which was generated by the summation of the suitable throat area and the throat area adjustment [1]. The real throat area and thrust vector output are represented by S_r and F_r [1].

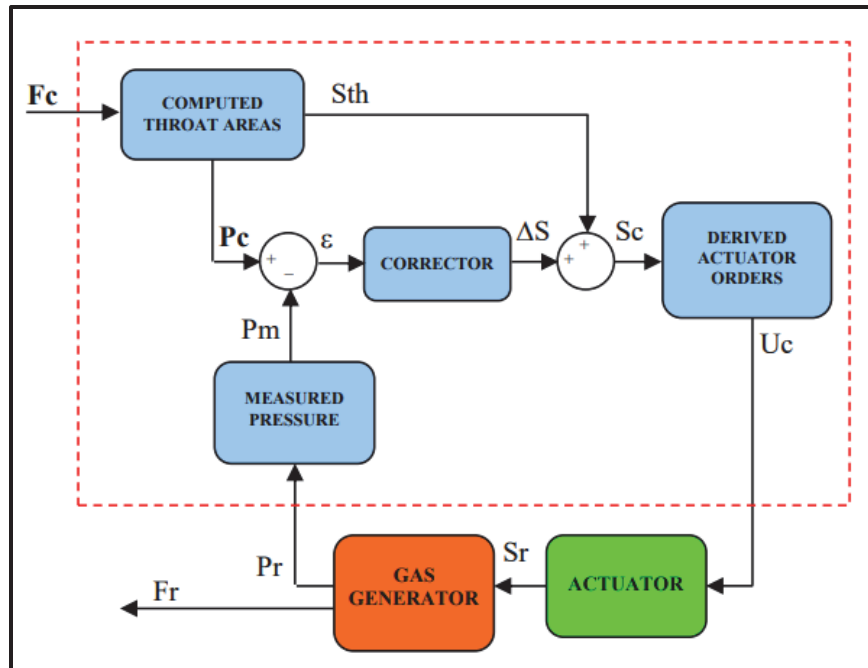


Figure 2.6: From ArianeGroup, pressure control loop for a pintle system [1].

While this system does provide thrust control, it is limited by response time and uncertainties in pintle location. This constraint has led to further research into the control of pintle valves [34]. Another limitation of pintle valves is that they are only compatible with some propellant formulations. Condensed phase species in exhaust gases can erode the pintle or clog the nozzle [1]. As a result, metal-free propellants, which may have lower performance due to the removal of metal fuels, must be used [1]. This study's proposed method of control via induction heating would allow for the use of metal propellants and is not reliant on the control of an actuator.

2.2.2 Wired Fuels and Propellants

Wired propellants/fuels are one method for enhancing burning rate. The use of embedded wires stems from an observation made in 1944 that the burning rate of a propellant sample increased in the area surrounding small metal thermocouples [36]. It was concluded that the increase in the burning rate was caused by coning along the thermocouple wire due to the metal's higher thermal conductivity than the grain [36]. This observation led to the investigation of embedding small wires inside solid propellant to increase heat transfer through the grain, therefore enhancing the burning rate [36-37]. Substantial increases of 2.5 to 3.0 times the baseline burning rate were observed [36]. Ideal wires like copper or silver have a high thermal diffusivity and melting point [4], [37]. When using long wires, the diameter must also be considered—generally, the larger the diameter, the faster the burning rate [4], [37-38]. However, there is an upper limit on wire diameter at which it acts as a heat sink and decreases the burning rate [4], [37-39]. Wires locally preheat sections of the grain as the flame approaches, which can modify the burning surface area, for

example, turning a flat-end burn into a conical burn [4], [37]. Isert et al. captured the effect of embedded long copper wire in non-aluminized AP/HTPB composite propellant on the burning surface area (Figure 2.7) [4]. As the flame proceeded down the grain, the burning surface area expanded radially due to coning from heat transferred from the flame through the wire faster than the propellant.

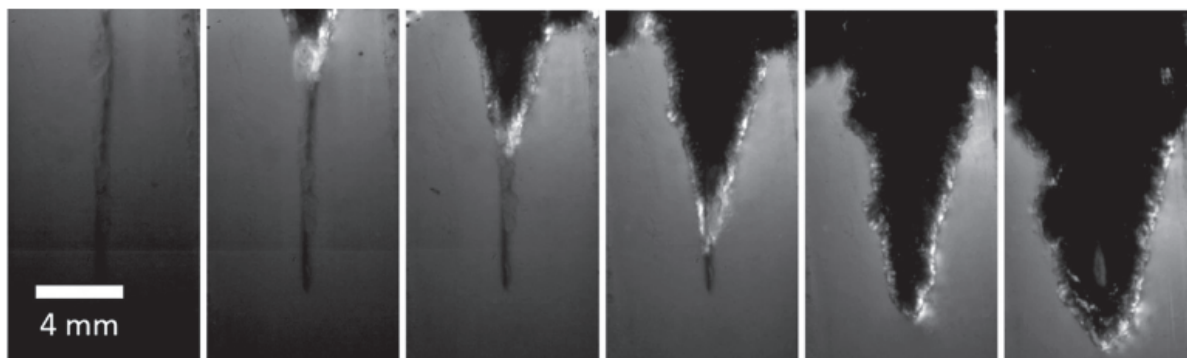


Figure 2.7: From Isert et al. “Propellant burning away from a copper wire at 13.8 MPa with 80 ms between exposures. The propellant burns radially after ignition.” [4]

While the addition of inert wires has proven to significantly increase burning rate, there are some drawbacks. Most notably, as wires are added, the ratio of inert material to energetic material in the propellant increases. At a certain point, the overall performance of the propellant will be decreased [4], [38-39]. As a result, more recent work has explored embedding reactive wires [4]. Isert et al. compared the effect of embedding Al/polytetrafluoroethylene (Al/PTFE) reactive foils, nickel/Al nanofoils, and self-alloying wire (Pyrofuze®) to standard copper wires [4]. One result of interest from this study is the mechanism causing a significant burning rate enhancement from the reactive Al/PTFE foils [4]. Unlike the other investigated materials, the Al/PTFE foils do not increase burning surface area [4]. Instead, they are consumed, releasing gases that react with and increase the temperature of the propellant’s combustion products, enhancing the burning rate [4]. Results showed that the Al/PTFE foils increased the burning rate more significantly than standard copper-wired propellants [4]. However, this method enhances localized propellant burning rate rather than bulk burning rate [4].

2.2.3 *Applied Electric Field*

Since the 1960s, researchers have explored the effects of applying a DC electric field to burning various fuels and propellants [10-16]. In all work there have been observations of an influence on the burning rate as well as flame structure, but it is unclear what mechanism is the cause. The debate remains between a few options: Joule effect heating, ionic winds, and alterations in chemical kinetics [10-16].

Baranov et al. [12] investigated the effect of an electric field on solid composite propellant samples in a flat form factor. Baranov et al. observed fluctuations in burning rate as electric field intensity was

increased. There is an initial decrease to about 65-75% of the initial value, and then an increase to greater than the initial burning rate value. Baranov et al. [12] argues against the mechanism of Joule effect heating, claiming that in their experiments, the power used could not substantially influence the flame temperature. They also argued against ionic winds, claiming that their burning rate measurements were insensitive to the polarity of the applied field. Instead, Baranov et al. [12] proposes that additional oxidizer is carried into the reaction zone because the applied field creates surface roughness which allows for early escape of the oxidizer (in their experiment this was AP).

Abrukov et al. [11] explored mixtures of AP, polymerized polybutadiene, and Al with an externally maintained discharge. Different effects were observed depending on the polarity of the field applied. In general, increases in linear burning rate were found for both cases. However, poorly dispersed mixes in a field with a positive specimen showed a reduction in linear burning rate. Abrukov et al. [11] also observed changes in the flame shape depending on field polarity. When the negative electrode was on top with the positive at the specimen, the positive ions flow upwards, and the negative ions flow downward. The opposite is true when the electrodes are switched. Under both conditions, ionic winds were generated, and were the main source of the effects caused by the applied electric field. It is proposed that the ionic winds recirculated the reaction products back to the specimen increasing heat transfer to the surface [11].

Bestgen [13-14] investigated the effects of an electric field applied to two different AP, metalized solid propellants (one with a DB binder and the other with polybutadiene). Bestgen [13-14] also explored multiple experimental setups to understand the impact of how and where the electric field is applied. For the case of an incomplete circuit, the applied voltage had no effects on burning rate or flame. When the propellant was placed as media between the electrodes, arcing occurred, but there were no changes in burning rate or flame. In the setup where the propellant acted as one of the electrodes, both burning rate increases and decreases of about 20-25% were observed [13-14]. The propellant with a DB binder had burning rate decreases which are thought to be caused by flame electrons creating reactional interference via electron encounters. The burning rate increases observed in the polybutadiene samples are thought to be a result of current effects inside the solid propellant. It is proposed that preferential current paths through the propellant change the burning surface area and therefore the burning rate. Bestgen [13-14] also concludes that ionic winds do not play a role in burning rate changes.

Young et al. [10] explored the effects of an applied electric field on solid fuels and propellants. The solid fuels were tested in an opposed flow burner setup while the propellants were tested in an optically accessible strand burner. For the fuel samples, it was observed that regardless of polarity, the distance that the paraffin fuel sample burned was a function of applied electric field strength; as the field strength was increased, the burning distance decreased. It was also observed that at specific voltage levels, arcing

occurred. This behavior is dependent on polarity, when the upper electrode is positive arcing began at a voltage nearly half that of the reverse case. For the propellant samples, both aluminized and non-aluminized formulations were investigated. Burning rate decreases that were linearly related to electric field strength were observed in both cases. This behavior also appears to be pressure dependent as the effect is greater at higher pressures. It is proposed that the decrease in burning rate of the aluminized propellants rules out Joule effect heating as the driving mechanism for burning rate alteration [10]. Rather, it is concluded that ionic winds may be causing changes in chemical kinetics and reacting species concentrations [10].

To summarize, the consensus of the researchers is that an applied DC electric field influences burning characteristics of fuels and propellants, but there is disagreement on the driving mechanism. There is great dependence on experimental setup, field polarity, sample formulation and geometry. This research initiative is promising but requires more work to be fully understood. The application of an electric field to premixed and diffusion flames has also been studied but is not covered in this literature review as it is less applicable to this work compared to the study of solid fuels and propellants. More information regarding the effect on flames can be found in references [40-41].

2.2.4 Microwave Enhancement

Microwaves are a form of electromagnetic radiation in the frequency range of 300MHz to 300GHz. Multiple studies by Sipple and collaborators explored using microwaves to transfer energy to flame structures and enable dynamic control of composite propellant energy release [5-9]. Two avenues for microwave energy transfer were investigated: the gas phase flame and the condensed phase propellant. To interface with the gas phase flame, two methods were proposed. The first is to establish a weak microwave induced plasma (WMIP) inside the flame by increasing the electron number density of the flame. Second, couple with the high-temperature metal oxide combustion products such as aluminum oxide, because their dielectric loss increases with temperature. Of the two methods, WMIP proved to be effective when doped with alkali metals, which are energetic materials with reagents that produce electro-positive species. It was observed that doped propellants had flame emission intensities increase between 4-13 times non-doped propellant and a burning rate increase of 20-60% based on weight percentage of dopant and the presence of aluminum [5-6], [7], [9]. Aluminized propellants had higher burning rate increase compared to non-aluminized [5-6], [7], [9]. It was proposed that microwaves couple with the condensed phase aluminum oxide combustions products, resulting in enhanced burning rate due to the presence of aluminum in the propellant. This theory was validated by the observation of a 10% burning rate enhancement when microwaves were applied to aluminized non-doped propellant [5-6], [7], [9]. It was concluded that all observed burning rate increases are mainly a result of thermal feedback to the propellant burning surface from the multiple energy deposition mechanisms.

Two methods were investigated for interfacing with condensed phase propellant: graphene oxide (GO) wrapped thermites and wired propellants [6], [8]. Nanoscale GO thermites were developed to be thermally switchable in terms of microwave absorptivity for controlled ignition delay. It was found that GO is highly microwave reflective and thermites wrapped in GO are not microwave-ignitable when exposed to high-powered microwave irradiation for up to 60 seconds [6], [8]. However, it was also observed that heating the wrapped thermites, reduced the GO layer and enabled microwave-ignition in as short as 200 to 300ms [6], [8]. Materials such as these thermally switchable thermites could also be used to create highly localized microwave loss to the burning surface. It was proposed that more work be done to develop other “smart” energetic materials [6], [8].

As stated above, microwaves were also applied to wired propellants to dynamically control solid propellant energy release via the condensed phase grain. As previously discussed in Section 2.2.2, adding inert wires to solid propellant enhances burning rate by locally preheating sections of the grain due to transferring heat from the flame through the wire faster than the grain. Applying microwaves to wired propellants allows for more significant burning rate enhancement because the wires are heated by the microwaves through Joule effect heating [6], [8]. The alternating field induces eddy currents inside the wire that results in heat generation from the current flowing through the resistance of the wire [6], [8]. Energy dissipation via the Joule effect (eddy current heating) is related to the penetration depth of the field which scales with frequency and material properties [6], [8].

As frequency of the field increases, penetration depth decreases and when the penetration depth is less than the diameter of the embedded wire there is a drop in power dissipation [6], [8]. As a result, the highest burning rate enhancement was observed with wires whose diameter was small enough to allow for penetration to the center and therefore no skin effects (when the induced current flows through just the outer layer of the susceptor) [6], [8]. With 0.3mm diameter graphite wire a burning rate enhancement of 700% was observed, while 1mm diameter graphite wire only provided a 62.5% enhancement [6], [8].

2.3 Induction Heating Theory

This study proposes induction heating (IH) to dynamically control solid propellant burning rates. Induction heaters utilize magnetic fields generated by a coil driven by an RF alternating current (3kHz to 300MHz) [20], [22-23]. IH has two relevant heating mechanisms to solid propellant: magnetic hysteresis heating and the Joule effect (eddy current heating). Magnetic hysteresis generates heat when magnetic dipoles within magnetic susceptors exhibit irreversible frictional losses during magnetic field alignment. In other words, heat is released due to friction caused by magnetic domain wall movement inside the particle as it attempts to align itself with the field. Utilizing magnetic particles enables uniform heating at low

concentrations if well dispersed. The magnetic hysteresis heating potential of a susceptor depends on composition and particle size. Metal spinel ferrites are a class of magnetic susceptors of the composition MFe_2O_4 , where $M = Zn, Co, Fe, Ni$, etc [42]. The coercivity (measure of a susceptor's ability to withstand a magnetic field without demagnetizing) and saturation magnetization (maximum magnetization of a susceptor) drastically differ depending on the metal cation; thus, the hysteresis loop. Ferrites are particularly interesting since they can act as both magnetic susceptors and burning rate catalysts [31-33].

For magnetic hysteresis, the volumetric heating potential of a susceptor in an AC field depends on the area of the hysteresis loop and the frequency at which the loop is cycled [21]. Equation 2.4 governs the volumetric heating power for a given hysteresis loop where μ_0 is the permeability of free space ($4\pi * 10^{-7}$) in H/m, f is frequency in Hz, and $\oint HdM$ represents the area inside the hysteresis loop in A^2/m^2 .

$$P = \mu_0 f \oint HdM \text{ [W/m}^3\text{]} \quad \text{Equation 2.4}$$

The saturation magnetization is relatively constant across particle size for a given temperature. Still, its coercivity is particle size dependent and peaks when the magnetic grain structure transitions from a multi-domain (more than one magnetic domain inside the particle) to a single domain (one magnetic domain inside the particle) [21]. Further reduction in particle size results in a transition into the superparamagnetic regime at which there is a reduction of magnetic properties and heat generation (Figure 2.8) [42].

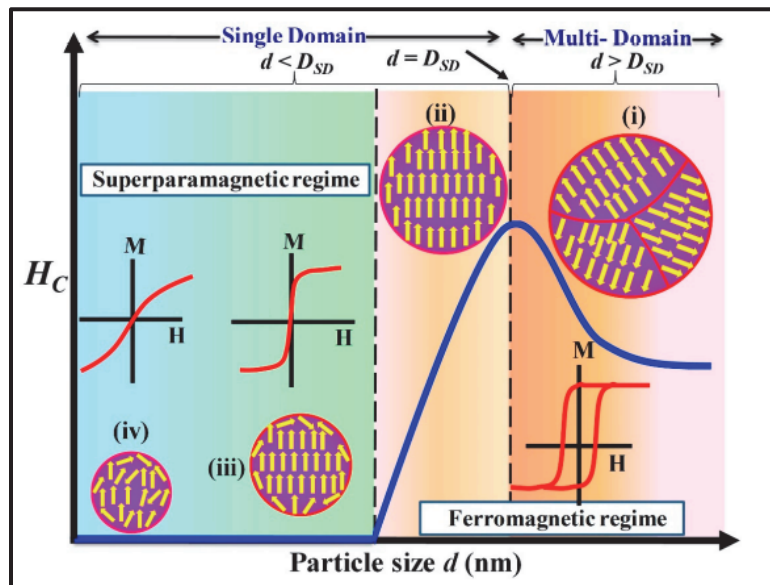


Figure 2.8: Visual representation of the different regimes based on particle size. The first critical diameter shown is the divide between multi-domain and single domain particles. The second is the line between the ferromagnetic and superparamagnetic regimes [42]

Rocket propellant combustion must be controlled; therefore, in burning rate modulation systems, the system must not contribute to a catastrophic failure. Magnetic materials exhibit temperature dependent

behaviors that can prevent thermal runaway. These characteristics include the susceptor's Curie temperature, superparamagnetic limit, and Néel relaxation time. Each susceptor exhibits a Curie temperature, at which it will lose its permanent magnetic properties, and heating via hysteresis will stop [21]. The superparamagnetic limit is dependent on both temperature and particle size [42-45]. For a given temperature, as particle size decreases, the susceptor enters the superparamagnetic region, where the magnetic dipoles within the susceptor can alternatively align themselves with the magnetic field via Néel and Brownian relaxation (Figure 2.9) [42]. As temperature increases, the size at which individual particles enter this regime also increases [42-45].

Brownian relaxation refers to the motion of an entire particle rotating as the magnetic field oscillates [42-45]. This mechanism reduces magnetic hysteresis heating efficiency because there is no longer heat generation from magnetic domain wall movement inside the particle. In composite propellant, the solid state of the propellant grain prevents the magnetic susceptor's physical rotation and therefore Brownian relaxation.

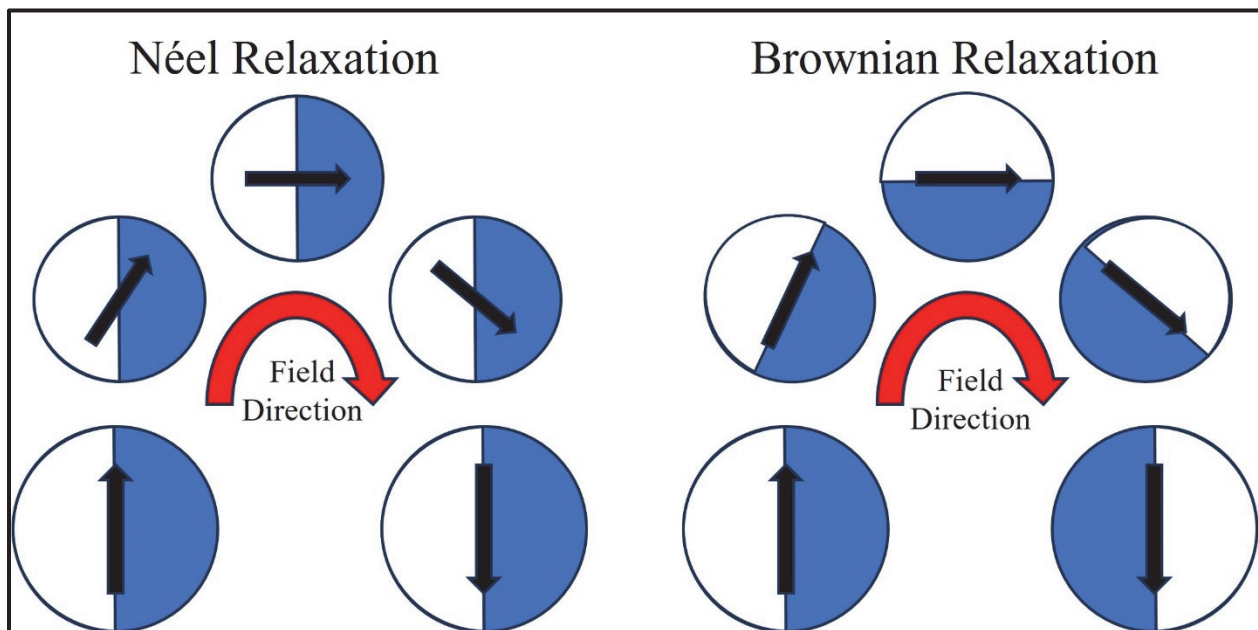


Figure 2.9: Visual guide to the difference between Néel relaxation and Brownian relaxation. It is shown that Néel relaxation is the movement of the magnetic dipole inside a particle while Brownian relaxation is the movement of the particle itself [42].

Néel relaxation occurs when magnetic susceptors contain adequate thermal energy, enabling the spontaneous flipping of their magnetic dipole [42-45]. Thus, particle size selection can enable Néel relaxation, reducing the hysteresis heating potential at a predetermined temperature [42-45]. Néel relaxation can also affect the heating efficiency of particles inside the ferromagnetic regime. Néel relaxation time is the average time between spontaneous rotations of a susceptor's magnetic dipole. It depends on particle

size, anisotropic energy, and temperature as shown by Equation 2.5, where τ_0 is the attempt frequency, K_{eff} is the effective anisotropic energy density, V is hydraulic volume, k_B is the Boltzmann constant, and T is temperature [42-44]. Néel relaxation time will decrease as particle size decreases or temperature increases.

$$\tau_N = \tau_0 \frac{K_{\text{eff}} V}{k_B T} \quad \text{Equation 2.5}$$

If the susceptor is not in the superparamagnetic regime but has a Néel relaxation time less than the frequency of the induction heater, the particle's heating efficiency significantly drops because the particle freely rotates faster than the magnetic field is flipping [42-44]. Therefore, characterizing the Néel relaxation time of a susceptor will be necessary for selecting induction heater parameters because it can significantly impact heating efficiency. Customized hysteresis heating rates can be achieved by carefully selecting induction heater system parameters and susceptor properties.

IH can also enable a Joule effect (eddy current heating) in a conductive continuum in propellants. Eddy current heating occurs when any electrically conductive material is exposed to an oscillating magnetic field [20-23]. The magnetic field induces eddy currents inside the material and produces thermal energy via resistive heating. Specific heating power is governed by Equation 2.6 [45] where P is specific power (W/kg), B_p is peak magnetic field strength (T), f is frequency (Hz), d is wire diameter (m), ρ is material resistivity ($\Omega \cdot \text{m}$), D is density (kg/m^3). Equation 2.6 assumes that the material and magnetic field are uniform and demonstrate no skin effect.

$$P = \frac{\pi^2 B_p^2 d^2 f^2}{12 \rho D} [\text{W/kg}] \quad \text{Equation 2.6}$$

Eddy current heating requires a large enough piece of material to form a current loop. In general, the larger the material, the greater the heating power. However, the skin effect must be considered as the size is increased.

The penetration depth of a magnetic field in a conductor is given by Equation 2.7 [45] where ρ is electrical resistivity of the material ($\Omega \cdot \text{m}$), f is frequency (Hz), and μ_r is relative magnetic permeability. Lower frequency magnetic field oscillations result in greater penetration depth. The radio wave frequency range (3kHz to 300MHz) used by IH reduces the microwave frequency (300MHz-300GHz) related issue of low penetration depth, which should result in more uniform heating throughout the propellant grain.

$$\delta = 503 \sqrt{\frac{\rho}{\mu_r f}} \quad [\text{m}] \quad \text{Equation 2.7}$$

In this work, both magnetic hysteresis and the Joule effect (eddy current heating) are investigated as potential candidates for controlling the burning rate of a solid fuel/propellant. Magnetic hysteresis heating is advantageous from a uniform heating perspective since the magnetic susceptors can be dispersed throughout the material. Eddy current heating can generate more thermal energy than magnetic hysteresis heating, but it requires larger conductors that cannot be as well dispersed as MNPs therefore the effect will be more localized.

2.4 COMSOL Modeling

COMSOL Multiphysics 6.0 was used for modeling throughout this study. COMSOL Multiphysics is a software designed for engineers and scientists to simulate many different devices, designs, and processes [46]. It is capable of single-physics and fully coupled multi-physics models [46]. It includes physics interfaces that model electromagnetic fields, heat transfer, fluid dynamics, and more. One example of multi-physics coupling includes pairing heat transfer physics and electromagnetic fields to model IH. While this software has excellent capabilities, it also has some limitations. It can be challenging to learn to use because it has a large number of settings and options. To help with this issue, COMSOL provides example models and video tutorials. The models discussed in this study were developed with the guidance of the Modeling Electromagnetic Coils in COMSOL course by Walter Frei [47]. A discussion of other limitations specific to this study is in Section 3.3.

Chapter 3

METHODS

3.1 Sample Preparation

3.1.1 Characterization of Magnetic Nanoparticles (MNP)

This study explored four MNP susceptors due to their contrasting magnetic properties: zinc ferrite (ZnFe_2O_4), cobalt ferrite (CoFe_2O_4), magnetite (Fe_3O_4), and maghemite ($\gamma - \text{Fe}_2\text{O}_3$). All materials except for $\gamma - \text{Fe}_2\text{O}_3$ are from NanoAmor® and provided by Dr. Qing Wang's lab at Penn State. The maghemite was from US Nano®. The suppliers provided magnetic properties [48-50] for all susceptors except for Fe_3O_4 , whose values are gathered from literature (Table 3.1) [43]. To validate the material's composition, XRD analysis was performed at the Penn State Materials Characterization Lab (MCL) on all except for $\gamma - \text{Fe}_2\text{O}_3$. The XRD results confirmed the composition of all susceptors tested, the data from that analysis are included in Appendix A.1.

Table 3.1: Magnetic Properties of Chosen Susceptors

Magnetic Susceptor	Curie Temp. [°C]	Single Domain Limit	Superparamagnetic Limit	Saturation Magnetization [emu/g]	Remanent Magnetization ¹ [emu/g]	Coercivity [Oe]
99% 30 nm Fe_3O_4	577	$d_{\text{SD}} < 128\text{nm}$	$d_{\text{SP}} < 20\text{nm}$	85	20	300
98% 35-55nm CoFe_2O_4	529	$d_{\text{SD}} < 40\text{nm}$	$d_{\text{SP}} < 10\text{nm}$	46.8	17.3	900
98% 35-55nm ZnFe_2O_4	93	n/d	$d_{\text{SP}} < 17\text{nm}$	4.0	0.06	84
99.5% 20 nm $\gamma - \text{Fe}_2\text{O}_3$	645	$d_{\text{SD}} < 166\text{nm}$	$d_{\text{SP}} < 20\text{nm}$	56.89	15	0.48

Multiple methods were used at MCL to characterize the particle size distribution of the magnetic susceptors, but this proved difficult. The first attempt was made on a Malvern Zetasizer Nano ZS which uses dynamic light scattering. The susceptors were suspended in water and dispersed via shaking by hand. The results showed an average particle size of about 1000nm. This result seemed unrealistic, as it was much larger than the expected 20-50nm. A second attempt was made with a Mastersizer 3000, which uses laser diffraction. This time, ethanol was used as a dispersant, and the sample was prepared with 20-30 seconds

¹ Magnetization left in the susceptor when a magnetic field is no longer applied.

of sonication. However, the results were similar to the first method; the particle size was around $1\mu\text{m}$. It was concluded that agglomerations and poor dispersion are most likely the cause of the large particle size. The data from both particle size analysis methods are provided and further discussed in Appendix A.2. After IH testing with propellant and fuel samples containing magnetite particles (discussed in Chapters 3 and 4), there was further need for a rough particle size distribution of the magnetite MNPs. Transmission electron microscopic (TEM) imaging was used to perform this characterization. Images of the magnetite powder suspended in epoxy were obtained with a Titan³ G2 microscope at MCL. ImageJ [51] processing software was used to estimate the diameters of the particles. Across four TEM images, 127 particles were measured (Figure 3.1). The average particle size is $15.60\pm 5.07\text{nm}$, with the distribution portrayed in Figure 3.2. It should be noted that this result may be biased toward smaller particles due to the difficulty of differentiating large particles from agglomerates. The main conclusion from this analysis is that a significant portion of the magnetite particles may be impacted by Néel relaxation time or the superparamagnetic limit. Further discussion on this implication in relation to heating power is provided in Section 4.2. Additional images used to generate the particle size distribution can be found in Appendix A.2.

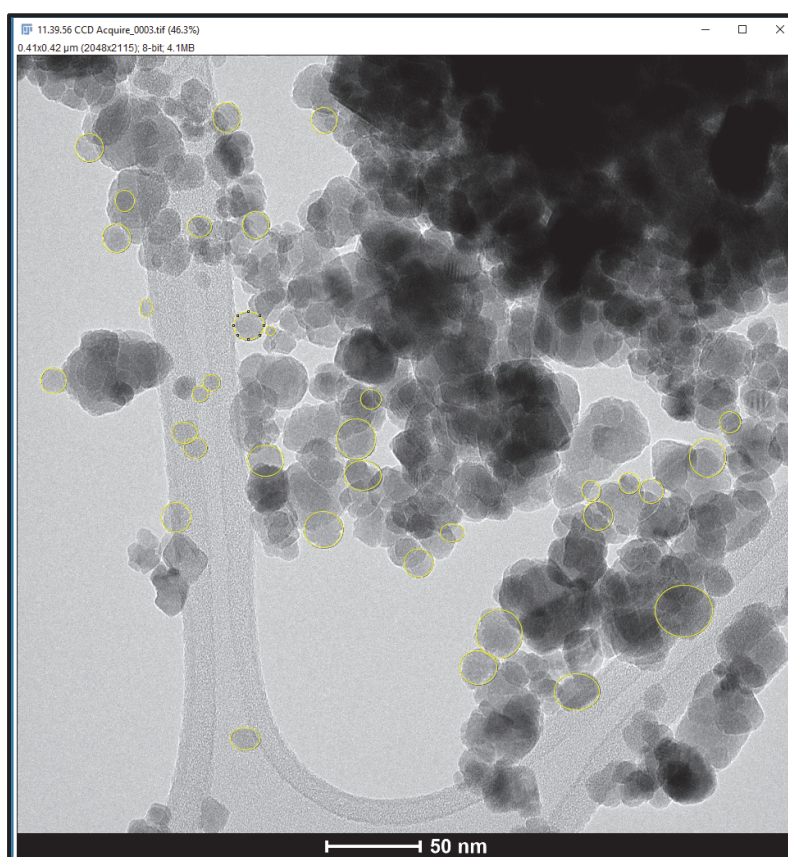


Figure 3.1: TEM image of NanoAmor 30nm magnetite with post processing in ImageJ to estimate particle size diameter. The raw image is monochromatic, the yellow circles were added in processing.

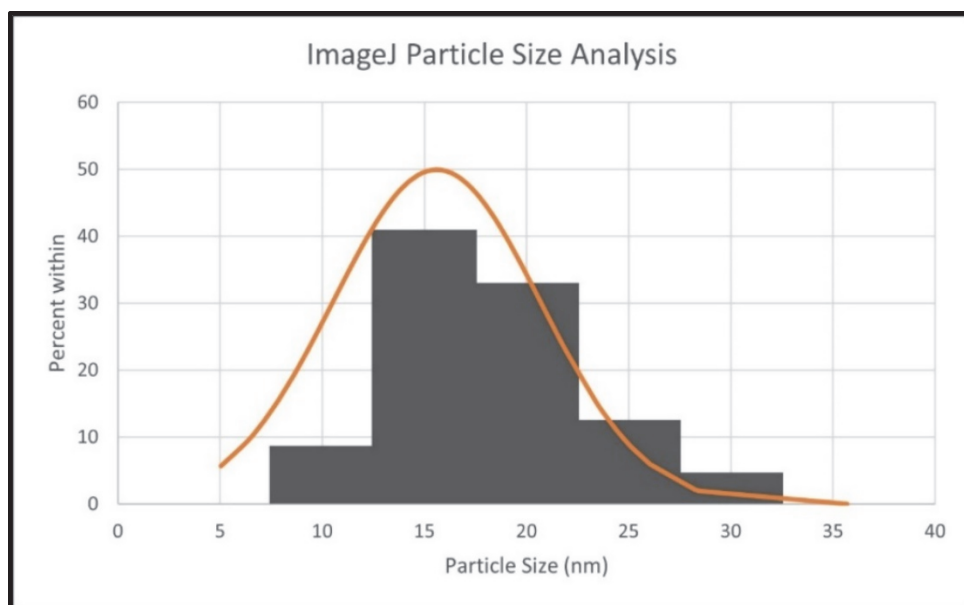


Figure 3.2: Estimated particle size distribution of NanoAmor 30nm magnetite particles using TEM images and ImageJ.

3.1.2 Fuel Sample Formulations

Hysteresis fuel samples are comprised of the following ingredients:

- Firefox Enterprises Inc. Hydroxyl Terminated R-45M Poly-Butadiene Resin
- Thermo Scientific Isophorone Diisocyanate 98%+ (Cat: 428602500)
- Sigma-Aldrich® Bis(2-ethylhexyl) adipate (DEHA) 97%+
- TCL America Dibutyltin Dilaurate >95% (Stock# D0303)
- TCL America Dibutyl Phthalate >97.0% (Stock# P0292)
- NanoAmor® 30nm Fe_3O_4 99% (Stock#2654WJ) (magnetite)

Varying weight percents (1wt%, 2.5wt%, 5wt%) of the magnetite particles were investigated.

Joule effect fuel samples are comprised of the same formulation as the hysteresis samples, excluding the magnetite particles. These samples utilized embedded copper and aluminum wires. Copper wires with diameters ranging from 0.10-0.64mm (Figure 3.3) and aluminum wires of 0.32 and 0.64mm with diameters were investigated. The weight percentages of all ingredients for each mix batch were recorded. An example mix sheet is in Appendix D.1.

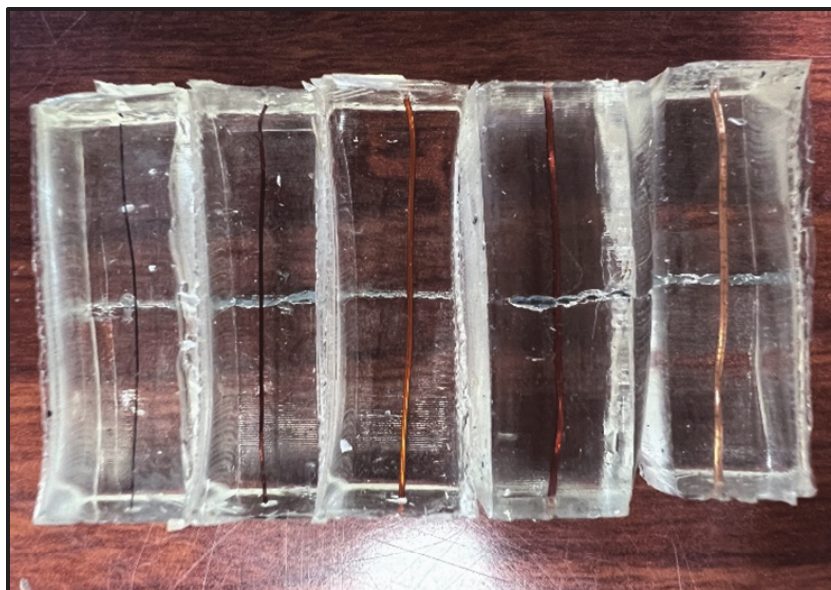


Figure 3.3: HTPB fuel samples with embedded copper wire. Diameters from left to right (0.10, 0.25, 0.40, 0.51, 0.64)mm.

3.1.3 Propellant Sample Formulations

Hysteresis propellant samples composition comprised of the following ingredients:

- Valimet H-95 spherical aluminum powder
- PyroChem Source 90- μm Ammonium Perchlorate
- PyroChem Source 200- μm Ammonium Perchlorate
- Firefox Enterprises Inc. Hydroxyl Terminated R-45M Poly-Butadiene Resin
- Thermo Scientific Isophorone Diisocyanate 98%+ (Cat: 428602500)
- Sigma-Aldrich® Bis(2-ethylhexyl) adipate (DEHA) 97%+
- TCL America Dibutyltin Dilaurate >95% (Stock# D0303)
- TCL America Dibutyl Phthalate >97.0% (Stock# P0292)
- NanoAmor® 30nm Fe_3O_4 99% (Stock#2654WJ) (magnetite)

Varying weight percents (2.5wt%, 5wt%) of magnetite particles were used. The formulation metrics are shown in Table 3.2.

Table 3.2: Propellant Formulation Metrics

Cure Ratio	1.0
Oxidizer/Fuel (O/F) Ratio	2.17-2.20
Coarse to Fine AP Ratio	1.95
Solids Loading	80%

Joule effect propellant samples were comprised of the same formulations as the hysteresis samples (excluding the magnetite particles) but contained aluminum or copper wires (Figure 3.4). These samples also have similar metrics to those displayed in Table 3.2. The weight percentages of all ingredients for each mix batch were recorded in the mix sheet (Appendix D.1).

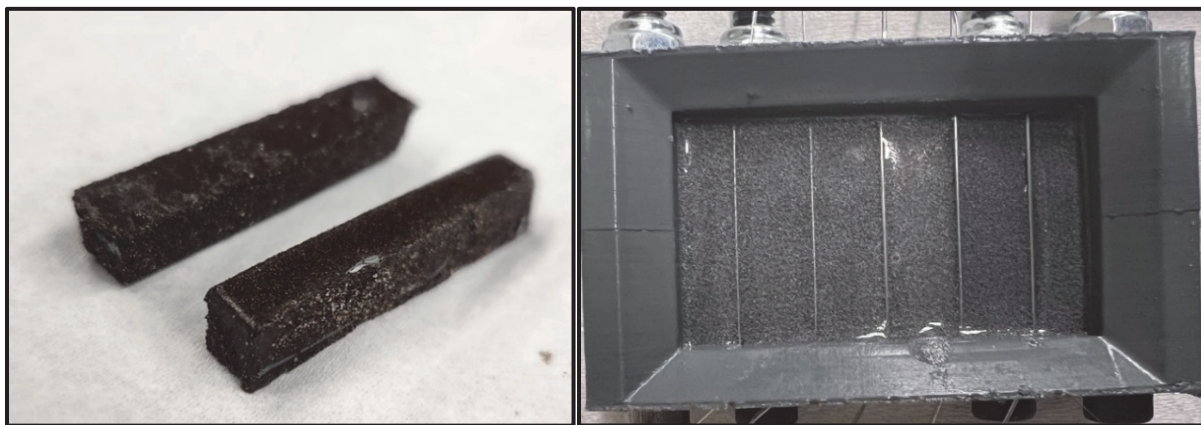


Figure 3.4: Magnetite (Fe_3O_4) MNP propellant samples (Left) and aluminum wired propellant samples during casting (Right).

3.1.4 *Mixing and Casting Process*

Using information from McCreary [28] and assistance from Ramirez [52], the mixing and casting process evolved from hand mixing and casting into cylindrical aluminum molds to mixing on a Resodyne LabRAM (original model) under vacuum and casting into 3D printed, enamel-coated block molds. Through this process development, sample quality improved significantly. Initially, hand-mixed fuel samples were difficult to cast into the 6-inch long, 0.25-inch diameter aluminum strand molds because the mix would adhere to the sides of the mold rather than flow down. These samples were also full of air bubbles because the other big challenge was outgassing. Many air bubbles form when mixing small 8-10g batches by hand. While the mix was placed inside a vacuum jar after mixing and then again after casting into the molds, samples remained porous. The long and thin strand molds had a small surface area for bubbles to escape; often, the material was pushed out of the top of the mold, resulting in samples with large voids. The samples were also difficult to remove from the molds. While multiple coats of Teflon mold release spray aided some, the samples would somewhat stick to the sides of the mold and tearing occurred when attempting to open the mold.

To mitigate these issues, a new mold needed to be designed, one with more surface area for air bubbles to escape, which resulted in the design of a block mold that was 3D printed in PLA (polylactic acid) (Figure 3.5). This mold was modified depending on batch size and sample type. The mold was coated with two coats of RUST-OLEUM® Ultra-Cover Flat Gray Primer and 1 to 2 coats of RUST-OLEUM® Crystal Clear Enamel to prevent adhesion and allow for the propellant block to be removed cleanly.

However, hand mixing and casting into these block molds was still difficult due to the mix's high viscosity and short pot life. This issue led to the discovery that the curative initially used, MDI (methylene diphenyl diisocyanate), for the HTPB was curing too fast and generating bubbles; switching to an IPDI (isophorone diisocyanate) curative resulted in less bubble formation, and outgassing under vacuum was successful. Fuel samples were then cured in an oven at 60°C for a few days depending on batch size. Finally, the blocks were cut into 0.375"(9.52mm) by 0.375"(9.52mm) by 1.50"(38.10mm) strands. The full procedure is included in Appendix C.

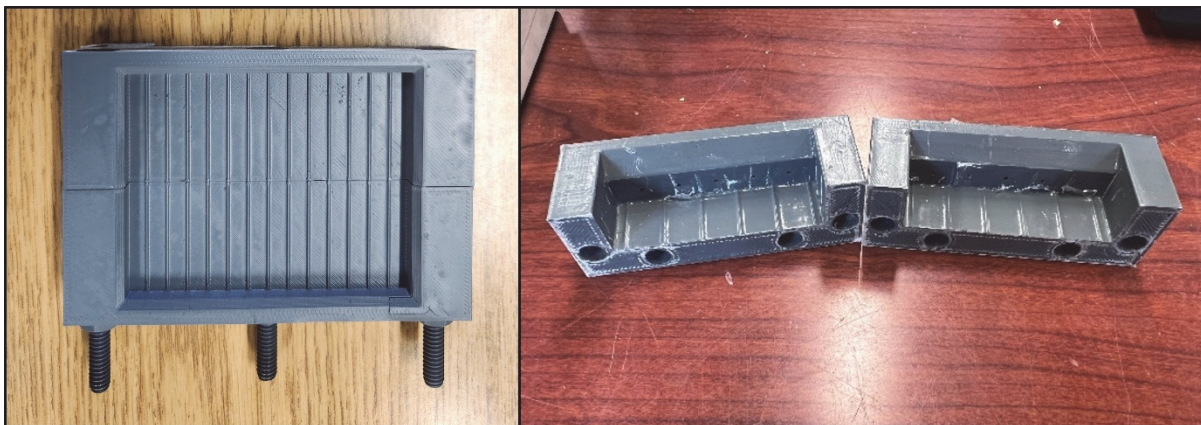


Figure 3.5: Block sample mold prepped for casting (left). Sample mold taken apart after sample removal (right). Samples are cut from the cured block.

For the propellant samples, the high solids loading made it too difficult to hand mix properly, so a procedure was developed for mixing on a Resodyne LabRAM (an acoustic mixer). The mixing procedure comes from a work by Claydon et al. [53-54] in which he investigated using a Resodyne LabRAM for mixing polymer bonded explosives. Claydon defines three stages of mixing: Mix, Bulk Motion, and Flat Line [53-54]. These stages are monitored through a live plot of intensity percentage versus time (Figure 3.6). The intensity of the Resodyne LabRAM scales with number of Gs applied to the mixture. During the Mix phase of the process, the intensity is ramped up and has many oscillations as the particles are wetted and begin to create shear layers [53-54]. The oscillations are a result of viscosity changes in the mixture, when it is less viscous, less power is required to move the particles. The Bulk phase enters when the average intensity remains fairly constant with oscillations [53-54]. The Flat Line phase shows a great reduction in oscillations and represents a homogenous mixture, this means that the entire mixing process is complete [53-54]. Throughout the mixing process, it is important to note that temperature will rise because friction between the moving particles generates heat (Figure 3.6). The elevated temperature, if kept below the decomposition temperature of the propellant mix, is advantageous for casting, as the mixture is less viscous when heated.

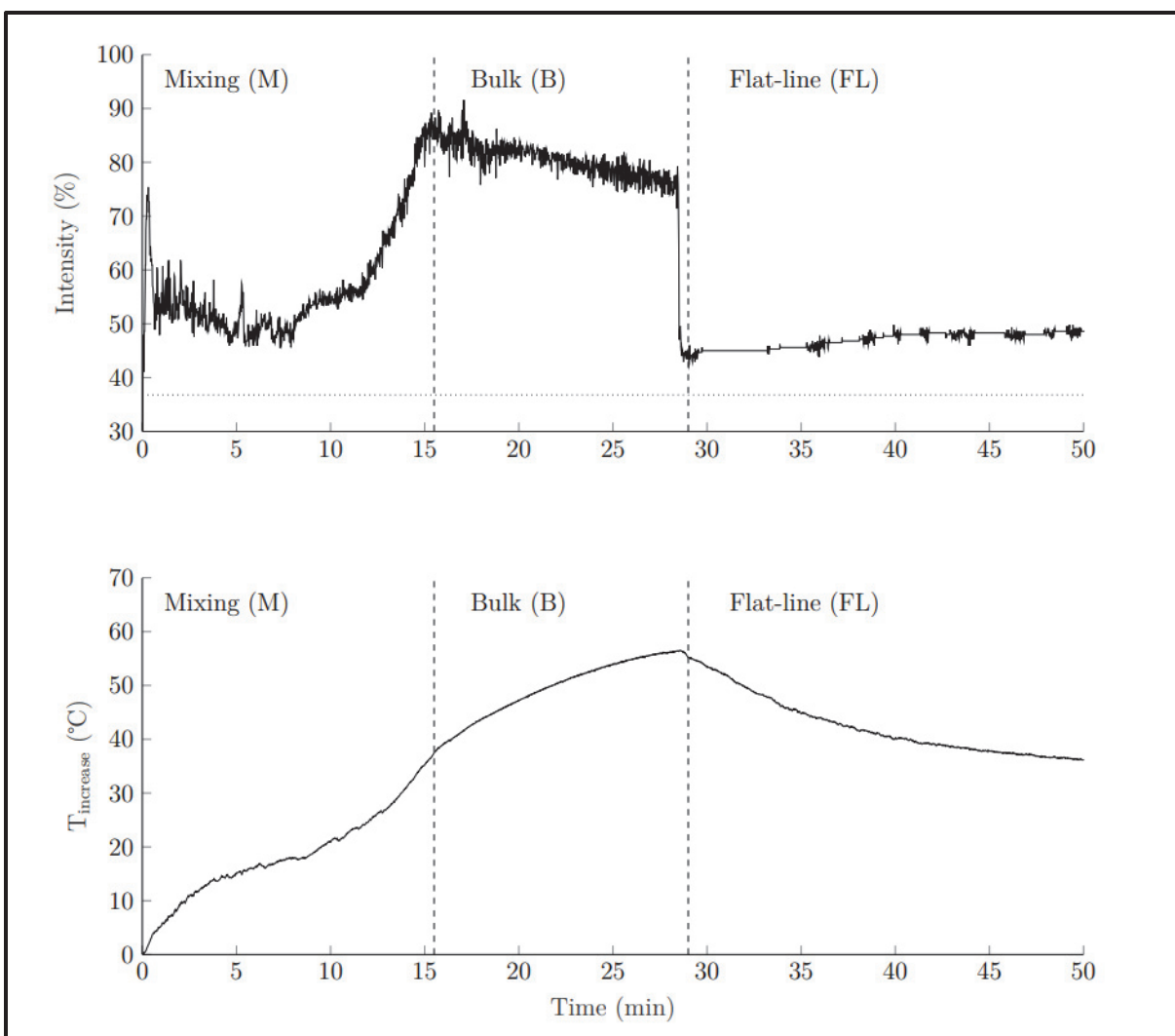


Figure 3.6: LabRAM intensity versus time and temperature versus time data from Claydon's thesis for mixing polymer bond explosives. These show the general trends for each phase of the mixing process, but the exact behavior will differ depending on the formulation being mixed [53].

Propellant samples used by this study were mixed in Anti-Static Pink Propylene ESD safe containers (from LACONTAINER) with a Resodyne LabRAM (original model) under vacuum and cast into 3D-printed PLA molds, which were enamel-coated to prevent adhesion. One example of the live intensity versus time data is provided in Figure 3.7. Currently, temperature data could not be recorded, but work is being done to add this capability to the setup. Propellant samples were cut into 0.250"(6.25mm) by 0.250"(6.25mm) by 2.50"(63.50mm) strands. The full mixing and casting procedure is in Appendix C.

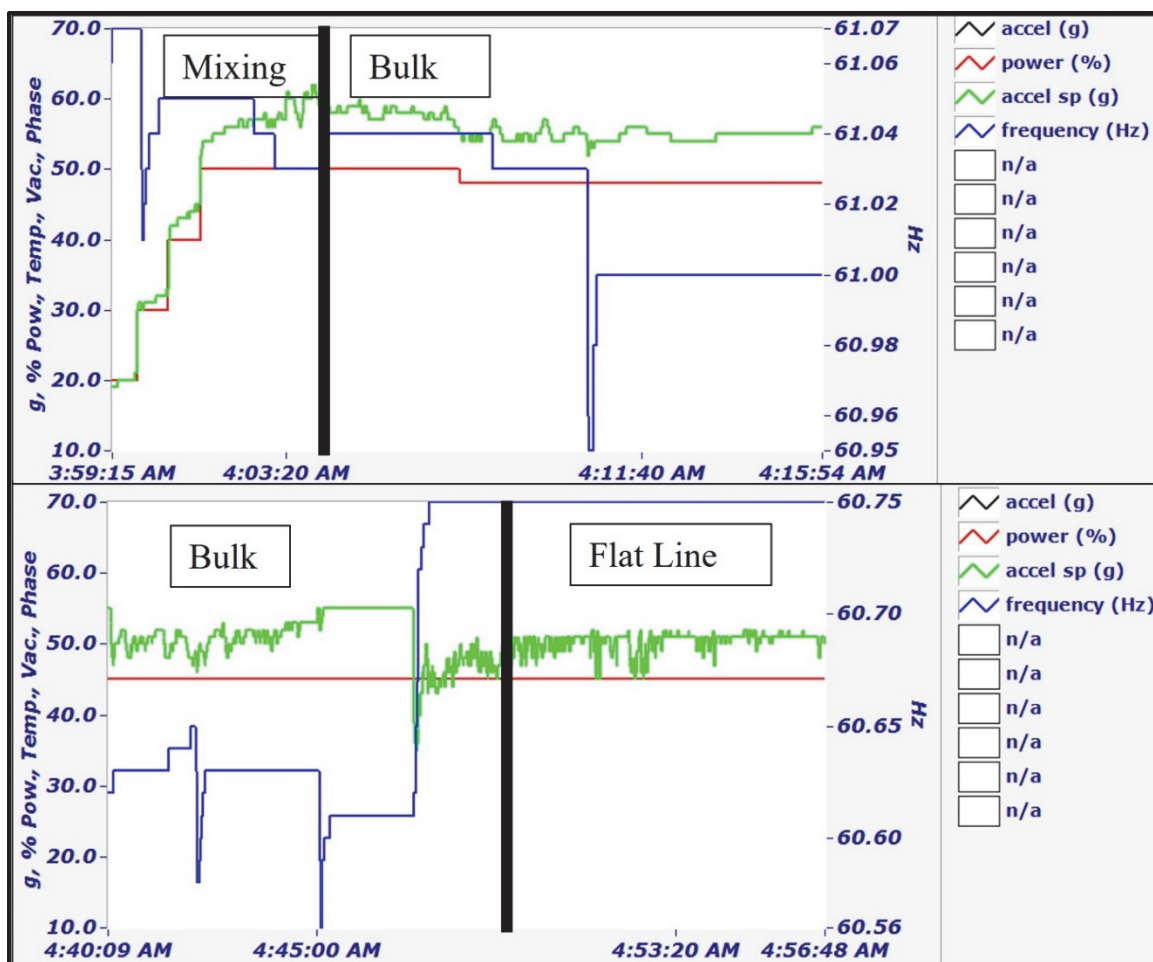


Figure 3.7: Intensity versus time data from the LabRAM during the beginning of the mixing procedure (top) and the end of the mixing procedure (bottom). The three phases of the process are marked.

3.2 Experimental Setup

3.2.1 Heating Test Setup

Experiments were performed using two different induction heaters, the first an MTI 25kW SP-25A Desktop induction heater capable of producing a strong magnetic field at frequencies ranging from 30-80kHz (frequencies adjust based on input current) (Figure 3.8). The MTI induction heater utilized a seven-turn, 2.5in diameter solenoid coil to generate the magnetic field. COMSOL Multiphysics 6.0 was used to simulate the magnetic field. The model showed that the field is most uniform at the center of the coil, and it estimated the magnetic field strength ranges from 220-880Oe, which is inversely related to the excitation frequency. The general heating test setup with the MTI heater is shown in Figure 3.9. The standard operating procedure (SOP) for this heater is in Appendix C.1.



Figure 3.8: MTI SP25 Desktop induction heater.

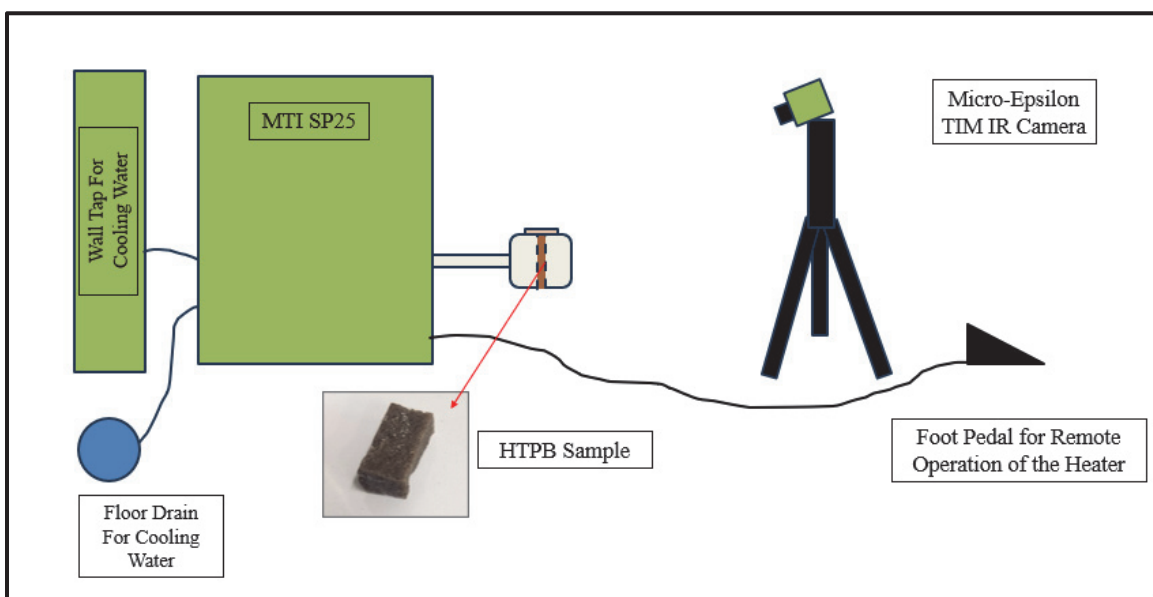


Figure 3.9: Simple model of general heating test setup with the MTI SP25 Induction Heater.

The second induction heater is an UltraFlex SB-3/1200, which produces a weaker field at a much higher frequency (789kHz) than the MTI. The frequency of this heater remains constant for all input current settings. The UltraFlex heater utilizes a two-turn ellipse-shaped coil to generate the magnetic field (Figure 3.10). The UltraFlex coil was also modeled in COMSOL Multiphysics 6.0 to estimate the magnetic field strength. Like the MTI coil, the field is most uniform in the center. The field strength was found to vary from 8-12Oe depending on the amperage of the input current. Further discussion of the results of the COMSOL models can be found in Section 4.1. Figure 3.11 shows a model of the general heating test set up with the UltraFlex heater. The SOP for this heater is in Appendix C.2.



Figure 3.10: Heating station with coil portion of the UltraFlex SB-3/1200 heater. This heater also comes with a power supply and water cooler.

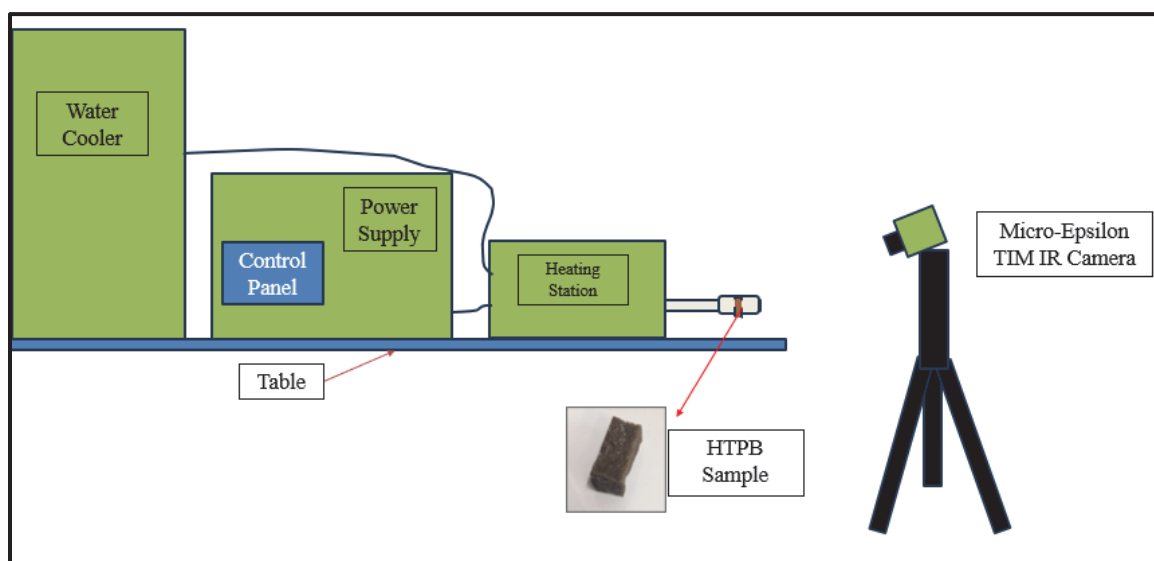


Figure 3.11: Simple model of general heating test setup with the UltraFlex SB-3/1200 Induction Heater.

A Micro-Epsilon TIM 160 long-wave infrared camera captured surface temperature measurements with a 23-degree lens and an emissivity setting of 0.9. The emissivity value was selected as the known emissivity of polyurethanes (similar polymer to HTPB) [55]. Most polymers have an emissivity from 0.9-0.97, with rubbers generally having an emissivity close to 0.9 [55]. Internal temperatures could not be measured directly because the magnetic field interacts with traditional thermocouples. Surface temperature measurements were limited to raw powder and fuel sample heating tests due to the peak temperature limit of the thermal camera (1000°C).

3.2.2 MNP Propellant Burning Rate Experimental Setup

Burning rate tests were performed on the propellant samples with embedded MNPs to observe dynamic changes in the burning rate when IH was applied. Because typical lead break wires interact with a magnetic field and the induction heater's coil blocks a camera's view of a portion of the sample, a novel approach for measuring burning rate using fiber optic break wires was attempted. While the concept remains promising, the setup required further optimization and could not be used for this testing. A discussion of this method is provided in Appendix E.

Instead, image analysis of video captured by a Photron FASTCAM SA4 determined the propellant burning rates. While only a few points above and below the coil can be seen, this optical method gives a decent measurement of relative changes in burning rate between the heated and non-heated sections of the propellant grain. This testing used the UltraFlex induction heater on the 15A, 15s setting. A thin coat of halocarbon grease was applied to the sides of each sample as an inhibitor to prevent flame spreading down the sides of the strand which allows for a flat burn on the top surface that can be easily tracked for burning rate measurements. Each sample was then placed inside a borosilicate glass tube, which was used to hold the sample and protect the induction coil. The sample was placed on a test stand which was designed for routing lead break wires and nichrome igniter wire. The first lead break wire was used for triggering the camera and the second for turning on the induction heater. Figure 3.12 shows a test stand model with a sample in place and the UltraFlex heater's coil. Figure 3.13 is a cross sectional image of the test setup.

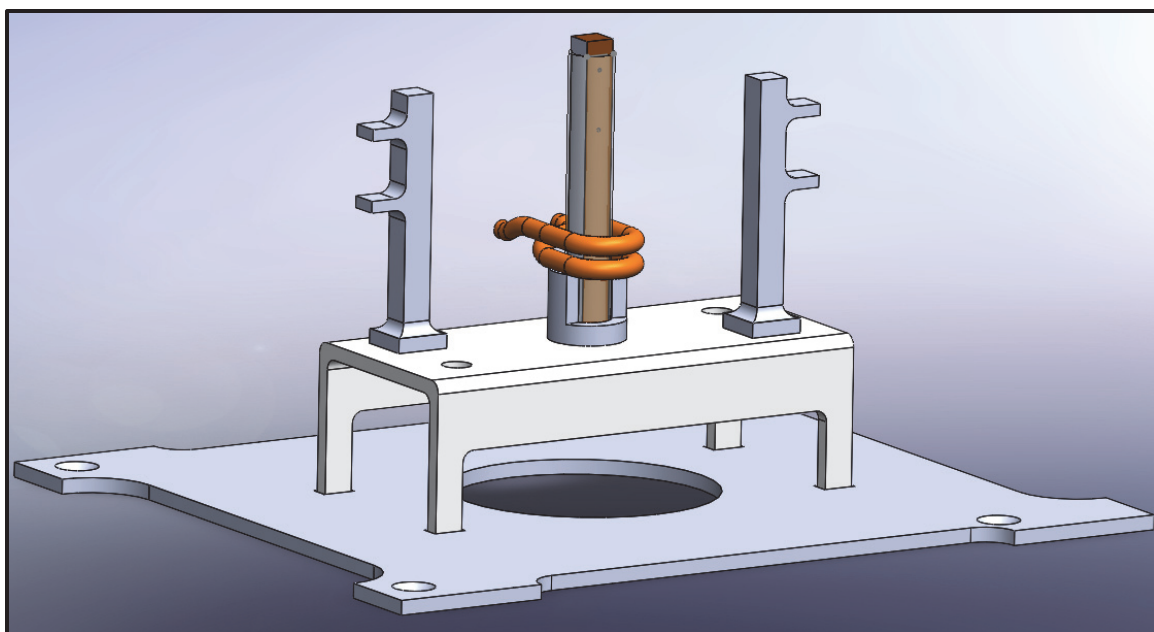


Figure 3.12: SolidWorks model of the test stand with a sample in place and the UltraFlex coil.

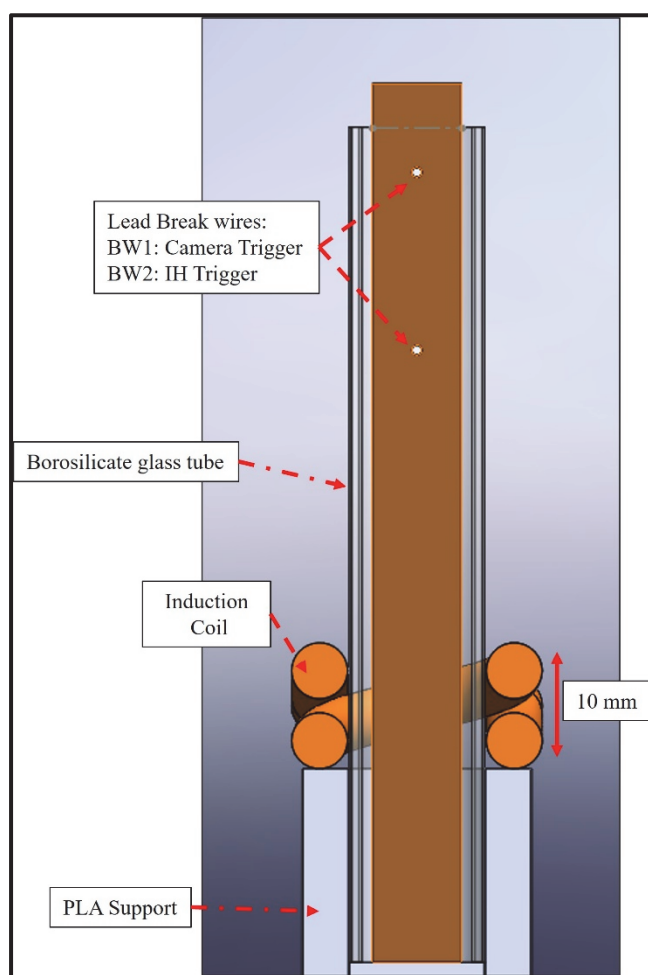


Figure 3.13: Cross sectional image of the test setup from the SolidWorks model.

3.3 COMSOL Model Setup

3.3.1 Magnetic Field Generated by MTI Coil

The purpose of this simulation is to estimate the magnetic field strength produced by the MTI induction heater's coil based on the excitation current strength and frequency. This heater allows for a selection of current inputs from 200A to 800A; as the current strength increases, the frequency decreases, and generated magnetic field strength should increase. However, there is no clear method for measuring output magnetic field strength, so modeling the coil was the best option for estimating the generated magnetic field. COMSOL has two options for building a geometry: the CAD kernel and the COMSOL kernel. For this model, SolidWorks was used to build the coil geometry, and that file was imported to COMSOL as a .stp file via the CAD kernel. A box was built around the coil using the internal geometry tools (Figure 3.14). This box constrains the simulation by providing maximum limits on the simulation volume. It also represents the air domain surrounding the coil.

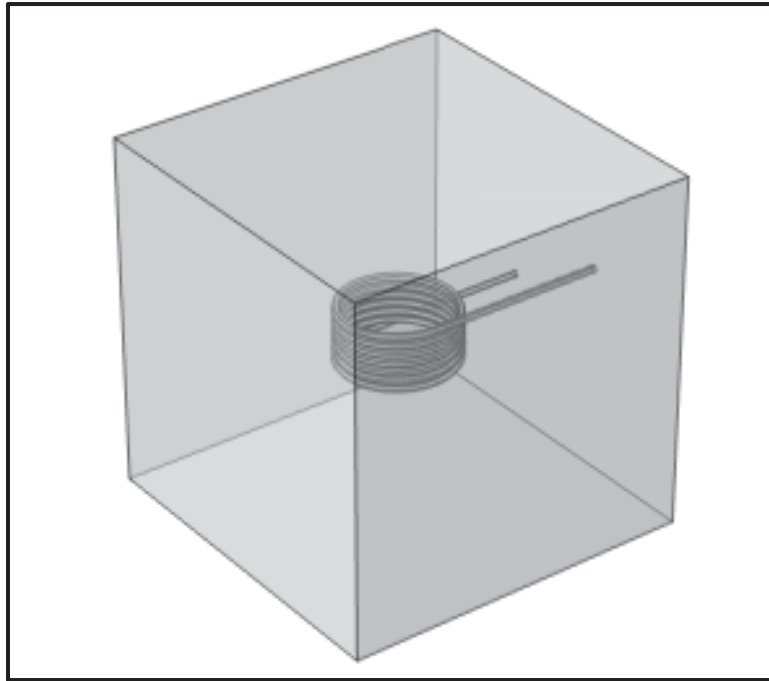


Figure 3.14: MTI coil COMSOL model geometry.

Materials are assigned to each domain and face. The box is air, and the coil is copper. COMSOL has an internal library of materials with properties but also has the capability for the user to define their material properties. For this model, the internal library was used. The properties used by COMSOL are listed in Table 3.4. COMSOL determines which material properties are needed based on the selected physics interfaces. This model uses the *Magnetic Fields (mf)* interface where there are multiple options for selecting domain parameters, including initial conditions, boundary conditions, and equations to apply. The

model defines *Ampere's Law* to be used throughout the air domain and assigns the copper domain to the *Coil* function. The *Coil* function allows the user to select the type of coil, the coil excitation parameters, and define the input and output terminals for the current. This model used current excitation with values ranging from 200-800A. The selected input and output terminals are the flat faces on the ends of the coil. The initial values are set to no current running through the coil and nominal ambient air conditions (22°C). The edges of the air domain are selected as magnetic insulations to constrain the size of the simulation to the size of the air domain box.

Table 3.3: Material Properties for MTI Coil COMSOL Model

Air	
Electrical Conductivity (S/m)	0
Relative Permittivity	1
Relative Permeability	1
Copper	
Electrical Conductivity (S/m)	$5.998 * 10^7$
Relative Permittivity	1
Relative Permeability	1

After building the geometry, selecting the physics interface, and defining parameters, the mesh is set, and the study conditions are selected. The model was simple enough to use COMSOL's auto-generated mesh defined by the chosen physics. This option allows for user selection of mesh size, but not shape. The model uses the *normal* mesh size. Basic study options include transient, stationary, frequency domain, and combinations of the three. For this model, a frequency domain study was performed with an initial step of *Coil Geometry Analysis*, which tells COMSOL to define the coil before proceeding with the simulation. The frequency domain study allows the user to define one or multiple frequencies. Frequencies ranging from 30-80kHz were tested. The model was set to produce the magnetic field strength across MTI induction heater current and frequency range. The results are in Section 4.1.1.

3.3.2 Magnetic Field Generated by UltraFlex Coil

The model for the UltraFlex coil's generated magnetic field was built in a similar way to the MTI coil model. The coil geometry was built in SolidWorks and imported to COMSOL as a .stp file. A box was built around the coil to constrain the simulation volume and air domain (Figure 3.15). The materials used were air for the box and copper for the coil, with the same properties as shown above in Table 3.3. The *Magnetic Fields (mf)* physics interface was used, with *Ampere's Law* defining the air domain and the *Coil* function defining the copper domain. The coil type selected was current excitation with set currents of 6 and 15 amps.

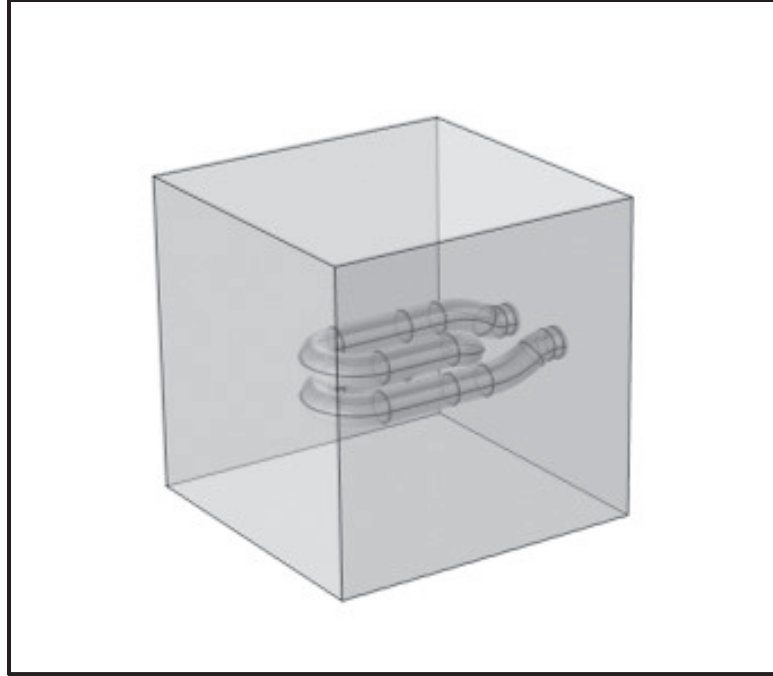


Figure 3.15: COMSOL model of UltraFlex coil geometry and the surrounding box representing the air domain.

The flat faces at the end of the coil were selected as current input and output terminals. The faces of the air domain box were set to the *Magnetic Insulation* boundary condition to constrain the simulation volume. The small coil required finer mesh size compared, so a completely user-defined mesh was created. In the air domain, a coarse-sized tetrahedral mesh was used. For the coil, a finer-sized tetrahedral mesh was used. These selections allowed for the smaller coil to be well-defined without generating a larger number of unnecessary nodes in the air domain. A frequency domain study was run with an initial *Coil Geometry Analysis* step. Unlike the MTI heater, the current frequency remains 789kHz for both current strengths, so this was the selected frequency for the study. The results are in Section 4.1.2.

3.3.3 Heat Transfer Through Fuel Samples

A model of the hysteresis fuel samples was developed to simulate the heat transfer through an HTPB fuel grain with embedded MNPs. The geometry for this model was built using the internal COMSOL kernel. It consists of three stacked cylinders representing the entire fuel sample but distinguishes between the sections of the sample inside versus outside of the induction coil (Figure 3.16). This separation is important because heat will only be generated inside the section of the sample that sits inside the induction coil. The overall modeled grain dimensions are 6.35mm diameter by 37mm long. The center segment is 10mm in length, the upper and lower are 13.5mm long.

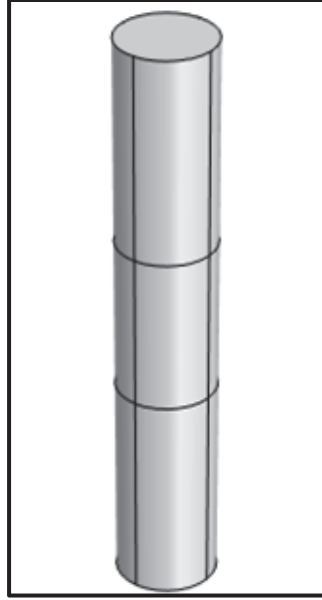


Figure 3.16: Hysteresis fuel sample COMSOL model geometry.

The material for all three domains is HTPB, which was user-defined. This approximation was selected because the COMSOL graphical user interface (Gui) cannot accurately resolve dispersed nanoparticles, as the particles would be smaller than the mesh. It is assumed to be a good approximation because the weight percentage of MNPs is very small compared to that of HTPB and the MNPs are uniformly dispersed. The material properties used by this study are shown in Table 3.4

Table 3.4: Material Properties for Hysteresis Fuel Sample COMSOL Model.

HTPB		Refs
Thermal Conductivity (W/(m*K))	0.283	[56]
Specific Heat Capacity (J/(kg*K))	2000	[57]
Density (kg/m³)	920	[58]
Emissivity	0.9	[55]

The physics interface used for the model is *Heat Transfer in Solids*. The governing equation used by the selected physics interface is the transient heat conduction equation (Equation 3.1) where ρ is material density, C_p is specific heat, T is temperature, t is time, \mathbf{u} is the velocity vector, k is thermal conductivity, and $Q + Q_{\text{ted}}$ represents source terms.

$$\rho C_p \frac{\partial T}{\partial t} + \rho C_p \mathbf{u} \cdot \nabla T + \nabla \cdot (-k \nabla T) = Q + Q_{\text{ted}} \quad \text{Equation 3.1}$$

For this model, the initial conditions are selected as 22°C which was the initial temperature recorded during hysteresis heating tests. A convective heat flux boundary condition with a natural

convection heat transfer coefficient of $5 \text{ W}/(\text{m}^2 \cdot \text{K})$ was applied to all outer faces [59]. A radiation boundary condition called *Surface to Ambient Radiation* was also applied to the outer faces. Since the source of heat generation will be from the dispersed MNPs inside the portion of the sample enclosed by the induction heater's coil, the heat source was selected as a volumetric internal heating rate for the center cylinder domain. The heating rate is in units of watts and can be defined as a constant value or an equation. For this model, a constant value was selected based on the estimated heating power generated by the MNPs. The value was informed by experimental results and differed depending on what MNP weight percentage was being simulated. The mesh of the model was chosen to be a fine-sized, physics-controlled, automatically defined mesh. This mesh was chosen because the geometry is simple enough to be accurately modeled by the autogenerated mesh and small enough that a fine mesh can be used without significantly impacting solving time. A transient study was run to simulate the fuel sample heating test conditions, which were a 15A excitation current for 15s inside the UltraFlex coil (same current strength and amount of time used during experimental heating tests). The study allows surface temperature to be tracked versus time, which can be easily compared to the experimental surface temperature data measured with an IR camera. The results of this simulation are in Section 4.1.3.

Chapter 4

RESULTS AND DISCUSSION

4.1 COMSOL Model

4.1.1 Magnetic Field Strength Produced by MTI Induction Heater

Recall from Section 3.3.1, the model of the MTI coil (63.5mm diameter by 47mm long) was developed to estimate the magnetic field strength generated by the induction heater on various current settings. The model was operated using the *Magnetic Fields (mf)* physics interface and a frequency domain study was performed. The simulation was run for the following current excitation values: 200, 300, 400, 500, 600, 700, and 800A. It was run with estimated corresponding frequencies ranging from 30-80kHz where the higher the current the lower the frequency. This relationship is a product of the way the MTI induction heater's electronic system is designed, there is a balance between the inductance of the coil, the amperage of the current, and the frequency of the current. The COMSOL model returns a 3D simulation of the magnetic field lines, with a color table corresponding the magnetic flux density throughout the field (Figure 4.1). It can be observed that the magnetic field lines are most uniform at the center of the coil which was expected.

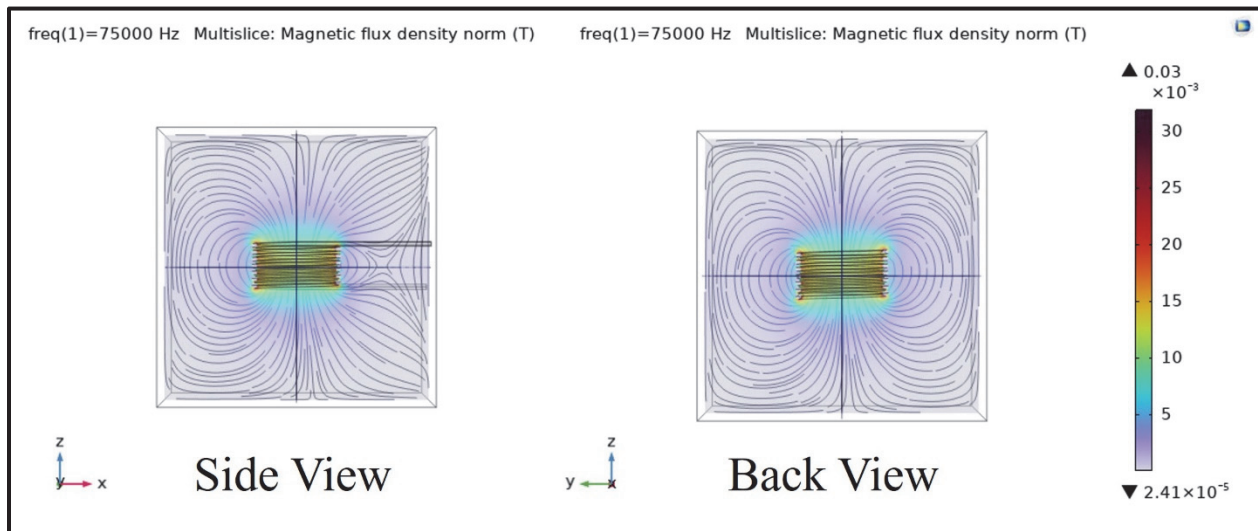


Figure 4.1: COMSOL simulation of magnetic flux density and magnetic field lines for MTI coil.

The strength of the field and the magnetic flux density at the center of the coil for each current excitation was also found by this simulation. The resulting values are shown in Table 4.1. It is observed that field strength varies linearly with excitation current. Attempts were made to develop this model further, by including the *Heat Transfer* physics interface and the *Induction Heating* Multiphysics interface, but this

proved difficult. The model struggled to converge when a frequency domain study with the Multiphysics interface was used.

Table 4.1: Magnetic Flux Density and Magnetic Field Strength Values of the MTI Coil for Various Excitation Currents

Current (A)	Frequency (kHz)	Magnetic Flux Density, B (T)	Magnetic Field Strength, H (Oe)
200	80	0.022	220
300	72.5	0.033	330
400	64	0.044	440
500	55.5	0.055	550
600	47	0.066	660
700	38.5	0.077	770
800	30	0.088	880

4.1.2 Magnetic Field Strength Produced by the UltraFlex Induction Heater

A COMSOL model was also developed to estimate the strength of the magnetic field generated by the UltraFlex induction heater. The complete model setup is described in Section 3.3.2. To summarize, the model utilized the *Magnetic Fields (mf)* physics interface, and a frequency domain study was performed. The purpose of this simulation is twofold, to characterize the magnetic field strength and the uniformity of the generated field. The UltraFlex heater's coil is much smaller than the MTI coil. It is a 2-turn coil, about 10mm in length while the MTI coil is 7-turn, about 47mm in length. Smaller coils generally have less uniform magnetic fields because the area inside the coil is small, and the toroidal field wants to wrap around the coil at the edges. The COMSOL simulation was used to understand at what point inside the coil the magnetic field uniformity and strength begins to drop off. During the experimental work, the samples were placed at the center of the coil in an attempt to stay within the most uniform area. This simulation was run for both current settings of the heater, 6A and 15A (both settings operate at a frequency of 789kHz). Figure 4.2 shows the magnetic field lines and magnetic flux density generated by the UltraFlex heater's coil on the 6A setting. Figure 4.3 shows the equivalent results for the 15A case. It is observed that the field shape does not change between the two settings, but the magnetic flux density value does.

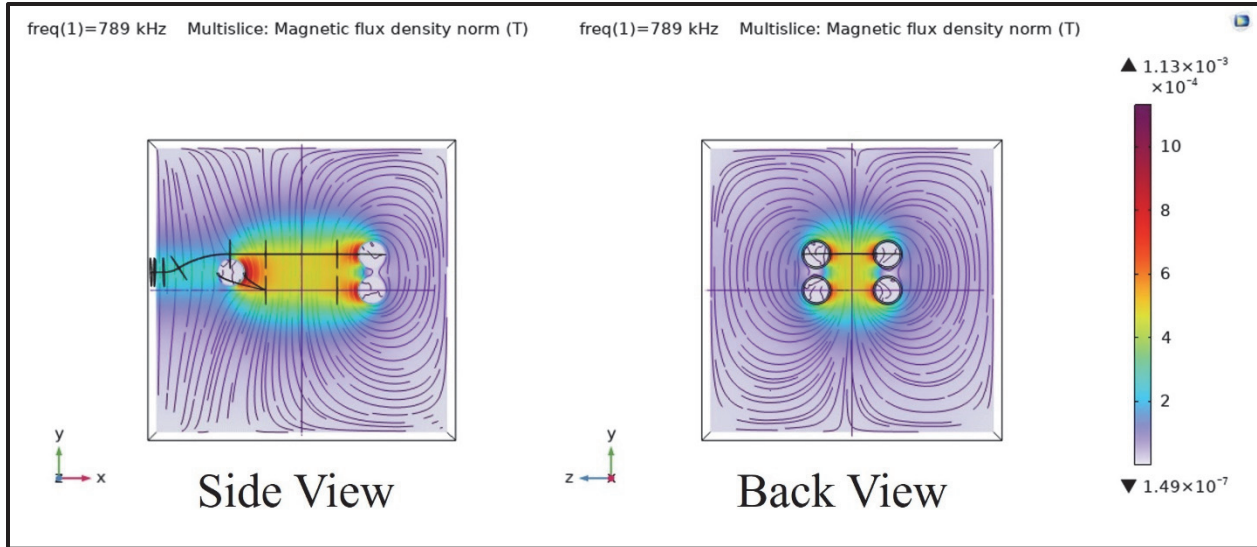


Figure 4.2: Side and back views of magnetic field lines of UltraFlex coil on 6A setting with 789kHz frequency. Note: this is a wire frame diagram of the coil.

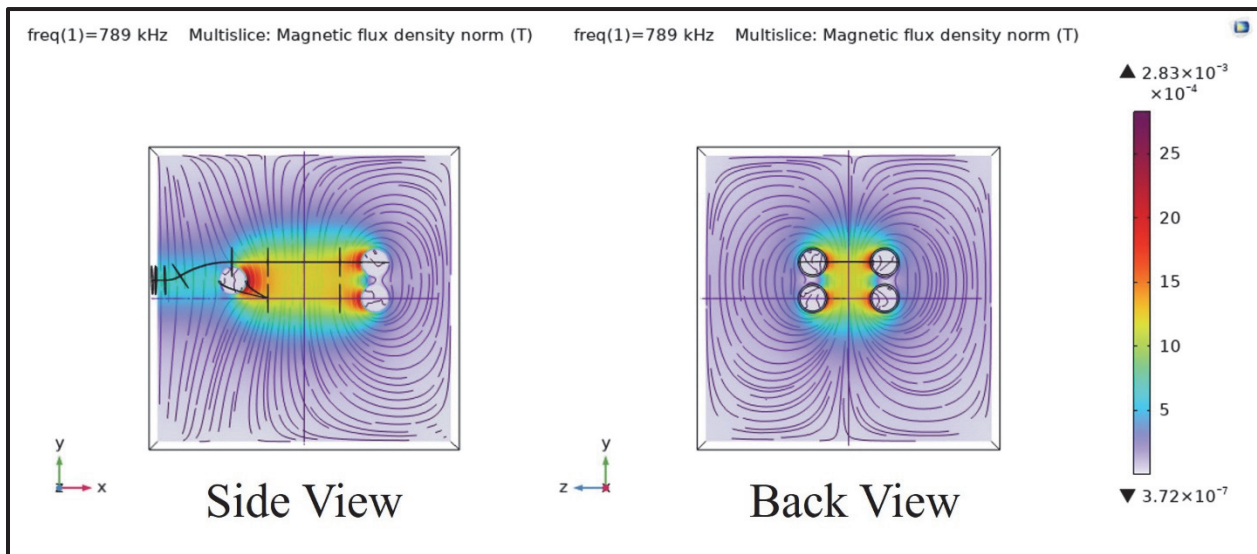


Figure 4.3: Side and back views of magnetic field lines of UltraFlex coil on 15A setting with 789kHz frequency. Note: this is a wire frame diagram of the coil.

A frequency domain study was also performed for 100-900kHz. While the heater only operates at 789kHz, there was interest in understanding how the magnetic field strength is affected by excitation current frequency. This information was also used to understand how magnetic field strength changes along the length of the centerline of the coil (Figure 4.4). Figures 4.5 (6A case) and 4.6 (15A case) are plots of magnetic field strength versus location along the coil's centerline for various frequencies. It is observed that as frequency increases field strength decreases, and this relationship is not linear. The estimated magnetic field strength for the 6A case at 789kHz is 4.75Oe (378A/m). For the 15A case the field strength is estimated to be 12Oe (955A/m). It is also observed that the magnetic field strength is not uniform for the

entire length of the coil. For both cases, it is most uniform for the middle 4mm section and weakens through the upper and lower 3mm of the coil. This is a product of the small coil length. The uniform section would be greater on a longer coil.

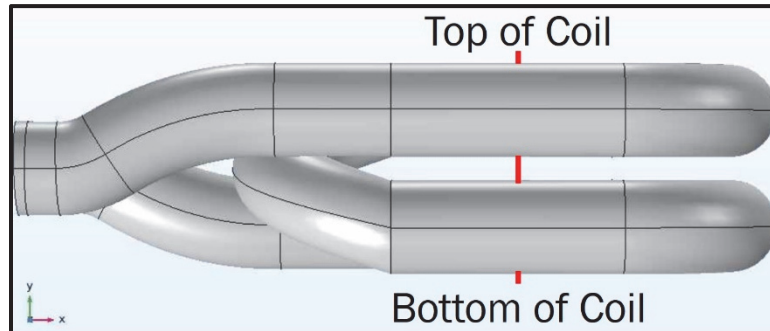


Figure 4.4: Centerline of the UltraFlex coil used for gathering the data displayed in the following two figures.

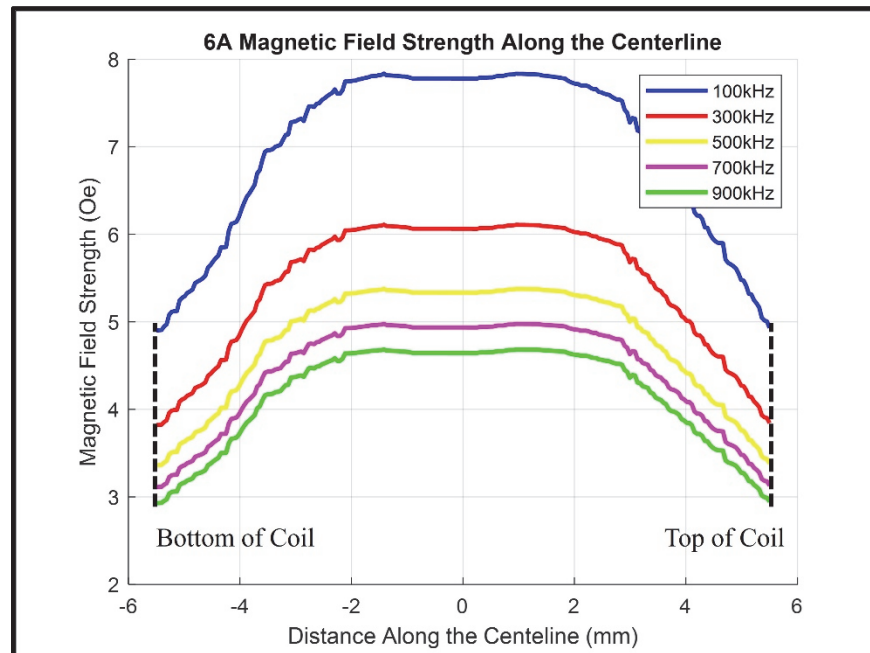


Figure 4.5: Magnetic field strength along the centerline for the 6A setting of the UltraFlex coil for multiple frequencies.

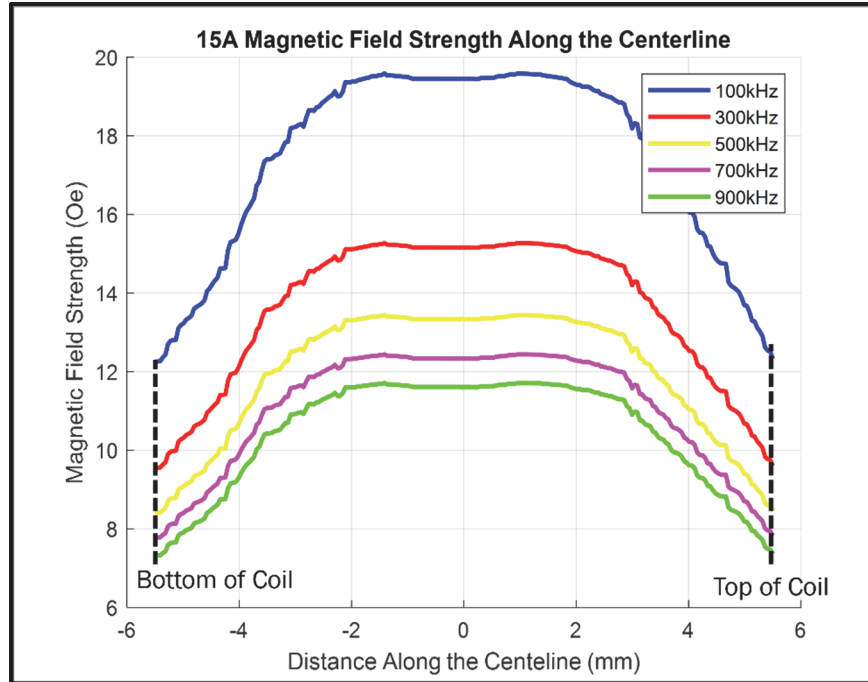


Figure 4.6: Magnetic field strength along the centerline for the 15A setting of the UltraFlex coil for multiple frequencies.

4.1.3 Hysteresis Fuel Sample Heat Transfer Model

Recall from Section 3.3.3, the heat transfer fuel grain model was developed to estimate heating power required to achieve a specified surface temperature value after 15s. This simulates a sample in the UltraFlex heater for 15s on the 15A setting. The model assumes a grain with the physical properties of HTPB alone, because COMSOL has difficulties dealing with dispersed nanoparticles. Both natural convection and radiation were used as boundary conditions for all outer surfaces of the grain. The simulation was run with an internal constant heating rate applied to the center segment of the grain which acts as the section inside the coil. The heating rate was iterated upon until a desired surface temperature was achieved. The temperature values were based on experimental results from heating tests of the 1wt%, 2.5wt%, and 5wt% magnetite samples on the UltraFlex heater for 15s on the 15A setting (see Section 4.3.1). Figure 4.7 shows the 2.5wt% fuel sample model at its initial condition, along with sample dimensions and variables used for boundary conditions. In Figure 4.7, h is the convective heat transfer coefficient, ϵ is emissivity, and q_{gen} is the constant internal heating rate. Figure 4.8 shows the surface temperature of the 2.5wt% fuel sample at multiple time steps from 0 to 15s. It is observed that the heating stays localized to the center of the grain which matches the behavior seen in experiments.

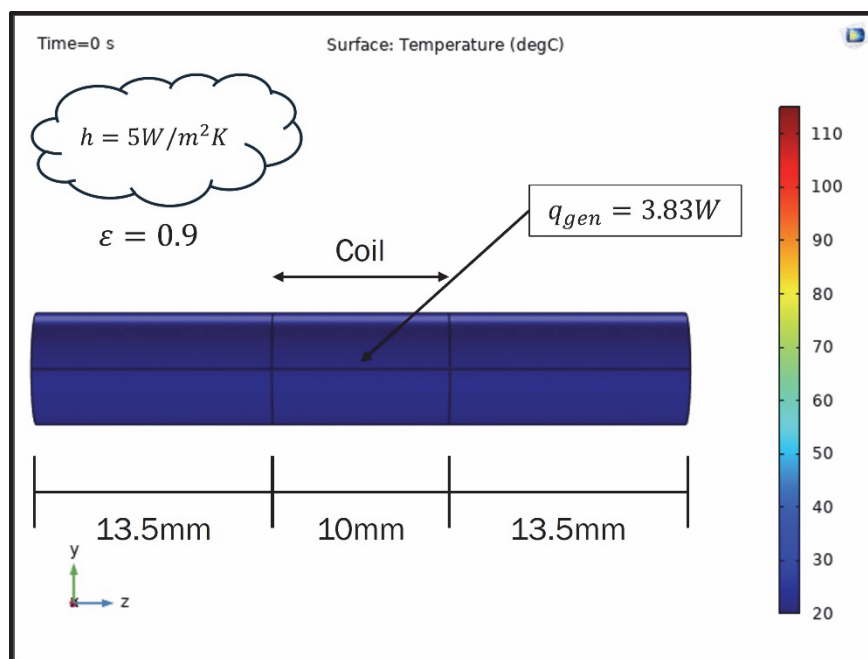


Figure 4.7: Surface temperature model setup for simulated 2.5wt% heating in the UltraFlex Coil for 15s on the 15A setting. The dimensions of the sample, location of the coil, and boundary condition variable values are included.

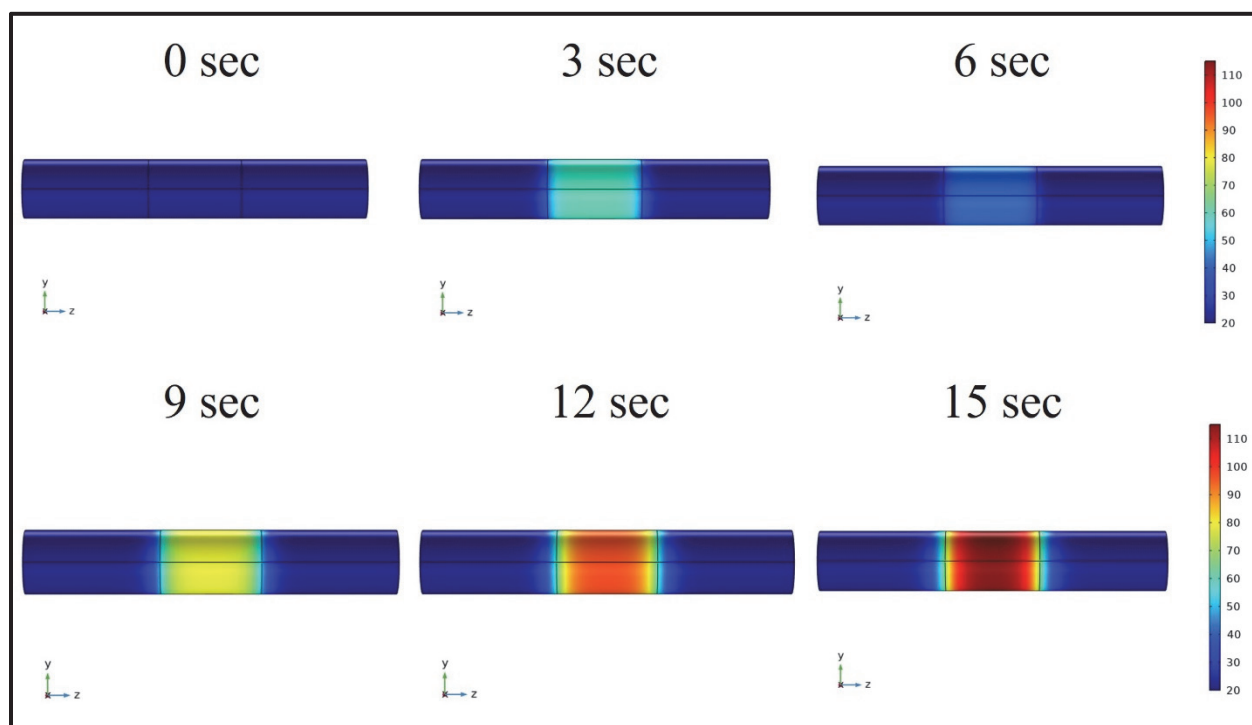


Figure 4.8: Surface temperature model at different time steps for the simulation of the 2.5wt% magnetite hysteresis fuel samples assuming the 15A, 15s UltraFlex heater settings.

Table 4.2 displays the surface temperature at 15s and the estimated heating power from experiment and the COMSOL simulation for each weight percentage of magnetite. The experimental surface temperature

values were measured with an IR camera, assuming an emissivity of 0.9 [55] (see Section 4.3.1). The heating power was calculated assuming no heat loss (see Section 4.3.1). There is agreement between the experimental results and the COMSOL model, however, as discussed in Section 4.3.1, the constant heating rate assumption made by the model is not accurate. Néel relaxation plays a role in the heating rate's nonlinearity. As the sample's temperature increases, the heating rate decreases because more particles begin to have a Néel relaxation time less than the frequency of the UltraFlex heater. In its current state, modeling this behavior is outside the simulation's capability.

Table 4.2: Surface Temperature and Heating Power at 15sec (Experimental and COMSOL Results)

Percentage MNP	Experimental Surface Temperature	Experimental Estimated Heating Power	COMSOL Surface Temperature	COMSOL Estimated Heating Power
1wt%	61.1°C	1.59W	61.1°C	1.63W
2.5wt%	113.5°C	3.66W	113.5°C	3.83W
5wt%	159.1°C	5.70W	159.2°C	5.78W

4.2 MNP Raw Powder Characterization Heating Tests

To determine the baseline heating capability of the MNP, about 100 mg of material was placed into a 3D-printed PLA sample holder that held the powder in the center of the induction coil. The magnetic field produced by an induction coil is most uniform in the center (as shown by the COMSOL model results); therefore, this location in the coil will exhibit the most uniform heating. MNPs were characterized in both induction heaters, but only results for magnetite are shown in the UltraFlex heater since zinc and cobalt ferrite did not exhibit significant heating. Magnetite demonstrated the best relative heating potential of all the metal ferrites in the MTI and Ultraflex heaters (Figures 4.9 and 4.10). As expected, when tested in the Ultraflex heater, the heating was significantly increased due to the higher magnetic field frequency.

Since zinc ferrite is considered a soft magnet (low coercivity), it is readily magnetized; thus, the hysteresis loop area is small compared to the other "harder" ferrites explored. This magnetization behavior is seen by the lack of change in heating behavior when subjected to increasing magnetic field strengths (Figure 4.9, Right). Cobalt ferrite coercivity is significantly greater than magnetite and zinc ferrite, requiring a strong magnetic field to generate heat. Given a stronger magnetic field, cobalt ferrite would provide greater heating than magnetite, which is not seen in the results (Figure 4.9, Left). There is possibly a two-fold explanation for this behavior; one, it was discovered that at higher amperages, the MTI heater frequency is halved, thus resulting in a loss of heating potential. The second explanation is the effects of Néel relaxation time. If the Néel relaxation time of the cobalt ferrite particles is less than the alternating period of the MTI heater frequencies, then magnetic hysteresis heating efficiency is greatly reduced. The heating potential of $\gamma - \text{Fe}_2\text{O}_3$ (maghemite) had been previously characterized by Dr. Wang's group for

their self-healing polymer work [60-61] and proved to be a promising candidate; however, magnetite contains an additional iron in its lattice, resulting in more significant heating. Further, previous investigations into MNPs show that magnetite has a more significant heating potential on a volumetric basis than maghemite [60-61]. Given the higher frequency magnetic field of the UltraFlex heater resulting in greater heating potential, all further IH experiments were performed in the UltraFlex heater.

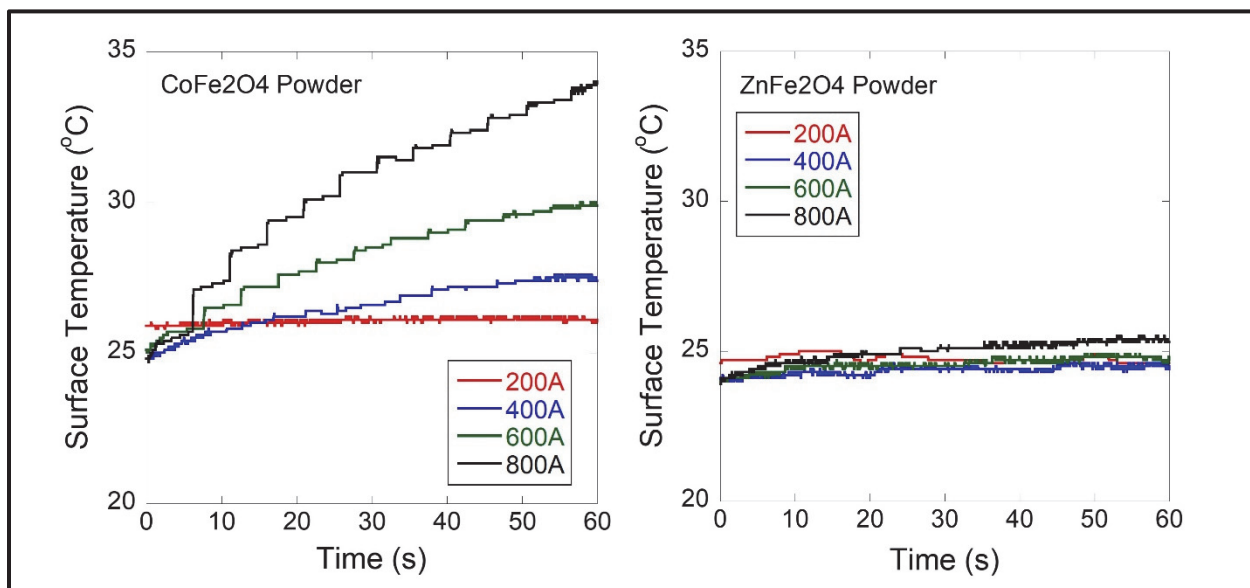


Figure 4.9: Cobalt ferrite (left) and zinc ferrite (right) neat powder thermal characterization in MTI induction heater. Note: The jumping temperature behavior of cobalt and zinc ferrites is a product of initial camera placement and resolution.

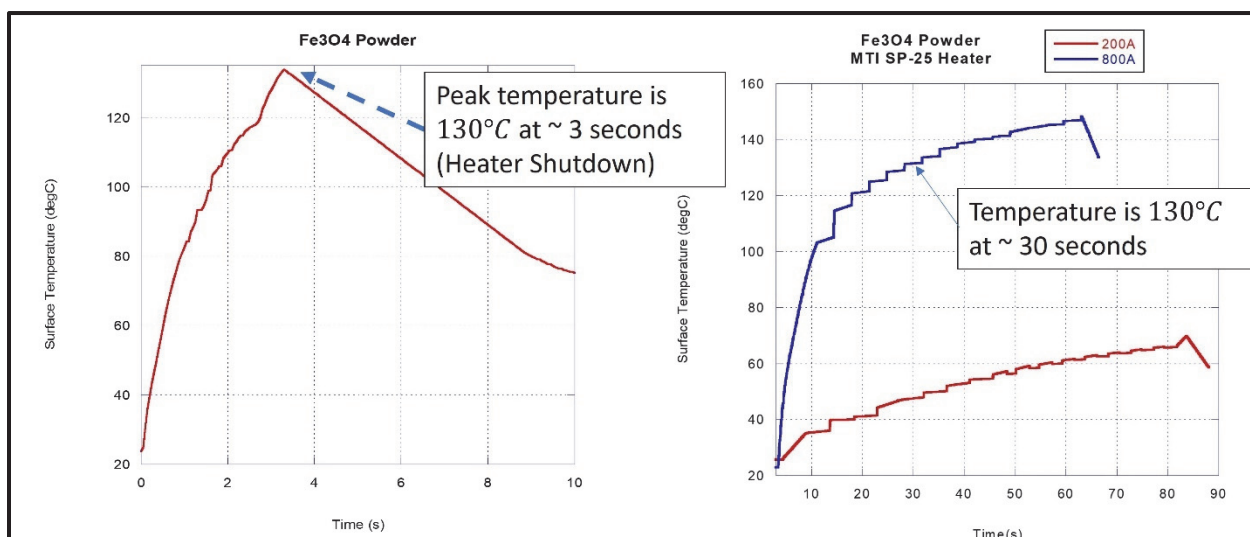


Figure 4.10: Neat powder heating of magnetite in higher frequency UltraFlex heater at 6A (left) and the MTI heater at 200A and 800A (right). The UltraFlex test was halted at three seconds to avoid melting the sample holder.

4.3 Fuel and Propellant Sample Heating Tests

4.3.1 MNP Fuel Hysteresis Heating Tests

Magnetite (Fe_3O_4) MNPs were initially cast into small HTPB cylinders of 0.375 x 1.5in to demonstrate fuel sample magnetic hysteresis heating capabilities. Samples containing 1wt%, 2.5wt%, and 5wt% magnetite were tested on the UltraFlex heater under two conditions (Table 4.3). The first is a 15A setting for 15s (duty cycle limit of higher amperage) which generates a 12Oe (955A/m) field alternating at 789kHz. The second, a 6A setting which produced a 4.75Oe (378A/m) field alternating at 789kHz until a nearly steady state temperature was reached. Varying the weight percent of magnetite has a proportional effect on the maximum temperature achieved in the hysteresis samples. For the 15A/15s samples, heating rate (dT/dt) was also calculated and plotted with surface temperature versus time (Figure 4.11). It is observed that the heating rate is not constant which does not match the constant internal heating rate assumed by the COMSOL model (see Section 4.1.3).

Table 4.3: Heating Data from Hysteresis Fuel Sample Testing

Sample	6 Amp	15 Amp	6 Amp 200 Sec	15 Amp 15 Sec
	65°C time (s)		Max Temp °C	
1wt% Fe_3O_4	165	~17	68	60
2.5wt% Fe_3O_4	35	5	130	115
5wt% Fe_3O_4	13	3	205	157

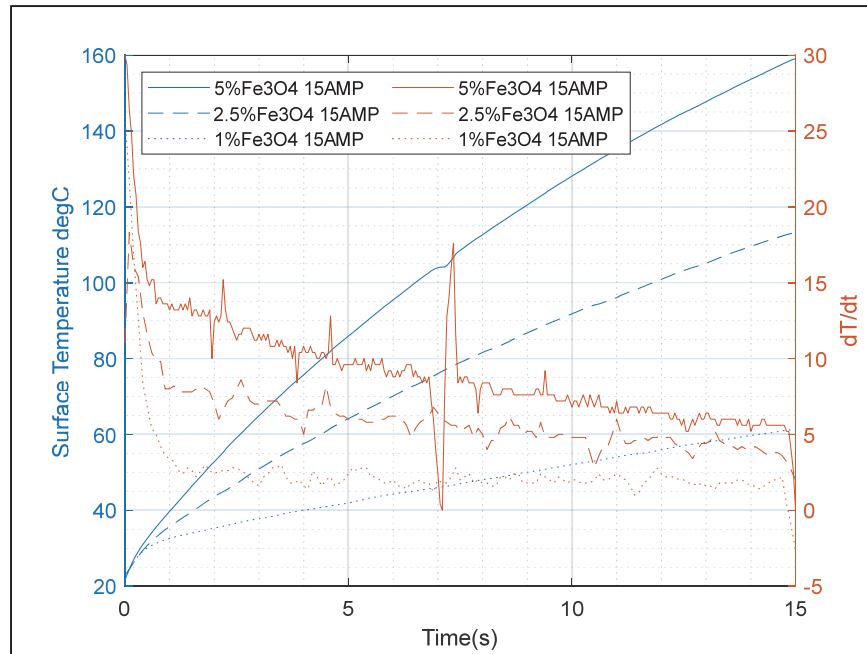


Figure 4.11: Surface Temperature and Heating Rate vs Time for 15A/15s Hysteresis Fuel Samples

During testing the 5wt% magnetite hysteresis fuel samples exhibited off-gassing while slightly elongating axially and bulging radially for both UltraFlex heater settings (15A and 6A). After the experiment was completed, the sample section contained within the coil had a spongy mechanical response when compressed. It is proposed that disassociation of the urethane bonds occurs, and the off-gassing consists of isocyanate vapors [62]. A previous investigation into the thermal decomposition of 2,4-toluene diisocyanate (TDI) cross-linked HTPB-based urethanes exhibited isocyanate dissociation in air starting at 208°C [62-63]. While not IPDI, the structure of the TDI is similar to IPDI, thus, it is reasonable to assume the IPDI was off-gassing [62].

Figure 4.12 shows the surface temperature measurements of all samples. It is observed that for both heater settings, relevant temperatures for leveraging temperature sensitivities can be reached. However, the 15A heater setting achieves these temperatures on a better timescale than the 6A setting. It is also seen that the heating rate reduces over time for all samples (indicated by the slopes of each line on Figure 4.12). To better understand the heating rate and characterize magnetic hysteresis heating power, the experimental data from the 15A/15s tests were used to calculate an estimated heating power, assuming no losses (Table 4.2). The calculation used Equation 4.1, where m is the sample mass, c_p is specific heat (2000 J/kg·K [57]), T_s is the final surface temperature (Table 4.3), T_i is initial temperature (22°C), and Δt is time (15s).

$$P = \frac{mc_p(T_s - T_i)}{\Delta t} \text{ [W]} \quad \text{Equation 4.1}$$

The experimental results were compared to values derived from literature. Specific absorption rate (SAR) data for multiple magnetite (Fe_3O_4) particle sizes tested at various magnetic field strengths from Mohapatra [42] were used to extrapolate a SAR value for 30nm magnetite particles in a 12Oe (955A/m) field in W/g. The extrapolated SAR value was multiplied by the fuel sample mass to estimate heating power. This extrapolation does not provide a direct comparison to the experimental data because the induction heater frequency used by Mohapatra[42] is different from the UltraFlex heater, but it provides an order of magnitude validation (Table 4.2).

A COMSOL Multiphysics 6.0 heat transfer model of a fuel sample grain was developed to validate the experimental heating power calculation. The model setup was outlined in Section 3.3.3. To summarize, the model assumes a constant volumetric internal heating rate as the source of heat generation. The boundaries are set up to account for losses due to natural convection and radiation. The constant internal power generation (heating rate) value was iterated on until the model matched the experimental surface temperature values for each sample. The results, assuming constant internal heating rate, for each weight percentage are in Table 4.2. It is important to note that the COMSOL model's assumption of constant

heating rate does not match reality because magnetic hysteresis heating power is dependent on temperature; the heating rate will decrease as temperature increases.

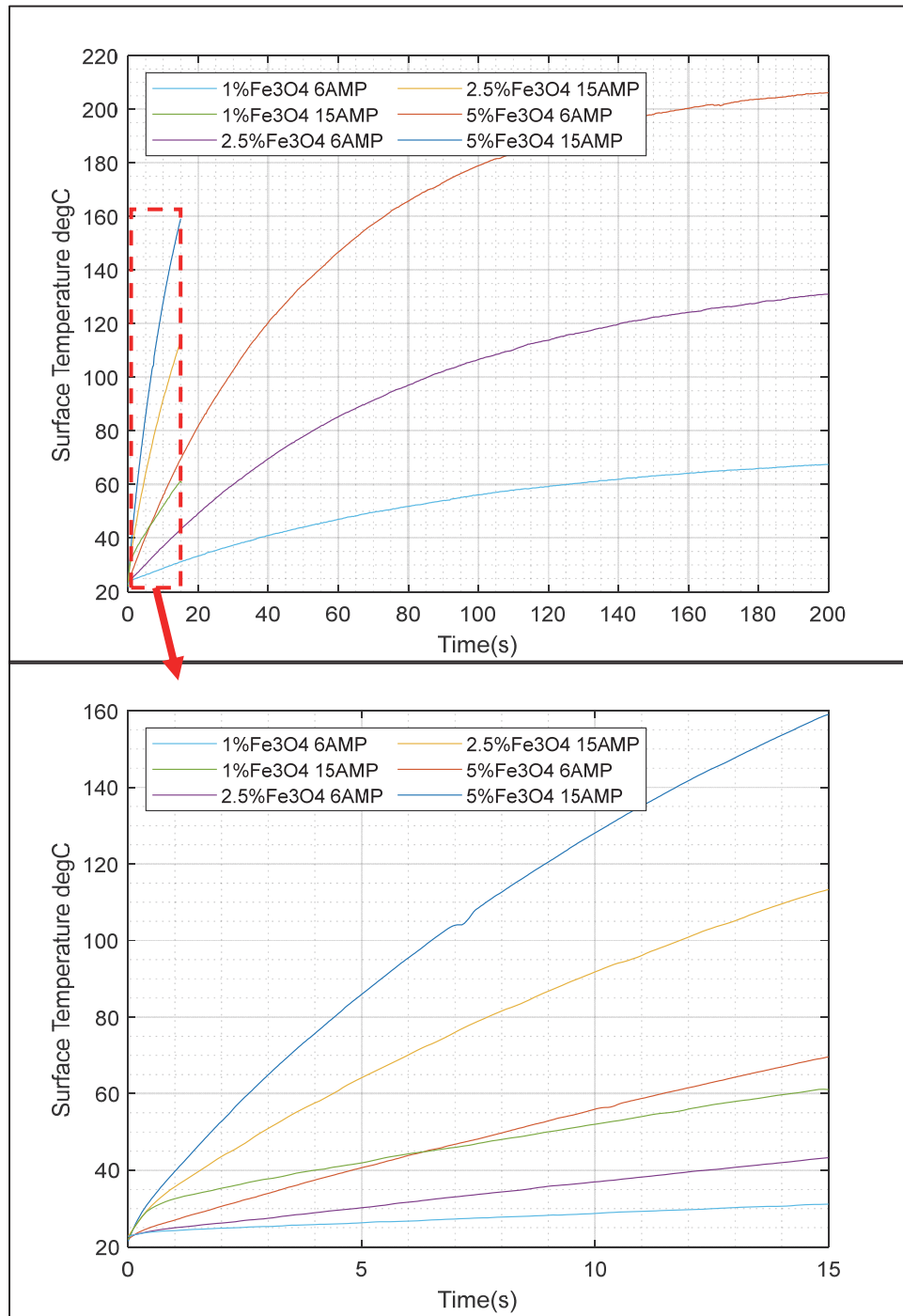


Figure 4.12: Magnetic hysteresis heating of HTPB fuel samples in UltraFlex Induction Heater.

A DC superconducting quantum interference device (SQUID) magnetometer [64] was used to find hysteresis curves at various magnetic field strengths for the 30nm magnetite powder to further characterize

hysteresis heating power (Figure 4.13). This device completes one magnetic field loop in a very slow manner. For the SQUID used by this study, each loop takes about an hour to complete. Equation 2.4 [21] from Section 2.3 is used to estimate the volumetric heating power (W/m^3) given a hysteresis loop. By multiplying the volumetric heating power by the sample volume, the heating power in W was estimated to be 0.94W (Table 4.2) for a 50Oe (3979A/m) field. The rest of the magnetometer data is in Appendix A.3. The SQUID could not generate the small field strength of the UltraFlex heater [12Oe (377A/m)], so this is not a direct comparison, rather order of magnitude. However, this value seemed significantly lower than the literature, experimental, and analytical heating power values.

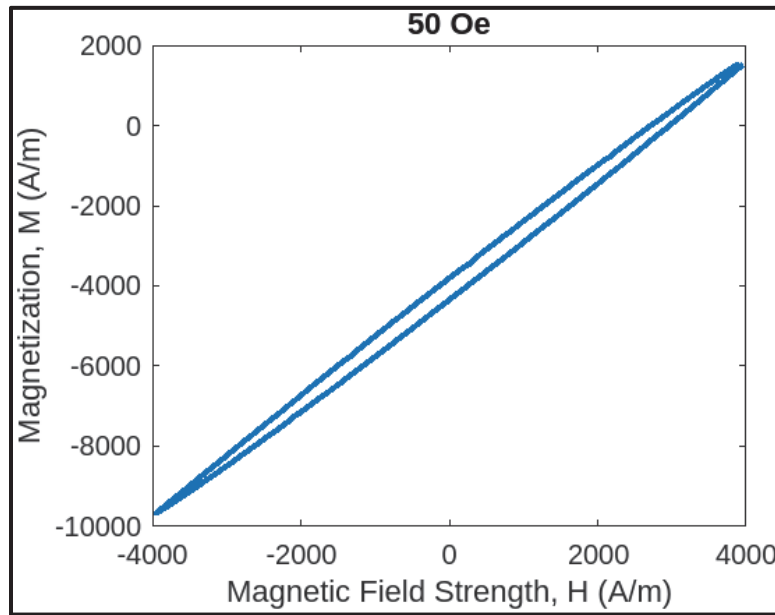


Figure 4.13: Magnetic hysteresis of 30nm magnetite in 50Oe field, taken with a DC SQUID magnetometer.

Table 4.4: Heating Power Comparison

Method	1wt% Fe_3O_4	2.5wt% Fe_3O_4	5wt% Fe_3O_4	Notes
$W = \frac{c_p m \Delta T}{t}$ [W] (Experimental)	1.59	3.66	5.70	Assuming no heat loss
COMSOL [W] (Analytical)	1.63	3.83	5.78	Constant \dot{q}_{gen} , $h = \frac{5W}{m^2 K}$
$SAR = \frac{c_p}{m} \left(\frac{dT}{dt} \right)$ [W] (Literature)	0.614	1.54	3.22	Extrapolated from Mohapatra [42] $\frac{f_{UF\ IH}}{f_{Lit\ IH}} = 1.97$
SQUID Magnetometer (Experimental)	0.94W in 50Oe Field			Exp. H field = 12Oe

It is concluded that Néel relaxation plays a role in the nonlinearity of the experimental heating rate and is the reason for the outlying SQUID magnetometer heating power calculation. If a particle's Néel relaxation time is less than the frequency of the induction heater's magnetic field, it will behave like it is in the superparamagnetic regime resulting in significantly reduced heat generation [42-44], [65-68]. Néel relaxation time is dependent on a few factors: anisotropic energy constant, hydraulic volume, and temperature [42-44], [65-68]. It is estimated with Equation 4.2, where τ_o is the attempt frequency, K_{eff} is the anisotropy constant, V is hydraulic volume, T is temperature, and k_B is the Boltzmann constant [42-], [65-68]. The attempt frequency, τ_o , represents how often the particle attempts to overcome its anisotropic energy barrier. For non-interacting particles, this value ranges from 10^{-13} to 10^{-9} , but for interacting particles, this value can reach 10^5 [69]. It is dependent on the particle's anisotropy [43-44], [69-70]. The product of $k_B T$ represents the thermal energy. When this value is sufficient, Néel relaxation is enabled.

$$\tau_N = \tau_o * \exp\left(\frac{K_{eff}V}{k_B T}\right) [s] \quad \text{Equation 4.2}$$

The anisotropic energy of the particle is represented by $K_{eff}V$ where K_{eff} is dependent on particle size and synthesis method [43-44], [69-70]. The value of K_{eff} becomes more significant at smaller particle sizes because there is a higher surface area to volume ratio [43-44], [69-70]. Multiple studies have characterized the K_{eff} value for magnetite based on particle size (Figure 4.14) [43-44], [71-72]. While all the papers agree on a K_{eff} value for bulk magnetite, they differ greatly as particle size is reduced. This is because K_{eff} is dependent on the surface structure which is related to synthesis method.

Néel relaxation times were calculated for various particle sizes and temperatures to gain an idea of how large of a role this plays in the experiment. For attempt frequency, a value of 10^{-9} was used because it is assumed the MNPs are well dispersed inside the fuel sample and not interacting with each other. However, agglomerations of MNPs could push the attempt frequency closer to 10^{-13} . The K_{eff} values from Mohapatra et al. [43] and Demotière et al. [44] were used to observe the upper and lower bounds of the Néel relaxation time for each particle size. Figures 4.15 and 4.16 display the results, along with the marked time for the UltraFlex Heater's frequency and the time it takes the SQUID magnetometer to complete one cycle. It is observed that the SQUID magnetometer data are heavily affected because all particles less than 30nm for both K_{eff} values have a Néel relaxation time less than the frequency of the magnetometer. This means that the hysteresis contributions of these particles are not captured in the loop generated by the SQUID magnetometer. An AC magnetometer with a frequency closer to that of the UltraFlex heater would provide a more accurate hysteresis loop for the experimental conditions.

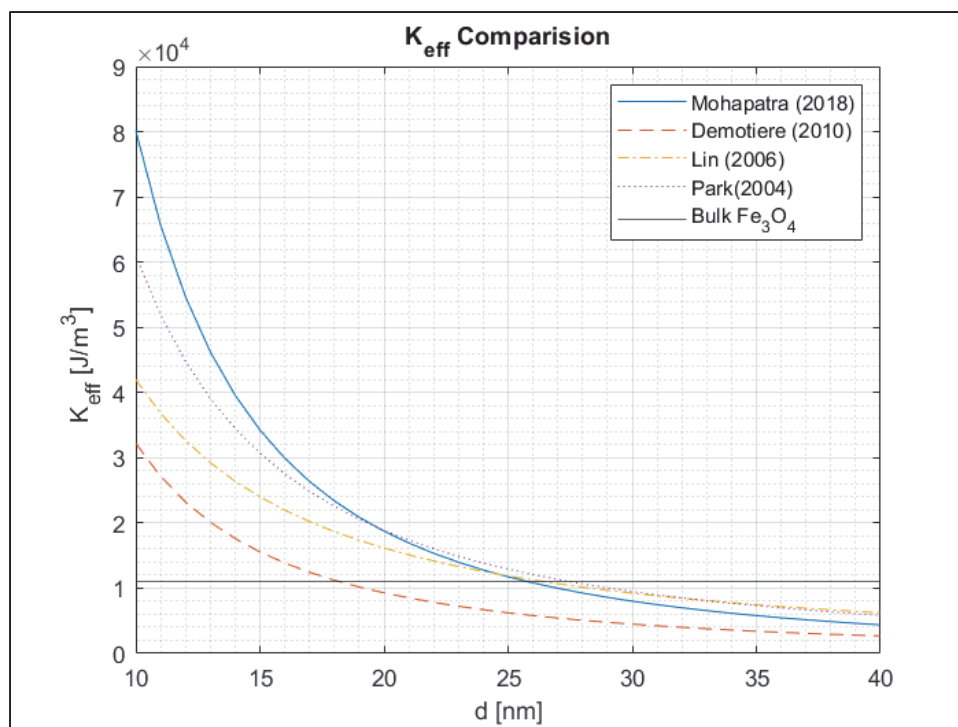


Figure 4.14: Anisotropic constant values derived from literature for magnetite nanoparticles [43-44], [71-72].

It is also observed that, depending on K_{eff} , some particles have Néel relaxation times on the order of the UltraFlex heater's frequency. Recall from Section 3.1.1, TEM imaging revealed a significant portion of magnetite particles are around 15nm in diameter. While an exact particle size distribution is unknown at this point, this information can be used to validate presence of particles sized small enough to impact hysteresis heating power when using the UltraFlex heater. It is concluded that the observed non-constant heating rate is caused by an increase in number of particles with a Néel relaxation time less than the heater's frequency as the temperature of the sample is increased.

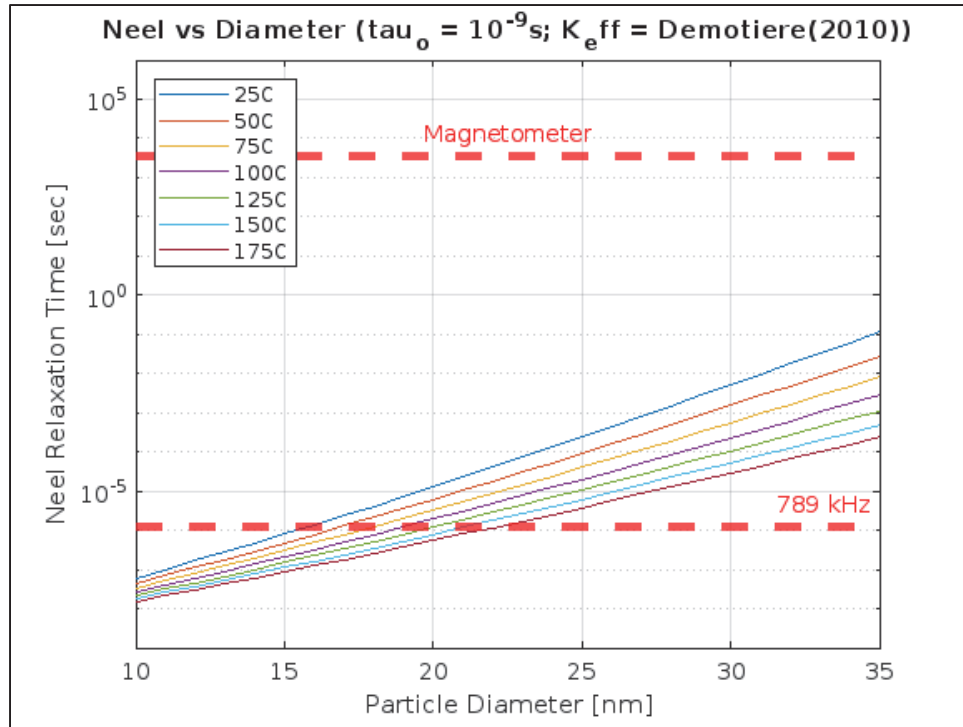


Figure 4.15: Néel relaxation times for various particle sizes and temperatures using the anisotropic energy constant from Demotière.

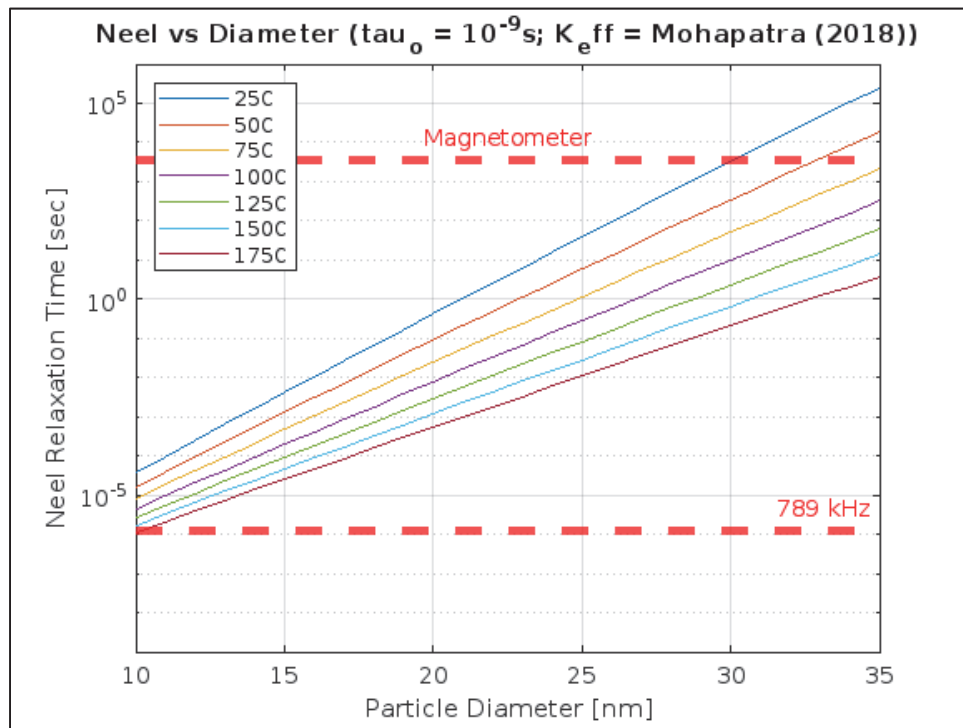


Figure 4.16: Néel relaxation times for various particle sizes and temperatures using the anisotropic energy constant from Mohapatra.

4.3.2 Wired Fuel Eddy Current Heating Tests

Eddy current heating (Joule effect) of fuel samples was performed with aluminum and copper wires to characterize the heating potential. IR measurements provide only surface temperature; thus, given the configuration of the wire, the actual maximum temperature is expected to be significantly greater. Measurements of similar diameter copper and aluminum wires demonstrate that the aluminum wires have far superior heating capabilities compared to copper. Aluminum wires of 0.64mm and 0.32mm diameters produced enough heat to reach a surface temperature of 126°C from an initial temperature of 22°C in 15s. Copper wires of 0.64mm and 0.40mm diameter resulted in only an 8°C increase in the same 15s time frame. It should be noted that despite the minimal increase in surface temperature, the copper wire could still produce significant enough heat to decompose HTPB (Figure 4.17). These heating results are promising because it shows significant temperature increases can be achieved in a short period of time which could be used to quickly enhance regression rate of a fuel.

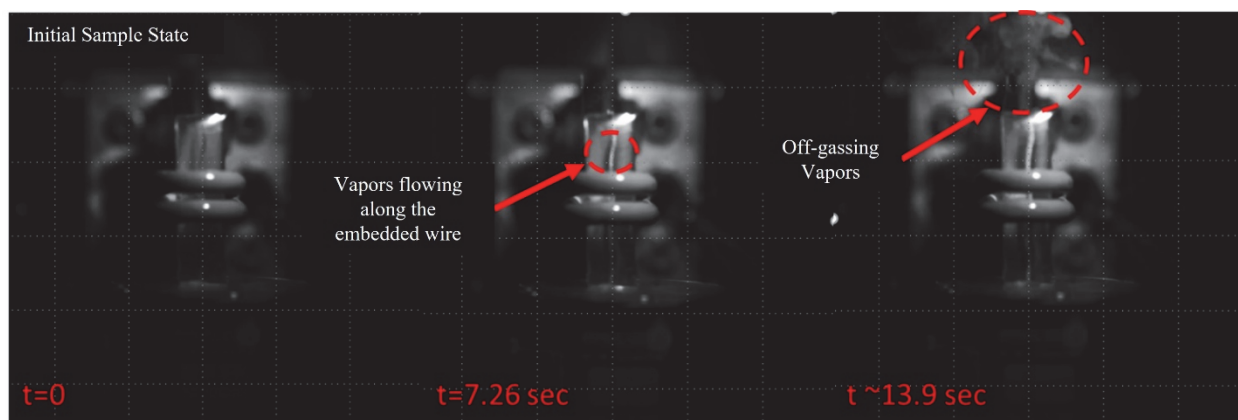


Figure 4.17: Thermal decomposition of HTPB fuel strand via heating from induction heated 0.64mm copper wire. Encircled in the center figure is the development of a gas interface along the solid wire due to decomposition. Encircled on the right is the escaping jet of HTPB decomposition products.

4.3.3 MNP Propellant Hysteresis Heating Tests

Initial attempts to characterize the surface temperature of the propellant samples during heating were unsuccessful due to the unexpectedly rapid energetic response of the propellant sample. The 5wt% magnetite sample ignited 1.5 seconds after completing the 15A/15s IH cycle (Figure 4.18). This result, while unexpected, was promising because it demonstrated the capability of IH to provide ample thermal energy to initiate propellant ignition. The 1wt% and 2.5wt% magnetite propellant samples did not exhibit ignition after completing the same 15A/15s IH cycle as the 5wt% samples. The 5wt% magnetite sample results required further development in the experimental setup to preserve the coil. For burning rate testing discussed in Section 4.4, propellant samples are inserted into a borosilicate glass tube to provide a barrier between the induction coil and the combusting propellant.

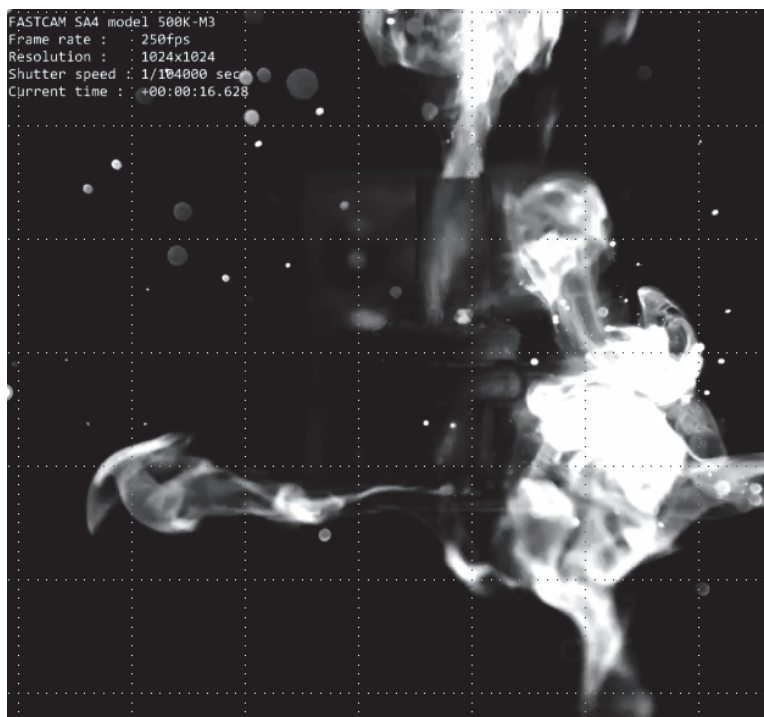


Figure 4.18: Combustion of 5wt% magnetite hysteresis based heated propellant. Note: The flame structure is of the burning PMMA barrier sheet that was around the propellant sample.

Attempts were made to characterize the heating of the 2.5wt% propellant samples. To perform these experiments, the samples were cut down to 12mm in length and held at the center of the coil by a 3D printed PLA holder. A few samples were tested inside of a borosilicate tube without the IR camera to ensure ignition would not occur resulting in damaged equipment. After this check, the IR camera was set up to view the top surface (square end) of the sample and a maximum temperature of 208°C was observed (initial sample temperature was about 22°C). There was also the presence of off-gassing - similar to that seen with the solid fuel samples - which is believed to be caused by the disassociation of the urethane bonds and consists of isocyanate vapors (as discussed in Section 4.3.1). The IR camera was then moved to view the side of the sample at the center of the coil and a maximum temperature of 218°C was observed (initial sample temperature was about 22°C). The higher maximum temperature makes sense because the magnetic field is most uniform at the center of the coil, so the highest heating will occur at that location. It is also noted that the samples appeared to bulge and elongate axially. It is proposed that this is a result of the off-gassing and is creating porosity within the sample (Figure 4.19). The impact of the porosity on burning rate is further discussed in Section 4.4.

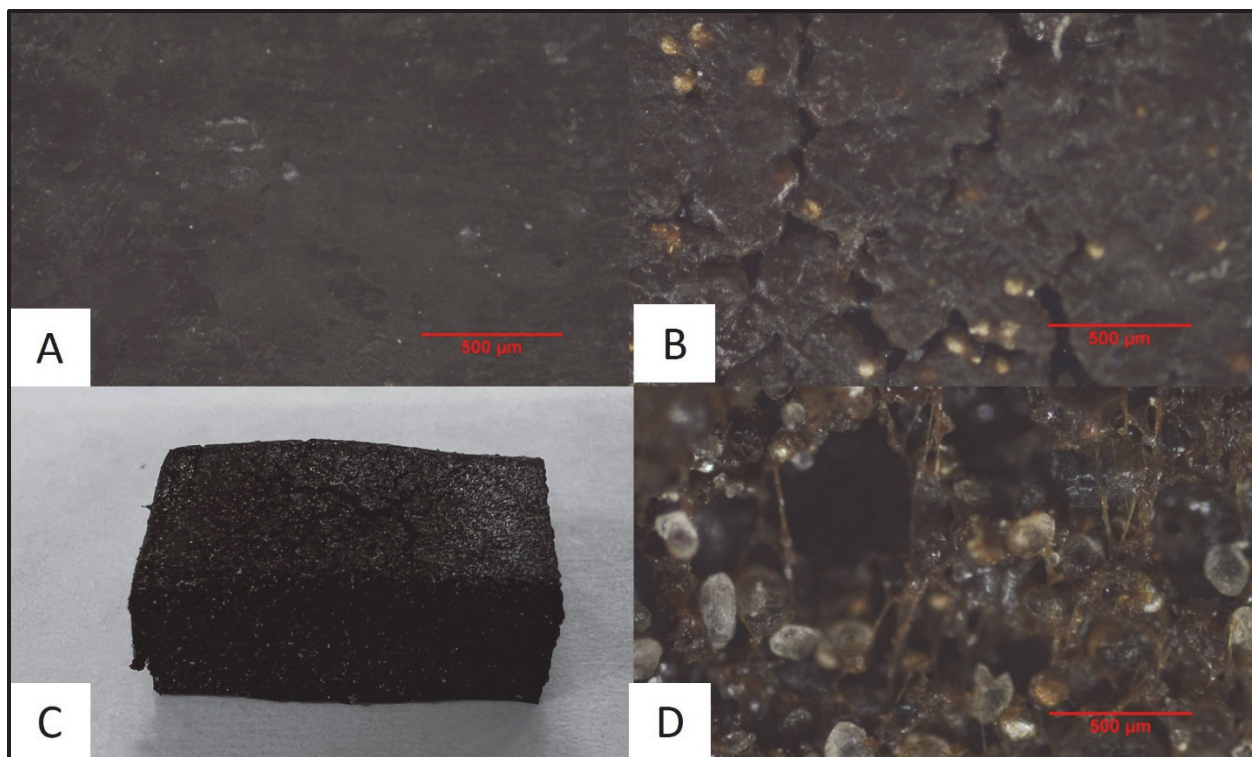


Figure 4.19: A) Surface of non-heated propellant sample. B) Surface of heated propellant sample. C) Heated propellant sample shows bulging in the center. D) Porosity inside heated propellant sample, shows that the AP and Al appear to be unaffected which supports the assumption that the urethane bonds in the binder are breaking down and isocyanate vapors are produced.

4.3.4 Wired Propellant Eddy Current Heating Tests

Eddy current heating (Joule effect) of propellant samples via embedded wires was performed only with 0.64mm diameter aluminum wires. During fuel sample testing, aluminum produced significantly more heating than copper wires, which was expected based on conductivity and density. As with the 5wt% magnetite hysteresis propellant samples, IR measurements could not be performed due to ignition of the propellant samples. High-speed imaging data shows that the wired propellant appears to ignite from the propellant's center at the location inside the induction coil (Figure 4.20). Ignition of the wired propellant occurred at approximately seven seconds of heating. DSC measurements (taken by MCL) of AP particles with iron oxide nanoparticles acting as a catalyst showed a high temperature decomposition of 340°C (See Appendix B). It is expected that the wired propellant samples reached at least this temperature, most likely higher because this formulation does not have an iron oxide catalyst.



Figure 4.20: Ignition of 0.64mm aluminum wired propellant along the wire/propellant interface.

4.4 MNP Propellant Burning Rate Testing

As discussed in Section 3.2.2 a Photron FASTCAM SA4 was used to optically measure burning rate. While only a few points above and below the coil could be obtained, it gives a decent measurement of relative changes in burning rate between the heated and non-heated sections of the propellant grain. To prevent premature ignition of the heated section of the propellant grain, as observed in the 5wt% magnetite (Fe_3O_4) samples during propellant heating tests, the 2.5wt% magnetite propellant samples were used for the burning rate testing. The non-heated section of all three samples of the 2.5wt% magnetite propellant exhibited an average burning rate of $0.94 \pm 0.01\text{mm/s}$ at atmospheric pressure and an ambient temperature around 22°C . The inductively heated section of the three propellant samples exhibited an average burning rate of $2.18 \pm 0.19\text{mm/s}$ (Figure 4.21). While the standard deviation of the heated propellant burning rate is greater, the inductively heated burning rate is 131% faster than the nominal (average value of three samples). This result shows that induction heating can modulate the burning rate of solid propellant after ignition. The next step is understanding the cause of this burning rate enhancement.

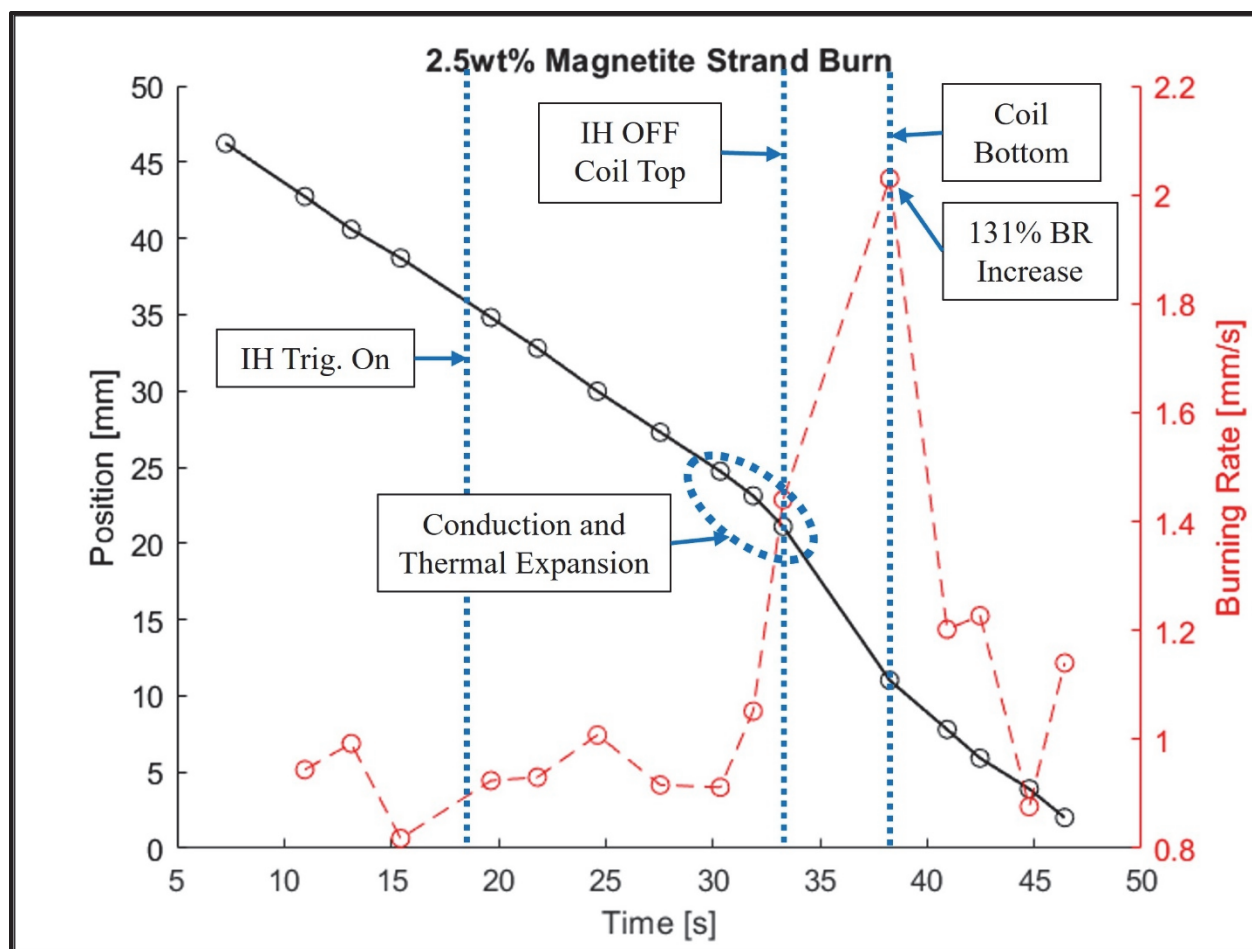


Figure 4.21: Results of dynamic burning rate testing of 2.5wt% magnetite propellant samples (average of three samples).

The original motivation of this study was to leverage the temperature sensitivity of solid propellants to modulate burning rate, however, the observed increase is thought to be more than a purely thermal effect. Instead, it is a consequence of temperature sensitivity coupled with changes in sample density and burning surface area due to generated porosity. Recall from Section 4.3.3, when the propellant samples are heated, there is off-gassing that creates porosity inside the sample as well as bulging and axial elongation. This porosity greatly increases the burning surface area in the heated section of the propellant sample resulting in a burning rate increase. This theory is further supported by a comparison to temperature sensitivities from literature for APCPs with embedded iron oxide particles (Table 4.5). A temperature sensitivity of around 0.2 %/°C is typical for most APCPs with iron oxide catalysts. If this value is assumed, a change in temperature of 655°C is needed to achieve a 131% burning rate increase. From the hysteresis propellant heating tests (Section 4.3.3), it is known that the sample on reaches 218°C (around a 196°C change in temperature) after a 15A/15s heating cycle. This comparison confirms that there is more going on than

simply a thermal effect. It is concluded that a combination of temperature sensitivity effect and burning surface area changes due to porosity is the source of the burning rate enhancement.

Table 4.5: Temperature Sensitivity Values from Literature of AP Composite Propellants with Catalysts

Composition	$\sigma_P \left[\frac{\%}{^\circ\text{C}} \right]$	Pressure	Ref
AP PBAN 2.4% Fe_2O_3	0.20	Extrapolated to 14.7psi	[73]
AP Al HTPB 2% Fe_2O_3	0.18	1380 psi	[74]

Chapter 5

CONCLUSION AND FUTURE WORK

5.1 Conclusion

This study explored the use of induction heating (IH) as a mechanism for modulating the burning rate of solid fuels and propellants. This was done by investigating four sample types: wired fuel, wired propellant, fuel with embedded MNPs, and propellant with embedded MNPs. The wired samples were developed to investigate the IH mechanism of eddy current heating (Joule effect) while the samples with embedded MNPs are used for exploring the mechanism of magnetic hysteresis heating. Experimental results were gathered to characterize heating capability of each sample type. An analytical model was developed to validate the experimental heating results of the fuel samples with embedded MNPs. Finally, experimental results were gathered for burning rate testing of the propellant samples with embedded MNPs.

Wired fuel samples were HTPB with embedded aluminum and copper wires of various diameters. They were heated using the UltraFlex induction heater for 15s on the 15A setting and it was found that the 0.64mm diameter aluminum wires provided the highest relative heating. The surface temperature of the fuel increased by 124°C. This is a promising result because temperatures high enough to leverage the temperature sensitivity of fuels was achieved on a time scale relevant to dynamically modulating burning rate. During testing of the wired propellant samples ignition occurred, so these samples could not be explored further with the current experimental setup. However, this result is also promising as it shows significant thermal energy was transferred to the propellant in a few seconds. This behavior could be optimized to achieve different results.

For the samples with embedded MNPs, zinc ferrite, cobalt ferrite, magnetite, and maghemite were characterized to select the best relative susceptor. It was found that the 30nm magnetite had the highest relative heating potential and was used as the susceptor for the fuel and propellant samples. Three weight percentages of magnetite particles were used: 1wt%, 2.5wt%, 5wt%. The 5wt% attained the highest heating, reaching a surface temperature of 159°C (from an initial temperature of 22°C) when heated for 15s in the UltraFlex heater on the 15A setting. Under the same conditions, the 2.5wt% sample reached a surface temperature of 113°C. These results are promising because relevant temperatures for enhancing burning rate were achieved in a short period of time using small amounts of embedded MNPs.

The 5wt% propellant sample ignited during heating tests, so it could not be pursued further in the current testing configuration. However, this result shows significant heat generation can be achieved through the IH mechanism of magnetic hysteresis. The 2.5wt% propellant sample heating tests resulted in a surface temperature of 218°C (from initial temperature of 22°C). Off-gassing, bulging, and sample

elongation was also observed during the 2.5wt% propellant sample heating tests. It was concluded that the urethane bonds are disassociating which generates isocyanate gases resulting in a density change within the sample by introducing porosity. This result shows that one way the magnetic hysteresis heating power can be tailored to achieve different temperatures and behaviors is based on the weight percentage of embedded particles. This is advantageous for solid propellants because typically, only small amounts of additives are desired.

To characterize the experimental heating power, a calculation was made, assuming no heat loss, using the data from testing of the fuel samples with embedded MNPs. These experimental values match closely with the analytical estimated heating power from the COMSOL Multiphysics 6.0 simulations. However, COMSOL assumes a constant heating power which generates a linear temperature versus time curve while the experimental data appeared to have a logarithmic shape. It was concluded that the reduction of heating power as the sample temperature increases is a consequence of Néel relaxation. An approximate particle size analysis showed that the 30nm magnetite has a significant fraction of particles on the order of 15nm which have Néel relaxation times that drop below the frequency of the UltraFlex heater as the sample temperature rises resulting in reduced magnetic hysteresis heating efficiency. This observation shows that another means of optimizing sample heating power is particle size selection. The decreasing heating power could also be leveraged to prevent thermal runaway of solid propellant samples.

While the heating test results discussed above imply IH can be used to modulate burning rate by leveraging the temperature sensitivity of propellants, to prove this method works, burning rate testing is completed for the propellant samples with embedded magnetite particles. The 2.5wt% propellant samples exhibited an average increase in burning rate of 131% in the heated section of the sample. This result proves significant burning rate enhancement can be achieved after ignition. It is proposed that this increase is a result of both a temperature sensitivity effect and the increased burning surface area due to the porosity generated by IH.

5.2 Future Work

This study began the investigation into the use of IH as a mechanism for modulating the burning rate of solid fuels and propellants. More work is needed to continue this study. Future efforts to do so are as follows:

- The temperature sensitivity of the propellant formulations used in this study will need to be characterized in an optical strand burner. Current efforts are being made to develop this experimental setup.

- An opposed flow burner experimental setup is currently being developed to perform regression rate tests on the fuel samples with embedded MNPs.
- An experimental setup needs to be designed for the safer testing of wired fuel and propellant samples because the wired fuel samples underwent off-gassing during heating tests and the wired propellant samples ignited.
- Ongoing efforts are working on further development of a COMSOL Multiphysics model to more accurately simulate the effects of IH on each sample type.
- Fully characterizing the particle size distribution of the MNPs will allow for a better idea of the full impact of Néel relaxation on heating power. If the particle size distribution is known, the heating power of particles affected by Néel relaxation can be calculated which will allow for a more accurate estimate of total heating power.
- Acquiring fiber optic thermocouples to experimentally measure internal temperature of the fuel and propellant sample is of interest to characterize the internal heating profile. This will become especially important of larger sample sizes.
- Acquiring thinner fiber optic wires to develop a better method for measuring the burning rate of a sample inside the coil is also desired. Appendix E discusses the novel burning rate measurement method in detail.
- Characterization of the heating capability of different particle sizes and materials would be of interest to allow for optimization of systems in the future. If this is to be applied to a real system, it will be important to understand which materials and particle sizes are required to achieve the desired effects for a given coil design, magnetic field strength, and frequency.

REFERENCES

- [1] P. Caubet and M. Berdoyes, “Innovative ArianeGroup Controllable Solid Propulsion Technologies,” in *AIAA Propulsion and Energy 2019 Forum*, Reston, Virginia: American Institute of Aeronautics and Astronautics, Aug. 2019. doi: 10.2514/6.2019-3878.
- [2] M. Zhu, Y. K. Li, X. Chen, J. J. Mi, W. X. Li, and H. F. Xue, “Design of nonlinear control method for pressure of pintle solid rocket motor,” *Acta Astronaut*, vol. 215, pp. 296–307, Feb. 2024, doi: 10.1016/j.actaastro.2023.12.008.
- [3] C. Shuling and L. I. Fengsheng, “Influence of Long Metal Wires on Combustion of Double-Base Propellants,” 1982.
- [4] S. Isert, C. D. Lane, I. E. Gunduz, and S. F. Son, “Tailoring burning rates using reactive wires in composite solid rocket propellants,” *Proceedings of the Combustion Institute*, vol. 36, no. 2, pp. 2283–2290, 2017, doi: 10.1016/j.proci.2016.06.141.
- [5] S. J. Barkley, K. Zhu, J. E. Lynch, J. B. Michael, and T. R. Sippel, “Microwave plasma enhancement of multiphase flames: On-demand control of solid propellant burning rate,” *Combust Flame*, vol. 199, pp. 14–23, Jan. 2019, doi: 10.1016/j.combustflame.2018.10.007.
- [6] T. Sippel, J. Michael, S. Barkley, K. Zhu, and J. Lynch, “Microwave Enhancement of Composite Solid Propellant Flames Final Technical Report DISTRIBUTION A: Distribution approved for public release Air Force Materiel Command,” Ames, Mar. 2021. [Online]. Available: <https://apps.dtic.mil/sti/pdfs/AD1132528.pdf>
- [7] S. J. Barkley, K. Zhu, J. B. Michael, and T. R. Sippel, “Pulsed microwave enhancement of doped composite solid propellants,” in *AIAA SciTech Forum - 55th AIAA Aerospace Sciences Meeting*, American Institute of Aeronautics and Astronautics Inc., 2017. doi: 10.2514/6.2017-0832.
- [8] S. J. Barkley, D. K. Kindem, K. Zhu, J. B. Michael, and T. Sippel, “Dynamic control of composite solid propellant flame spread through microwave eddy current heating of propellant-embedded antennas,” in *AIAA Scitech 2019 Forum*, American Institute of Aeronautics and Astronautics Inc, AIAA, 2019. doi: 10.2514/6.2019-1239.
- [9] J. Lynch, M. Ballesteros, S. Barkley, R. Cazin, J. B. Michael, and T. R. Sippel, “Microwave-supported plasma combustion enhancement of composite solid propellants using alkali metal dopants,” in *54th AIAA Aerospace Sciences Meeting*, American Institute of Aeronautics and Astronautics Inc, AIAA, 2016. doi: 10.2514/6.2016-0685.
- [10] G. Young, J. J. Koeck, N. T. Conlin, J. L. Sell, and G. A. Risha, “Influence of an electric field on the burning behavior of solid fuels and propellants,” *Propellants, Explosives, Pyrotechnics*, vol. 37, no. 1, pp. 122–130, Feb. 2012, doi: 10.1002/prop.201100052.
- [11] S. A. Abrukov *et al.*, “Effects of an electric field on combustion in condensed systems,” *Combust Explos Shock Waves*, vol. 11, no. 1, pp. 110–111, Jan. 1975, doi: 10.1007/BF00742867/METRICS.
- [12] A. A. Baranov, V. F. Buldakov, and G. G. Shelukhin, “Influence of the Electric Field on the Combustion Rate of a Heterogenous Condensed System,” *Combust Explos Shock Waves*, vol. 12, no. 5, pp. 689–692, 1976.

- [13] C. R. F. Bestgen, "A Study of the Effects of Electric Fields on Solid Propellant Burning Rates," Doctoral Dissertation, Air Force Institute of Technology, Wright-Patterson AFB, Ohio, 1970. [Online]. Available: <https://apps.dtic.mil/sti/pdfs/AD0731840.pdf>
- [14] C. R. F. Bestgen and H. E. Wright, "A Study of the Effects of Electric Fields on Solid Propellant Burning Rates," *AIAA 9th Aerospace Sciences Meeting*, Jan. 1971, doi: 10.2514/6.1971-174.
- [15] P. J. Mayo, L. A. Watermeier, and F. J. Weinberg, "Electrical control of solid propellant burning," *Proc R Soc Lond A Math Phys Sci*, vol. 284, no. 1399, pp. 488–498, Mar. 1965, doi: 10.1098/RSPA.1965.0076.
- [16] I. Zamir, M. Ben-Reuven, A. Gany, and D. Grinstein, "Investigation of Electrically Controlled Ammonium Nitrate – Epoxy Solid Propellant at High Pressures," *Propellants, Explosives, Pyrotechnics*, vol. 46, no. 3, pp. 477–483, Mar. 2021, doi: 10.1002/PREP.202000208.
- [17] X. Liu *et al.*, "Comprehensive understanding of magnetic hyperthermia for improving antitumor therapeutic efficacy," *Theranostics*, vol. 10, no. 8, pp. 3793–3815, 2020, doi: 10.7150/thno.40805.
- [18] C. A. M. Iglesias *et al.*, "Magnetic nanoparticles hyperthermia in a non-adiabatic and radiating process," *Sci Rep*, vol. 11, no. 1, Jun. 2021, doi: 10.1038/s41598-021-91334-9.
- [19] B. Mehdaoui *et al.*, "Optimal size of nanoparticles for magnetic hyperthermia: A combined theoretical and experimental study," *Adv Funct Mater*, vol. 21, no. 23, pp. 4573–4581, Dec. 2011, doi: 10.1002/adfm.201101243.
- [20] S. Zinn and S. Semiatin, *Elements of Induction Heating*. Carnes Publication Services Inc., 1988.
- [21] B. D. Cullity and C. D. Graham, *Introduction To Magnetic Materials*, 2nd ed. Hoboken: John Wiley & Sons Inc, 2008. doi: 10.1002/9780470386323.
- [22] H. Osborn, P. Brace, W. Johnson, J. Cable, and T. Eagan, *Induction Heating*. Cleveland: Twenty Seventh National Metal Congress and Exposition, 1946.
- [23] E. Davies and P. Simpson, *Induction Heating Handbook*. London: McGRAW-HILL Book Company (UK) Limited, 1979.
- [24] D. J. Ramirez, K. A. Walz, M. Zhao, J. E. Boyer, Q. Wang, and R. Yetter, "Active burning rate control of solid propellant via RF frequency hysteresis heating of magnetic nanoparticles," in *Eastern State Section of the Combustion Institute Spring Meeting*, Athens, Mar. 2024.
- [25] D. J. Ramirez, K. A. Walz, M. Zhao, J. E. Boyer, Q. Wang, and R. Yetter, "Active burning rate control of solid propellant via RF frequency hysteresis heating of magnetic nanoparticles (working title)," 2024.
- [26] G. Sutton and O. Biblarz, *Rocket Propulsion Elements*, Ninth. Hoboken: John Wiley & Sons Inc., 2017.
- [27] Northrop Grumman, "Northrop Grumman Performs Full-Scale Propellant Mix for Next-Generation Interceptor Motor," Northrop Grumman. Accessed: Jan. 10, 2024. [Online]. Available: <https://news.northropgrumman.com/news/releases/northrop-grumman-performs-full-scale-propellant-mix-for-next-generation-interceptor-motor>
- [28] T. McCreary, *Experimental Composite Propellant*. Murray State University, 2000.

- [29] N. Kubota, *Propellants and Explosives: Thermochemical Aspects of Combustion*. John Wiley & Sons, 2006. doi: 10.1002/9783527610105.
- [30] S. Isert, L. J. Groven, R. P. Lucht, and S. F. Son, "The effect of encapsulated nanosized catalysts on the combustion of composite solid propellants," *Combust Flame*, vol. 162, no. 5, pp. 1821–1828, May 2015, doi: 10.1016/j.combustflame.2014.11.040.
- [31] S. Chaturvedi and P. N. Dave, "A review on the use of nanometals as catalysts for the thermal decomposition of ammonium perchlorate," *Journal of Saudi Chemical Society*, vol. 17, no. 2, pp. 135–149, Apr. 2013. doi: 10.1016/j.jscs.2011.05.009.
- [32] W. Wang and J. Yao, "Catalytic activity of magnetite with different shapes for the thermal decomposition of ammonium perchlorate," *Chem Lett*, vol. 43, no. 10, pp. 1554–1556, 2014, doi: 10.1246/cl.140602.
- [33] M. Zhang *et al.*, "Catalytic Activity of Ferrates (NiFe₂O₄, ZnFe₂O₄ and CoFe₂O₄) on the Thermal Decomposition of Ammonium Perchlorate," *Propellants, Explosives, Pyrotechnics*, vol. 45, no. 3, pp. 463–471, Mar. 2020, doi: 10.1002/prep.201900211.
- [34] J. Sapkota, Y. H. Xu, and H. J. Sun, "Numerical study on response characteristics of solid rocket pintle motor," *Journal of Aerospace Technology and Management*, vol. 11, 2019, doi: 10.5028/jatm.v11.1050.
- [35] S. L. Burroughs, "Status of army pintle technology for controllable thrust propulsion," in *37th Joint Propulsion Conference and Exhibit*, American Institute of Aeronautics and Astronautics Inc., 2001. doi: 10.2514/6.2001-3598.
- [36] L. Hurt, "The Study of the Mechanism of Enhanced Burning Rate of Solid Propellants," Huntsville, 1964. Accessed: Feb. 05, 2024. [Online]. Available: <https://apps.dtic.mil/sti/citations/AD0348263>
- [37] J. J. Ritter, Z. Wingard, T. Canami, and A. McBain, "Visualization and Measurement of the Burning Surface of Wire-Embedded Energetic Materials, Part I: JA2 and Pentolite," 2014. [Online]. Available: <https://apps.dtic.mil/sti/citations/tr/ADA606477>
- [38] N. N. Bakhman and I. N. Lobanov, "Influence of the diameter of the heat-conducting elements on their efficiency during the combustion of condensed systems," *Combust Explos Shock Waves*, vol. 19, no. 1, pp. 42–46, Jan. 1983, doi: 10.1007/BF00790235.
- [39] M. Q. Brewster and B. E. Hardt, "Influence of metal agglomeration and heat feedback on composite propellant burning rate," *J Propuls Power*, vol. 7, no. 6, pp. 1076–1078, 1991, doi: 10.2514/3.23431.
- [40] R. J. Heinsohn, D. E. Wulforth, and P. M. Becker, "The effects of an electric field on an opposed-jet diffusion flame," *Combust Flame*, vol. 11, no. 4, pp. 288–296, Aug. 1967, doi: 10.1016/0010-2180(67)90018-1.
- [41] S. D. Marcum and B. N. Ganguly, "Electric-field-induced flame speed modification," *Combust Flame*, vol. 143, no. 1–2, pp. 27–36, Oct. 2005, doi: 10.1016/J.COMBUSTFLAME.2005.04.008.
- [42] J. Mohapatra, M. Xing, and J. P. Liu, "Inductive Thermal Effect of Ferrite Magnetic Nanoparticles," *Materials*, vol. 12, no. 19, p. 3208, Sep. 2019, doi: 10.3390/ma12193208.

- [43] J. Mohapatra *et al.*, “Size-dependent magnetic and inductive heating properties of Fe₃O₄ nanoparticles: Scaling laws across the superparamagnetic size,” *Physical Chemistry Chemical Physics*, vol. 20, no. 18, pp. 12879–12887, 2018, doi: 10.1039/c7cp08631h.
- [44] A. Demortière *et al.*, “Size-dependent properties of magnetic iron oxide nanocrystals,” *Nanoscale*, vol. 3, no. 1, pp. 225–232, Jan. 2011, doi: 10.1039/c0nr00521e.
- [45] C. Binns, “Tutorial section on nanomagnetism,” in *Frontiers of Nanoscience*, vol. 6, Elsevier Ltd, 2014, pp. 1–32. doi: 10.1016/B978-0-08-098353-0.00001-4.
- [46] COMSOL, “COMSOL Multiphysics Simulation Software.” Accessed: Jan. 09, 2024. [Online]. Available: <https://www.comsol.com/comsol-multiphysics>
- [47] Walter Frei, “Course: Modeling Electromagnetic Coils in COMSOL,” COMSOL. Accessed: Jan. 09, 2024. [Online]. Available: <https://www.comsol.com/blogs/course-modeling-electromagnetic-coils-in-comsol/>
- [48] US Research Nanomaterials Inc., “Iron Oxide Fe₂O₃ Nanopowder / Nanoparticles (Fe₂O₃, gamma, 99%, 20-40 nm).” Accessed: Feb. 05, 2024. [Online]. Available: <https://us-nano.com/inc/sdetail/593>
- [49] Nanostructured & Amorphous Materials Inc., “Cobalt Iron Oxides Nanopowder (CoFe₂O₄, 98%, 35-55 nm).” Accessed: Feb. 05, 2024. [Online]. Available: <https://www.nanoamor.com/inc/pdetail?v=1&pid=3968>
- [50] Nanostructured & Amorphous Materials Inc., “Zinc Iron Oxide Nanopowder (ZnFe₂O₄, 98.5%, 40 nm).” Accessed: Feb. 05, 2024. [Online]. Available: <https://www.nanoamor.com/inc/pdetail?v=1&pid=3967>
- [51] C. A. Schneider, W. S. Rasband, and K. W. Eliceiri, “NIH Image to ImageJ: 25 years of image analysis,” *Nature Methods*, vol. 9, no. 7, pp. 671–675, Jul. 2012. doi: 10.1038/nmeth.2089.
- [52] D. J. Ramirez, “Personal Communication.” Aug. 2023.
- [53] A. J. Claydon, “Resonant Acoustic Mixing of Polymer Bonded Explosives,” PhD, Cranfield University, 2020.
- [54] A. J. Claydon, A. N. Patil, S. Gaultier, G. Kister, and P. P. Gill, “Determination and optimisation of Resonant Acoustic Mixing (RAM) efficiency in Polymer Bonded eXplosive (PBX) processing,” *Chemical Engineering and Processing - Process Intensification*, vol. 173, p. 108806, Mar. 2022, doi: 10.1016/J.CEP.2022.108806.
- [55] “Surface Emissivity Coefficients.” Accessed: Mar. 17, 2024. [Online]. Available: https://www.engineeringtoolbox.com/emissivity-coefficients-d_447.html
- [56] Z. Zhang *et al.*, “Enhanced the thermal conductivity of hydroxyl-terminated polybutadiene (HTPB) composites by graphene-silver hybrid,” *Composites Communications*, vol. 24, p. 100661, Apr. 2021, doi: 10.1016/J.COCO.2021.100661.
- [57] D. M. Hanson-Parr and T. P. Parr, “Thermal properties measurements of solid rocket propellant oxidizers and binder materials as a function of temperature,” *Journal of Energetic Materials*, vol. 17, no. 1, pp. 1–48, 1999, doi: 10.1080/07370659908216094.

- [58] “The RCS Store.” Accessed: Mar. 17, 2024. [Online]. Available: <https://www.rocketmotorparts.com/>
- [59] P. Kosky, R. Balmer, W. Keat, and G. Wise, “Mechanical Engineering,” *Exploring Engineering*, pp. 259–281, Jan. 2013, doi: 10.1016/B978-0-12-415891-7.00012-1.
- [60] Y. Yang *et al.*, “Self-healing of electrical damage in polymers using superparamagnetic nanoparticles,” *Nature Nanotechnology*, vol. 14, no. 2. Nature Publishing Group, pp. 151–155, Feb. 01, 2019. doi: 10.1038/s41565-018-0327-4.
- [61] Y. Yang *et al.*, “Defect-targeted self-healing of multiscale damage in polymers,” *Nanoscale*, vol. 12, no. 6, pp. 3605–3613, Feb. 2020, doi: 10.1039/c9nr09438e.
- [62] D. J. Ramirez, “Personal Communication.” Jan. 2024.
- [63] T. Gupta and B. Adhikari, “Thermal degradation and stability of HTPB-based polyurethane and polyurethaneureas,” *Thermochim Acta*, vol. 402, no. 1–2, pp. 169–181, Jun. 2003, doi: 10.1016/s0040-6031(02)00571-3.
- [64] M. Zhiqiang, “Mao’s Quantum Materials Research Laboratory,” Penn State. [Online]. Available: <https://sites.psu.edu/zqmao/instruments/>
- [65] C. L. Dennis and R. Ivkov, “Physics of heat generation using magnetic nanoparticles for hyperthermia,” *International Journal of Hyperthermia*, vol. 29, no. 8, pp. 715–729, 2013, doi: 10.3109/02656736.2013.836758.
- [66] W. F. Brown, “Thermal fluctuations of a single-domain particle,” *Physical Review*, vol. 130, no. 5, pp. 1677–1686, Jun. 1963, doi: 10.1103/PhysRev.130.1677.
- [67] J. Carrey, B. Mehdaoui, and M. Respaud, “Simple models for dynamic hysteresis loop calculations of magnetic single-domain nanoparticles: Application to magnetic hyperthermia optimization,” *J Appl Phys*, vol. 109, no. 8, p. 83921, Feb. 2011, doi: 10.1063/1.3551582/929402.
- [68] R. E. Rosensweig, “Heating magnetic fluid with alternating magnetic field,” *J Magn Magn Mater*, vol. 252, no. 1–3, pp. 370–374, 2002.
- [69] R. Moreno, S. Jenkins, W. Williams, and R. F. L. Evans, “Atomistic calculation of the f 0 attempt frequency in Fe 3 O 4 magnetite nanoparticles,” Jan. 2024. doi: 10.48550.
- [70] Z. Ma, J. Mohapatra, K. Wei, J. P. Liu, and S. Sun, “Magnetic Nanoparticles: Synthesis, Anisotropy, and Applications,” *Chemical Reviews*, vol. 123, no. 7. American Chemical Society, pp. 3904–3943, Apr. 12, 2023. doi: 10.1021/acs.chemrev.1c00860.
- [71] J. Park *et al.*, “Ultra-large-scale syntheses of monodisperse nanocrystals,” *Nat Mater*, vol. 3, pp. 891–895, Nov. 2004, doi: 10.1038/nmat1251.
- [72] C.-R. Lin, Y.-M. Chu, and S.-C. Wang, “Magnetic properties of magnetite nanoparticles prepared by mechanochemical reaction,” *Material Letters*, vol. 60, no. 4, pp. 447–450, Feb. 2006, doi: 10.1016/j.matlet.2005.09.009.
- [73] D. A. Baker, “Investigation of Composite Solid Propellant Burning Rate Temperature Sensitivity,” Purdue University. [Online]. Available: <https://www.proquest.com/docview/302665070?pq-origsite=gscholar&fromopenview=true&sourcetype=Dissertations%20&%20Theses#>

- [74] V. V Kulkarni, A. R. Kulkarni, P. A. Phawade, and J. P. Agrawal, “A Study on the Effect of Additives on Temperature Sensitivity in Composite Propellants,” *Propellants, Explosives, Pyrotechnics*, vol. 26, no. 3, pp. 125–129, Jun. 2001, doi: 10.1002/1521-4087(200106)26:3<125::AID-PREP125>3.0.CO;2-8.
- [75] G. Tambourine and E. Bazilevskaya, “Particle Size Analysis,” The Pennsylvania State University Materials Research Institute. [Online]. Available: <https://www.mri.psu.edu/materials-characterization-lab/characterization-techniques/particle-size-analysis>
- [76] K. Wang and J. Gray, “Transmission Electron Microscopy,” The Pennsylvania State University Materials Research Institute. [Online]. Available: <https://www.mri.psu.edu/materials-characterization-lab/characterization-techniques/transmission-electron-microscopy>
- [77] M. Buchner, K. Höfler, B. Henne, V. Ney, and A. Ney, “Tutorial: Basic principles, limits of detection, and pitfalls of highly sensitive SQUID magnetometry for nanomagnetism and spintronics,” *J Appl Phys*, vol. 124, no. 16, p. 161101, Oct. 2018, doi: 10.1063/1.5045299.
- [78] “Qing Wang | Penn State Department of Materials Science and Engineering.” Accessed: Mar. 17, 2024. [Online]. Available: <https://www.matse.psu.edu/directory/qing-wang>
- [79] D. A. Reese, S. F. Son, and L. J. Groven, “Preparation and characterization of energetic crystals with nanoparticle inclusions,” *Propellants, Explosives, Pyrotechnics*, vol. 37, no. 6, pp. 635–638, Dec. 2012, doi: 10.1002/prop.201200142.
- [80] S. F. Son, B. C. Terry, S. Isert, T. R. Sippel, I. E. Gunduz, and L. J. Groven, “Encapsulated Nanoscale Particles and Inclusions in Solid Propellant Ingredients,” *Energetic Nanomaterials: Synthesis, Characterization, and Application*, pp. 323–340, Jan. 2016, doi: 10.1016/B978-0-12-802710-3.00012-X.
- [81] D. J. Ramirez, “Personal Communication.” Dec. 2023.
- [82] L. C. Landers, C. B. Stanley, and D. W. Ricks, “Propellant development for the Advanced Solid Rocket Motor,” in *AIAA 27th Joint Propulsion Conference*, Sacramento: American Institute of Aeronautics and Astronautics (AIAA), Jun. 1991. doi: 10.2514/6.1991-2074.

Appendix A: Material Characterization

A.1 XRD Analysis for Magnetic Susceptors

X-Ray Diffraction (XRD) was performed on the magnetic susceptors from NanoAmor® to validate the composition of the materials. This was performed by Penn State's Materials Characterization Lab (MCL). The patterns were collected at 40kV and 40mA on a 240mm radius Panalytical Empyrean® theta-theta X-ray diffractometer equipped with a line source [Co K- α 1-2 (1.789010/1.792900 Å)] X-ray tube. Data was collected with a step size of 0.0334° from 10-120° 2-theta. The incident optics consisted of a Bragg-Brentano HD® Co optic fitted with 0.04rad. Soller slits, a 10mm beam mask, 1/8° and 1/2° divergence, and anti-scatter slit respectively. The diffracted optics included an X'Celerator® detector with a 2.1223 active length in scanning line mode with a 1/4° programmable anti-scatter slit and 0.04 rad Soller slits. Phase ID was carried out using Jade® software (version 8.7) from Materials Data Inc. (MDI) and the International Centre for Diffraction Data (ICDD) PDF4® database. The results matched expectations for all three susceptors, confirming the composition and phase were correct. Figure A.1.1 through Figure A.1.3 show the collected patterns.

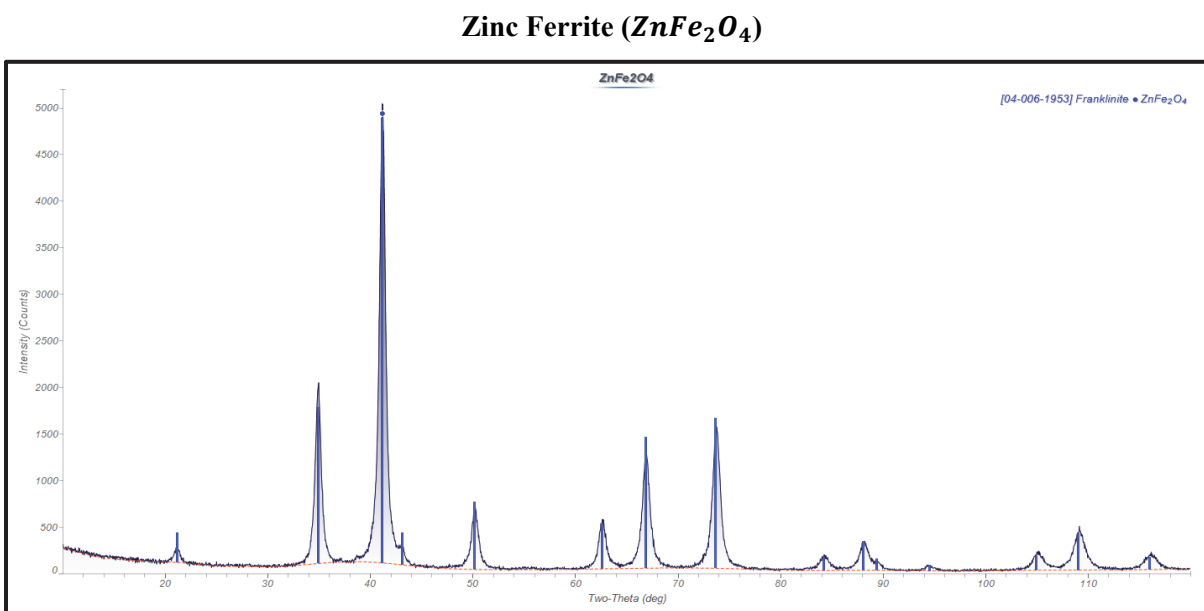


Figure A.1.1: XRD results for zinc ferrite from NanoAmor®

Cobalt Ferrite (CoFe_2O_4)

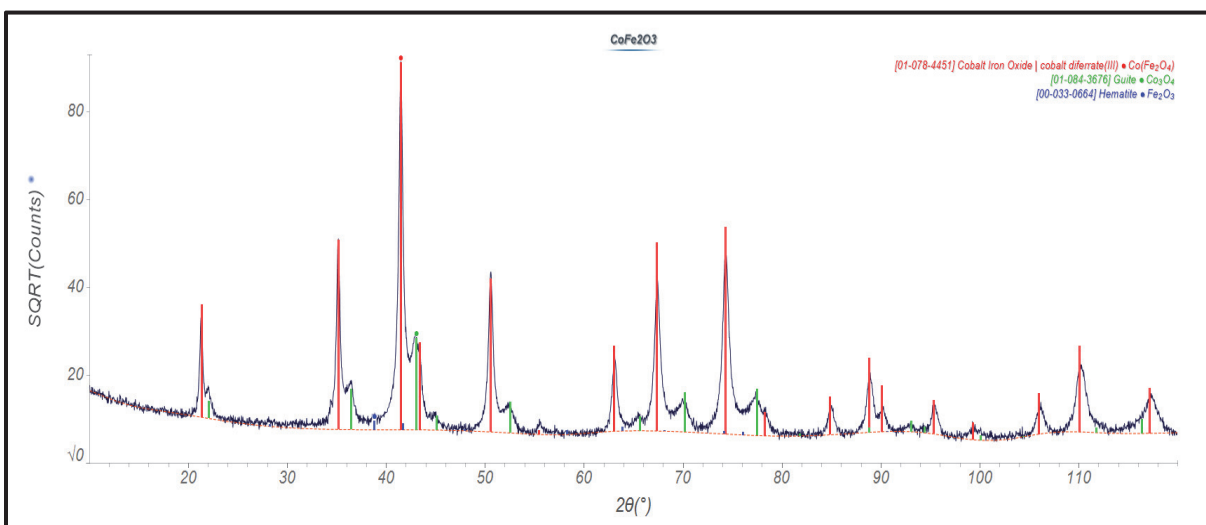


Figure A.1.2: XRD results for cobalt ferrite from NanoAmor®

Magnetite (Fe_3O_4)

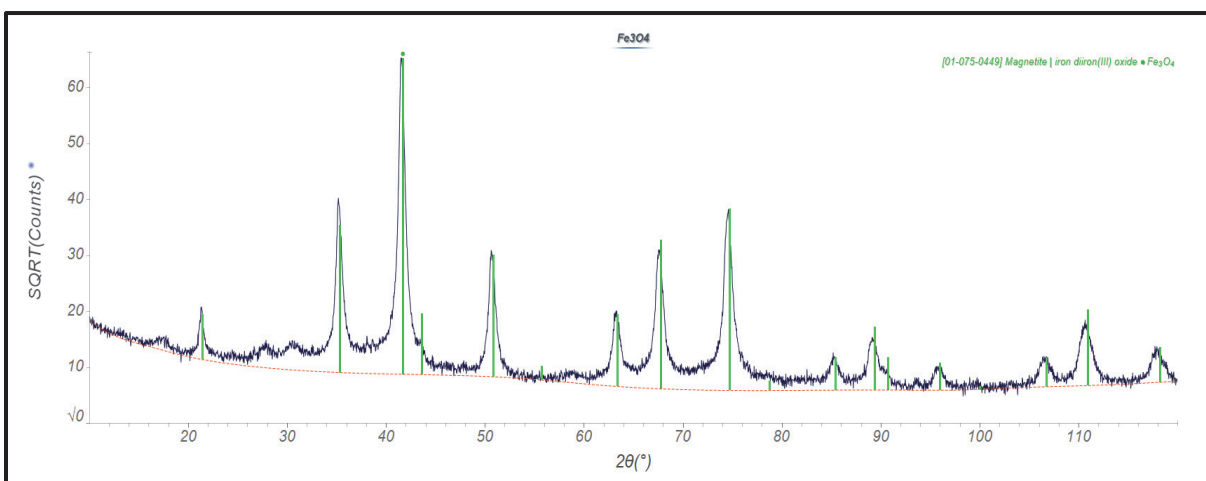


Figure A.1.3: XRD results for magnetite from NanoAmor®

A.2 Particle Size Analysis

Penn State's Materials Characterization Lab (MCL) performed particle size analysis on the zinc ferrite, cobalt ferrite, and magnetite nanoparticles using three methods. First, with dynamic light scattering (DLS) on a Malvern Zetasizer Nano ZS. DLS uses the Brownian motion of particles suspended in a fluid to determine the diffusion coefficient [75]. The diffusion coefficient is used to calculate hydrodynamic diameter of the particles [75]. For this test, the susceptors were suspended in water and shaken by hand for a few seconds to disperse the particles. The results from this test were unexpected. Figure A.2.1 through Figure A.2.3, show the particle size distribution plots for each susceptor. While the sizes were expected to be around 30nm for magnetite, 35-55nm for cobalt ferrite, and 40nm for zinc ferrite, all three had distributions around 1000nm (1 μ m). It was concluded that this result is most likely caused by poor dispersion or agglomerations.

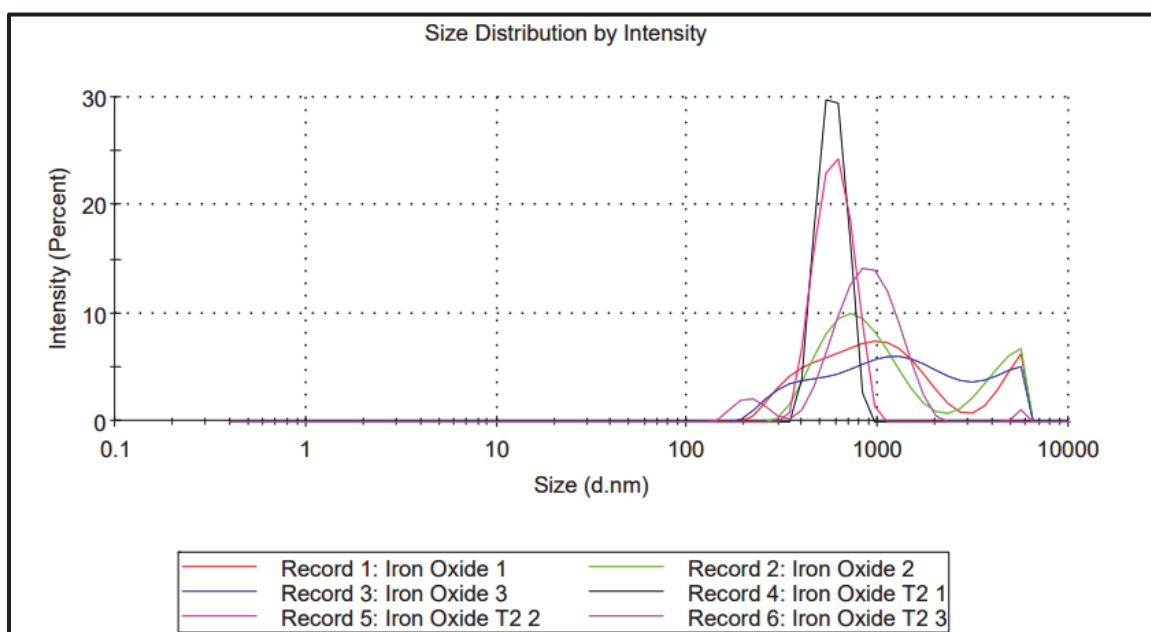


Figure A.2.1: Particle size distribution results for magnetite on Malvern Zetasizer Nano ZS provided by MCL.

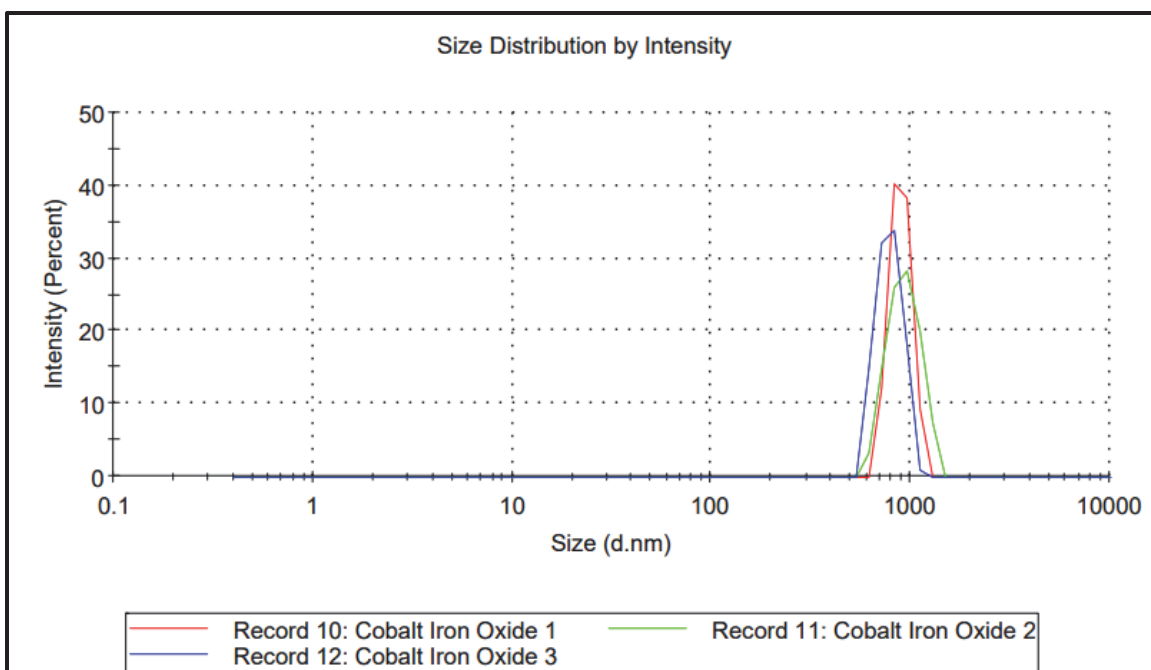


Figure A.2.2: Particle size distribution results for cobalt ferrite on Malvern Zetasizer Nano ZS provided by MCL.

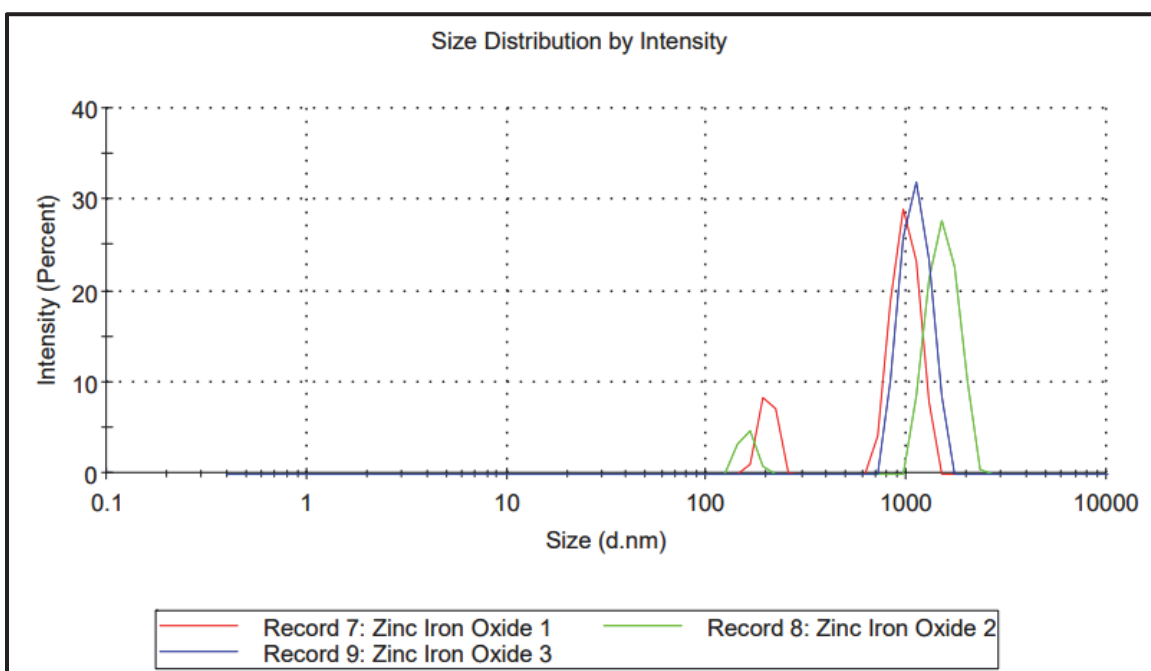


Figure A.2.3: Particle size distribution results for zinc ferrite on Malvern Zetasizer Nano ZS provided by MCL.

MCL suggested a retest using a different method, laser diffraction on a Mastersizer 3000. Laser diffraction measures light scattering to determine particle size [75]. The angles and light intensity of the measured diffraction pattern are related to particle size [75]. Larger particles create narrower angles with a

higher intensity than smaller ones [75]. For this test, the particles were suspended in ethanol and 20-30 seconds of sonication was used for dispersion. Figure A.2.4 through Figure A.2.6, show the results from this testing method for each susceptor. Unfortunately, this method also provided particle size distributions around $1\mu\text{m}$ (1000nm). The decision was made that agglomerations and poor dispersion are an issue with both methods of characterization.

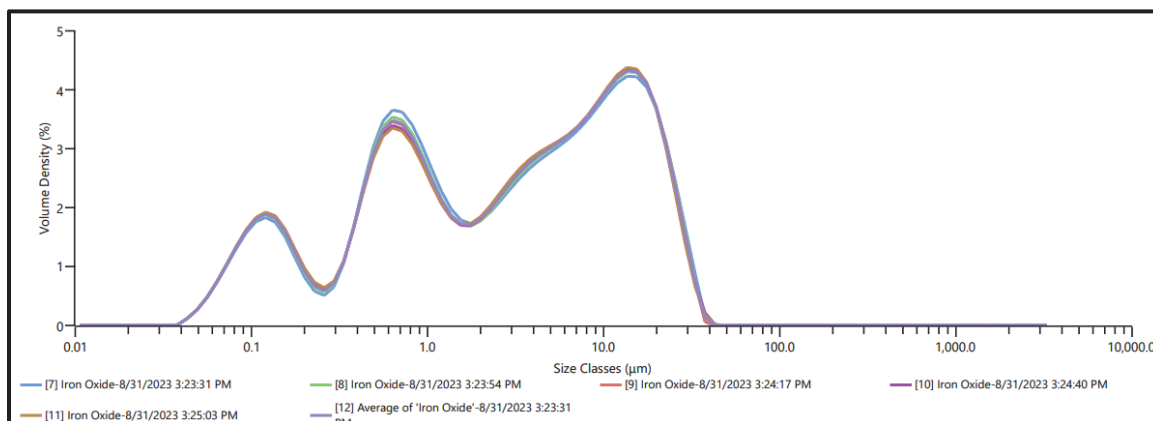


Figure A.2.4: Particle size distribution results for magnetite on Mastersizer 3000 provided by MCL.

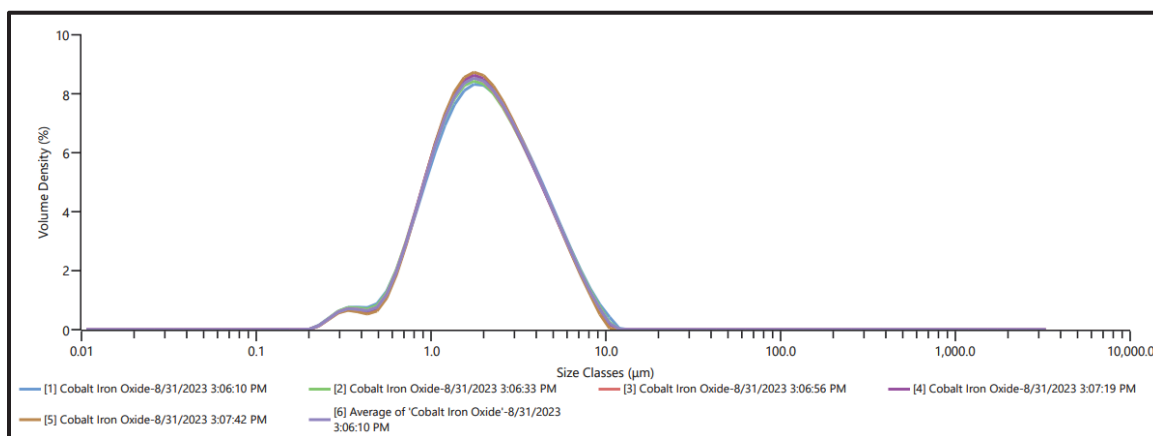


Figure A.2.5: Particle size distribution results for cobalt ferrite on Mastersizer 3000 provided by MCL.

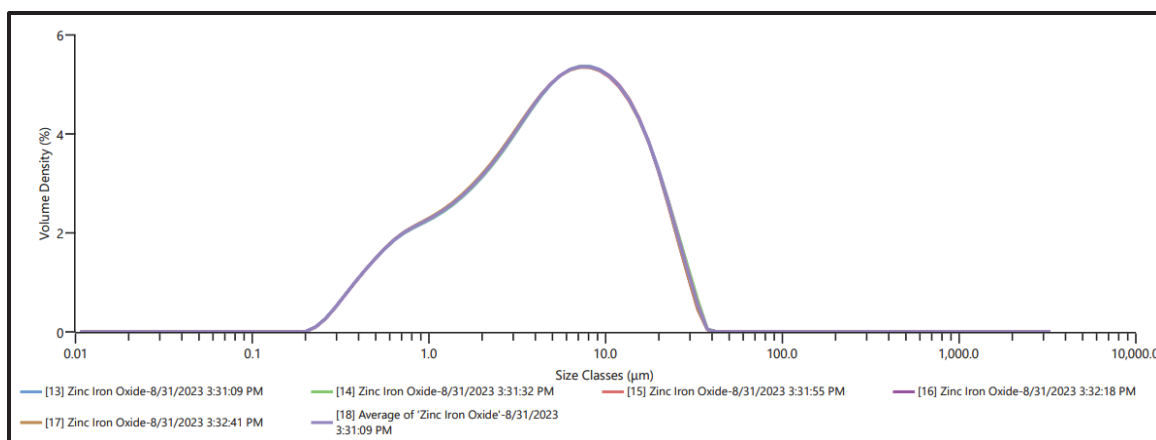


Figure A.2.6: Particle size distribution results for zinc ferrite on Mastersizer 3000 provided by MCL.

After testing with propellant and fuel samples containing the NanoAmor® 30nm magnetite particles (discussed in chapters 3 and 4), there was further need for a rough particle size distribution. Transmission Electron Microscopic (TEM) imaging was used to perform this characterization. TEM is a form of electron microscopy in which a high kV electron beam is transmitted to a super thin sample [76]. The portion of electrons that flow through the sample are called the direct beam which generates high contrast images that provide information about the specimen's mass and size [76]. Other information can be gathered from TEM, but for this analysis only imaging was necessary. MCL took images of the magnetite powder suspended in epoxy with a Titan³ G2 microscope. ImageJ [51] processing software was used to estimate the diameters of the particles. Across four TEM images, 127 particles were measured (Figure A.2.7). The average particle size is $15.60 \pm 5.07 \text{ nm}$ with the distribution portrayed in Figure A.2.8. It should be noted that this result may be biased toward smaller particles due to difficulty of differentiating particles.

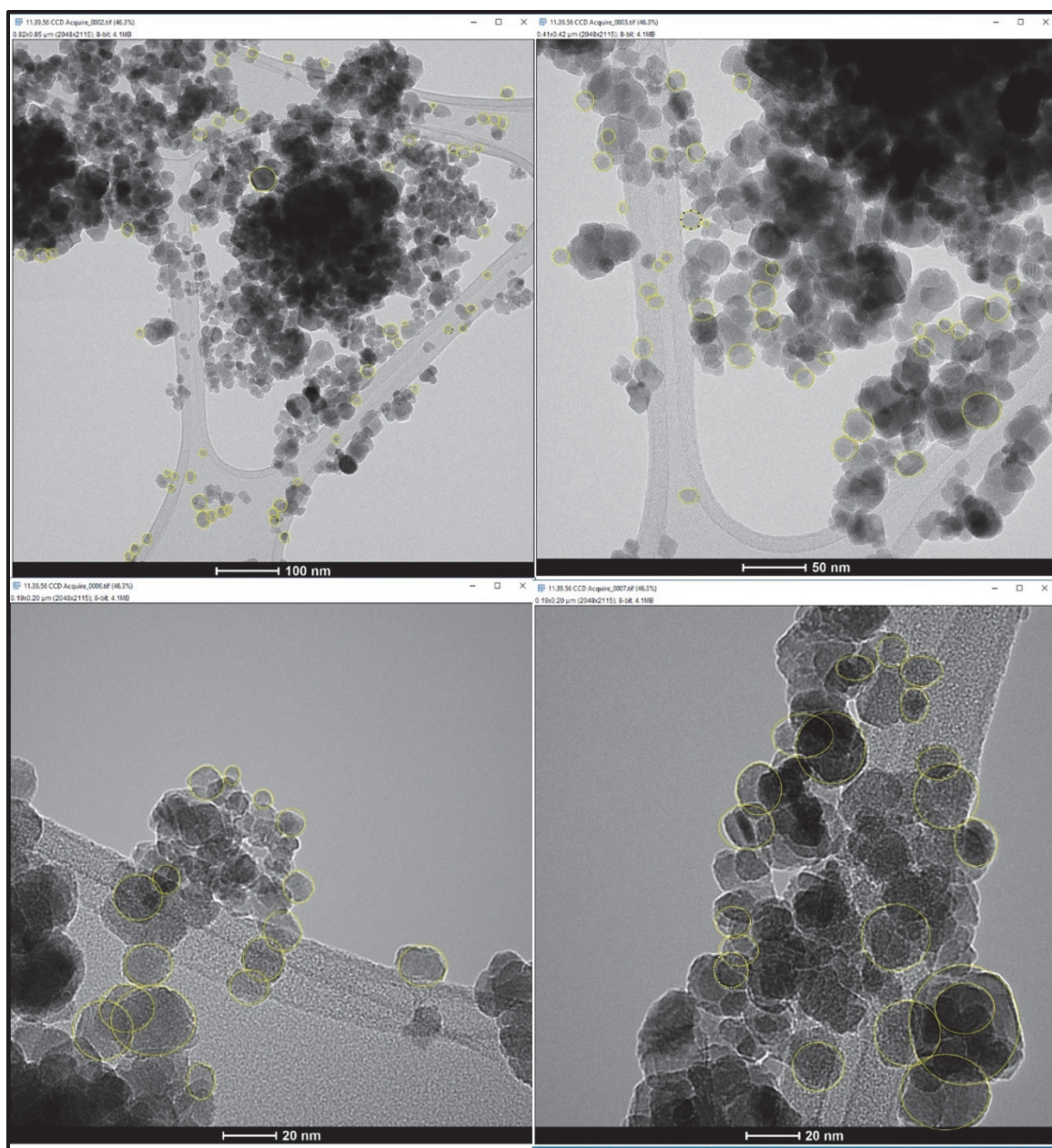


Figure A.2.7: Transmission electron microscope (TEM) images used to estimate particle size distribution of NanoAmor® 30nm Fe_3O_4 MNPs. The yellow circles were added during image processing with ImageJ to measure the diameter of 127 particles across the four images.

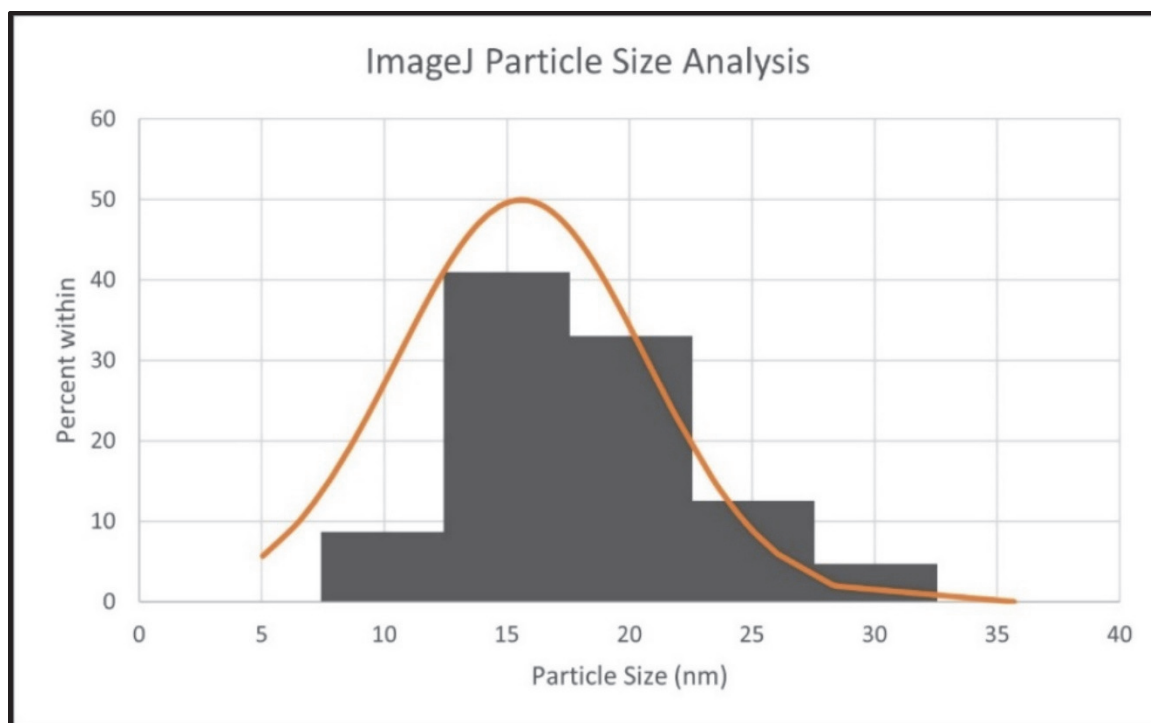


Figure A.2.8: Estimated particle size distribution of NanoAmor® 30nm Fe_3O_4 MNPs based on TEM images and processing with ImageJ.

A.3 DC SQUID Magnetometer Data

A DC superconducting quantum interference device (SQUID) magnetometer [64] was used to find hysteresis curves at various magnetic field strengths for the 30nm magnetite powder. A SQUID magnetometer is one of the most sensitive equipment used in magnetometry which allows for characterization of samples with low magnetic moments and/or coercivity. They are commonly used by the fields of nanomagnetism and spintronics. Buchner et al. provides more information on how SQUID magnetometers work and how to interpret the data [77]. For the present study, Figures A.3.1 through A.3.6 show the hysteresis curves generated by the 30nm magnetite particles for magnetic field strengths of 70000, 500, 200, 100, and 50Oe. The 70000Oe field provides information about the saturation magnetization of our particles, while the other curves can be used to understand heating power. However, as discussed in Section 4.3.1, these curves are not representative of the full heating power generated in our fuel samples because of Néel Relaxation times. The DC magnetometer takes about an hour to complete one loop, therefore any particles with a Néel relaxation time less than an hour are not captured in this data. An AC magnetometer with a frequency similar to that of the UltraFlex induction heater (789kHz) would provide a more applicable hysteresis curve for estimating heating power. However, such equipment was not available for use by this study.

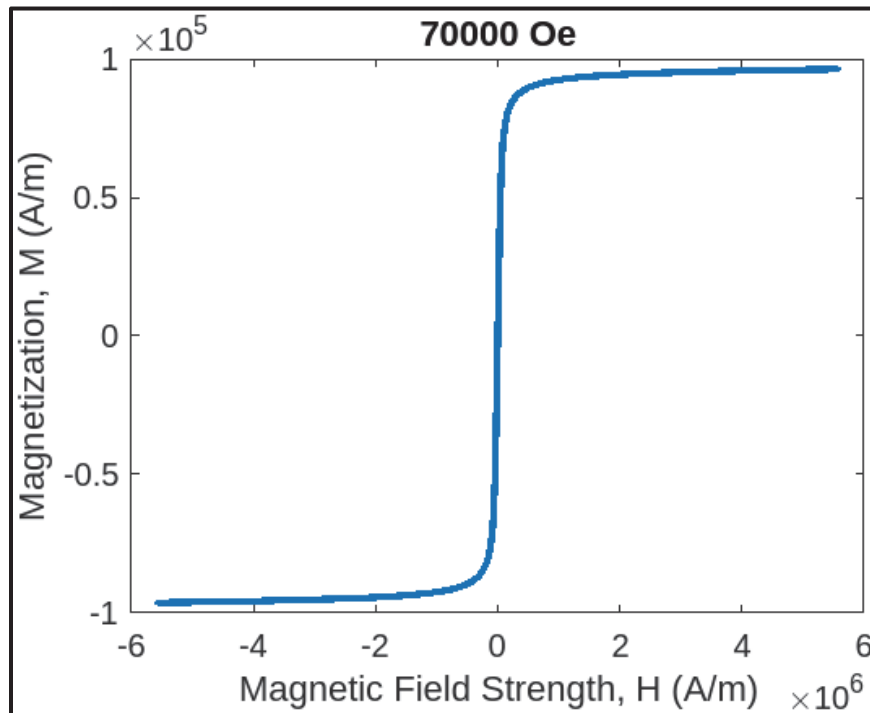


Figure A.3.1: DC SQUID Magnetometer data for 30nm magnetite in 70000Oe field.

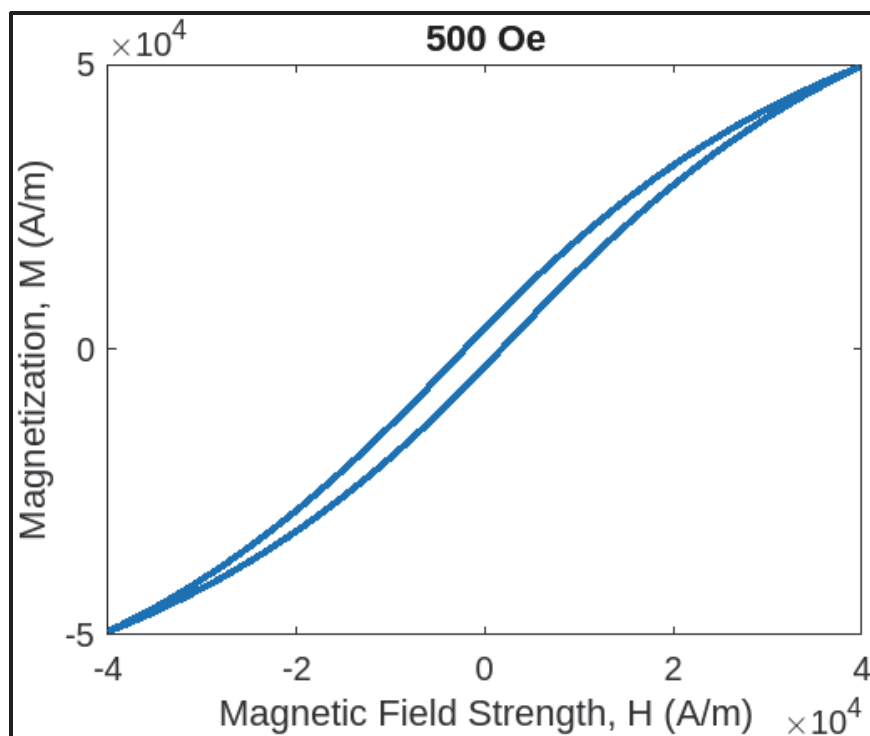


Figure A.3.2: DC SQUID Magnetometer data for 30nm magnetite in a 500Oe field.

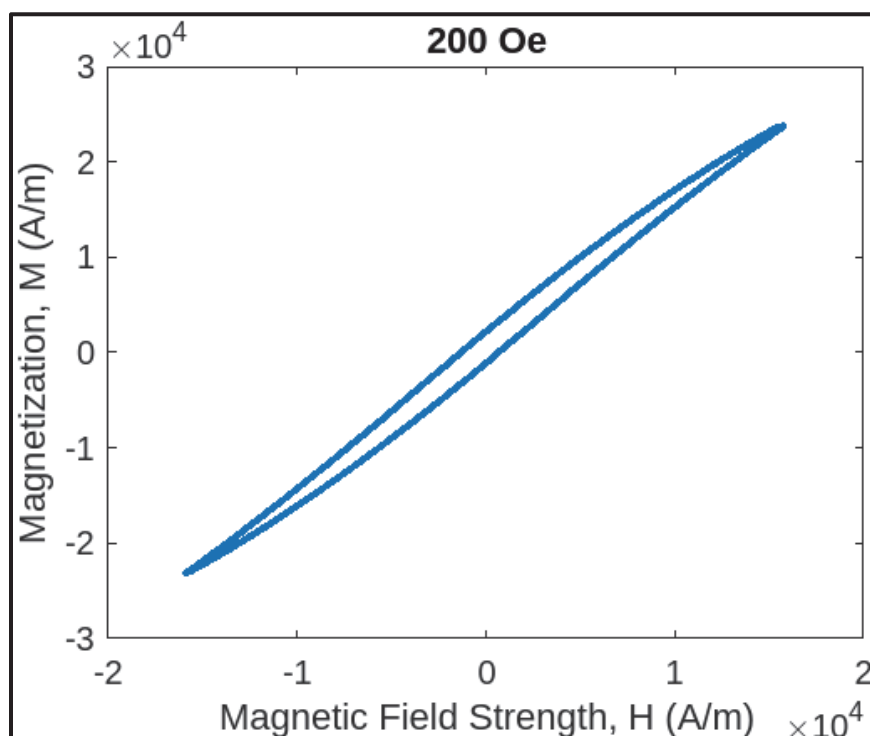


Figure A.3.3: DC SQUID Magnetometer data for 30nm magnetite in a 200Oe field.

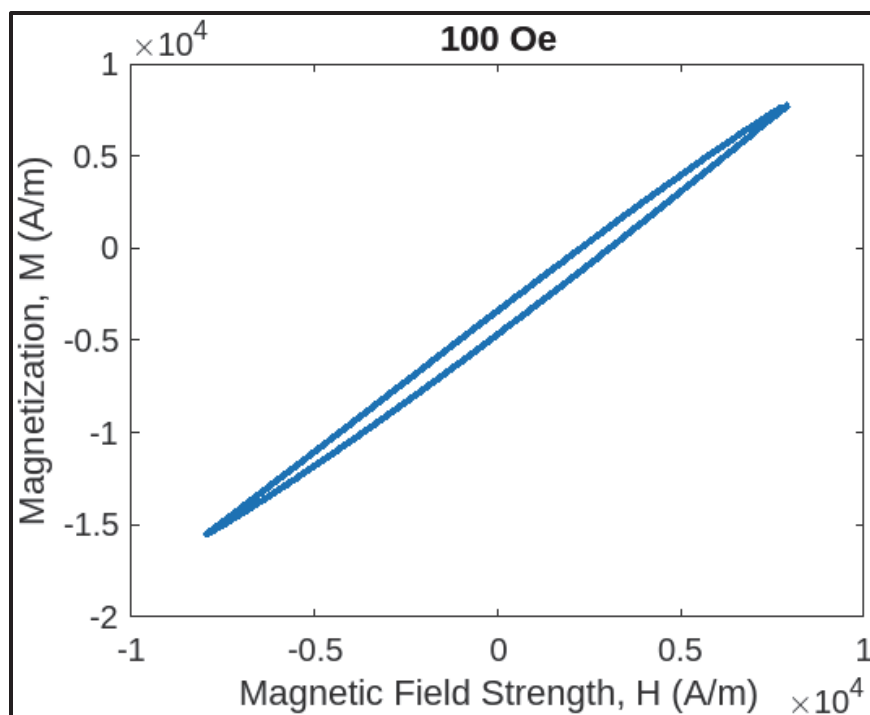


Figure A.3.4: DC SQUID Magnetometer data for 30nm magnetite in a 100Oe field.

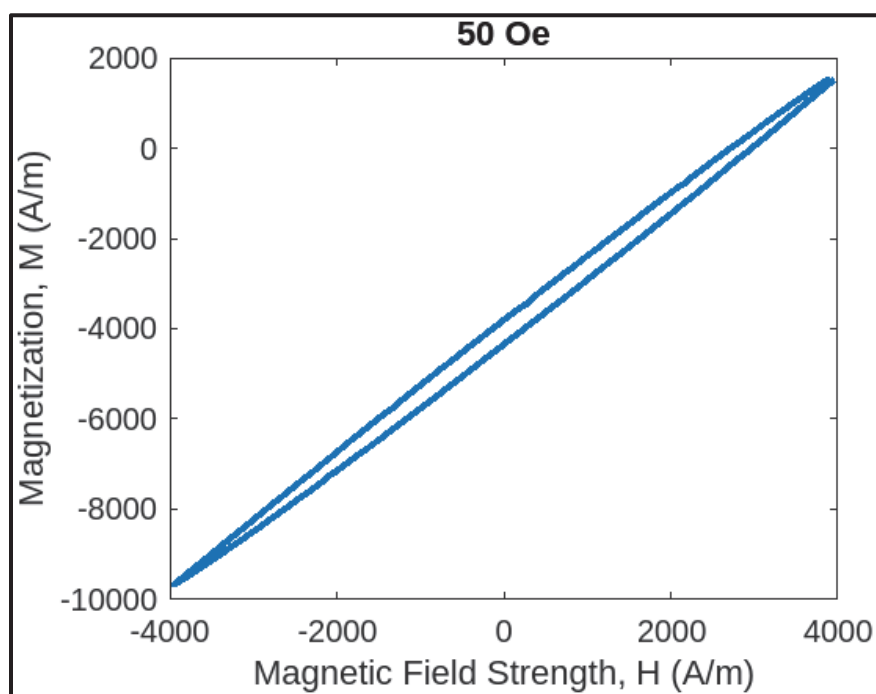


Figure A.3.5: DC SQUID Magnetometer data for 30nm magnetite in a 50Oe field.

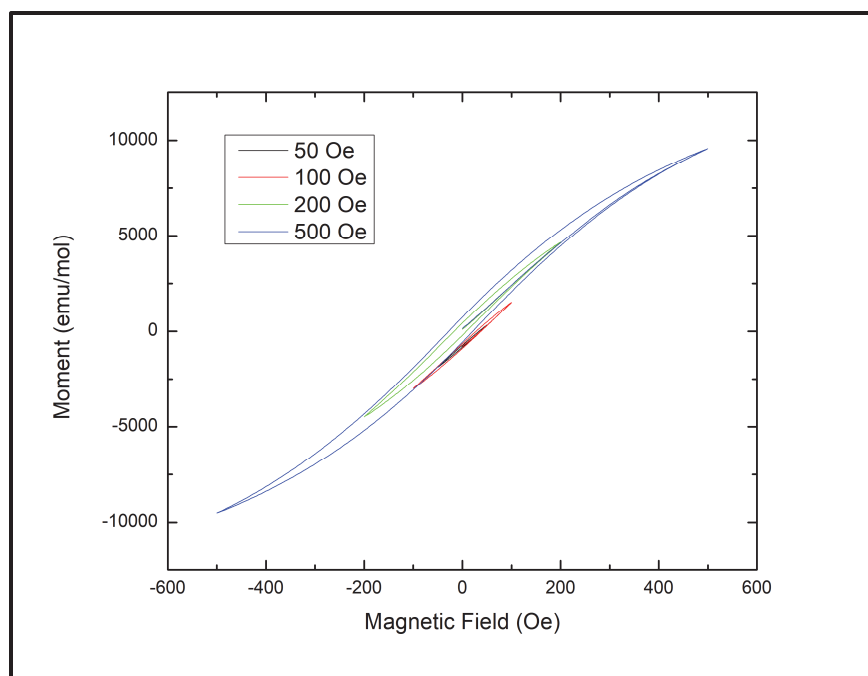


Figure A.3.6: Combine figure of hysteresis curves produced by 50, 100, 200, and 500Oe fields for 30nm magnetite.

Appendix B: AP Encapsulation Study

There was interest in investigating if MNPs encapsulated inside AP crystals impacted samples differently than MNPs dispersed with AP crystals throughout a sample. To explore this, induction heating tests completed in conjunction with Dr. Qing Wang's [78] laboratory at Penn State.

Dr. Wang's group crystalized AP particles with encapsulated maghemite ($\gamma - \text{Fe}_2\text{O}_3$) and magnetite (Fe_3O_4). The process outlined by Groven and Son was followed [30], [79-80]. Three different amounts of MNPs were investigated: 1wt%, 5wt%, and 10wt%. The Yetter Group heated these particles with an UltraFlex SB-3/1200 induction heater. Results of the initial testing of AP with embedded $\gamma - \text{Fe}_2\text{O}_3$ is shown in Table 2. For testing, the particles were placed in a small pile on a glass slide and heated on the 15 Amp setting for 15 seconds. The AP particles with magnetite have not yet been tested. It is hypothesized that slightly higher temperatures will be reached based on the results of the neat powder heating tests already discussed in Section 4.2.

Table B.1: Results of AP with Encapsulated Iron Oxide Heating Tests

Weight Percent	Maximum temperature (°C)
1wt%	25.6
5wt%	60.0
10wt%	147.2

The Yetter group is developing HTPB films containing AP with encapsulated MNPs. The procedure for manufacture of the films can be found in Appendix C. Heat testing of initial films with 40wt% solids loading was performed in the UltraFlex heater. Three films were manufactured, one for each batch of AP with encapsulated magnetite (1wt%, 5wt%, and 10wt% MNPs). The weight percent of MNPs reported is the amount used to develop AP/magnetite encapsulations; thus, the actual weight percent of AP and magnetite is not known. Current efforts by Dr. Wang are underway to determine the actual composition of the AP encapsulated magnetite. The results are in Figure B.1. The films aim to observe the heating of particles dispersed in a polymer binder. It should allow for the analysis of individual particles as opposed to the influence of a cluster of particles. Casting the AP in HTPB should also reduce the convective heat loss at each particle's surface to the surroundings.

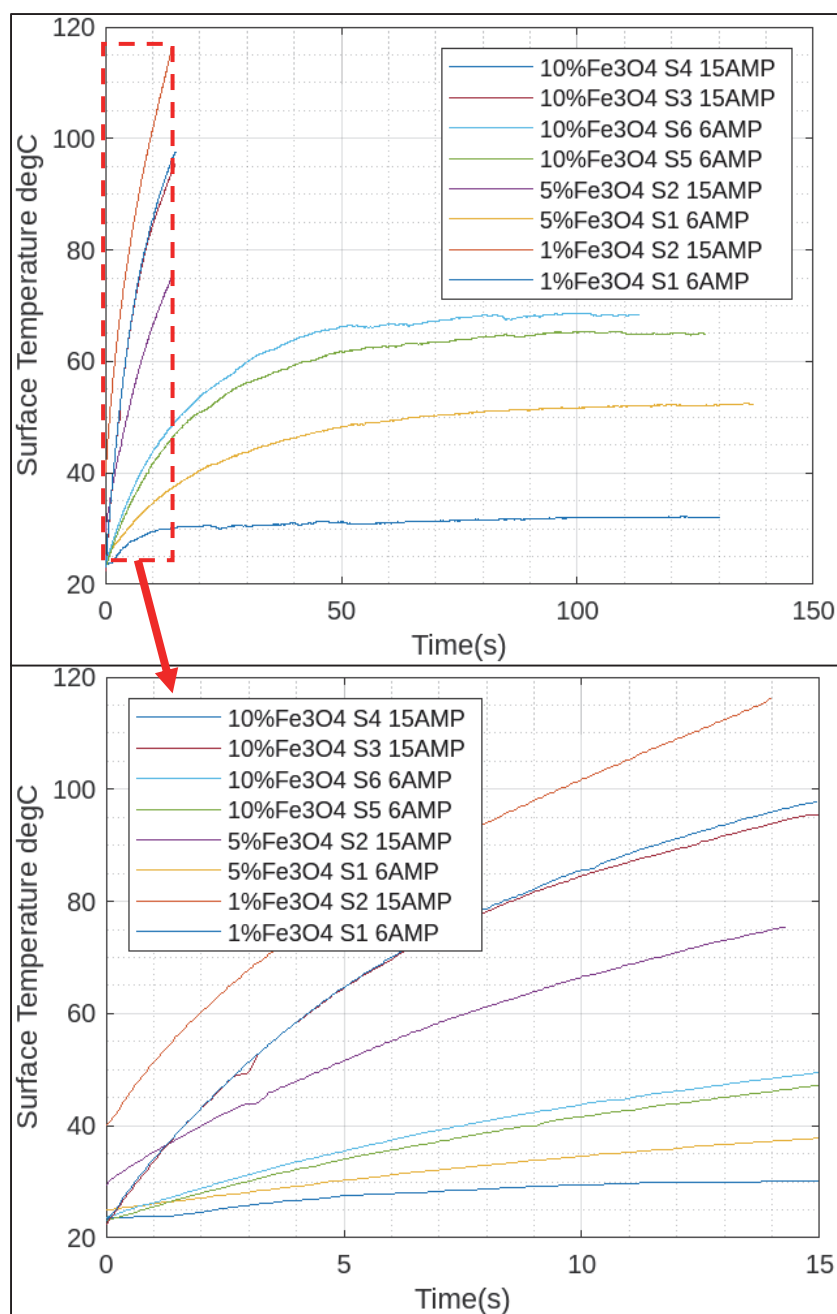


Figure B.1: Thermal profile of AP encapsulated magnetite in HTPB films. Films contain 40% AP encapsulated magnetite.

None of the tests performed with the AP encapsulation resulted in an ignition event. Differential scanning calorimetry (DSC) and thermogravimetric (TGA) measurements determined that the lower-temperature decomposition of AP with 30nm magnetite starts at 290°C and the high-temperature decomposition occurs at 340°C (Figures B.2 and B.3). Therefore, it is unsurprising that the films did not exhibit an ignition event. Future efforts involve increasing the solids loading of AP encapsulated HTPB to increase the amount of heat generated and, thus, the ultimate temperature reached.

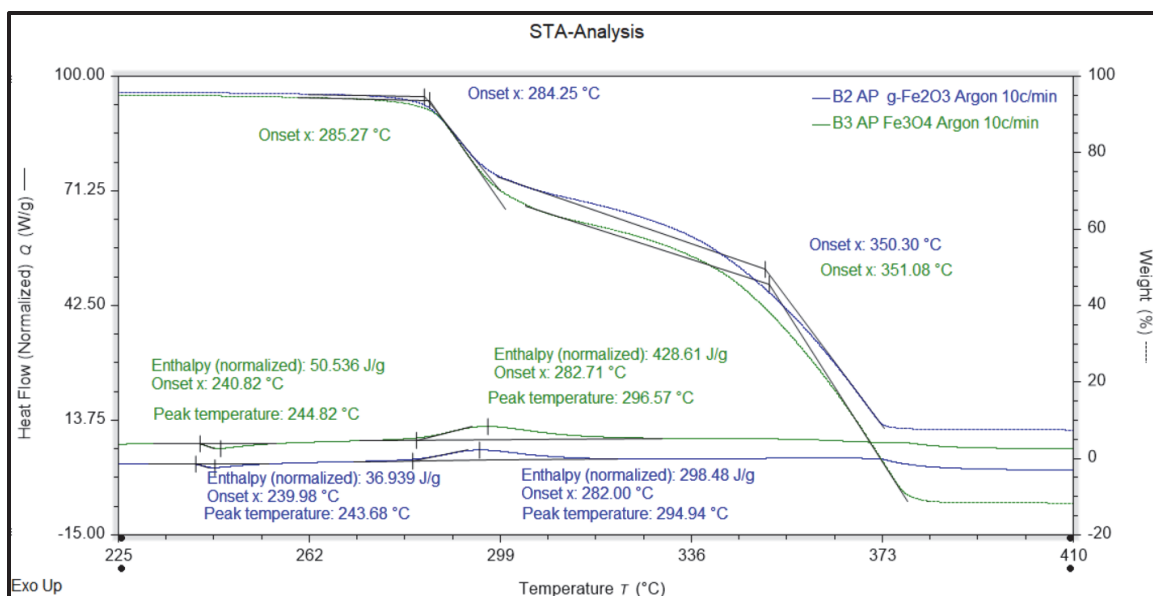


Figure B.2: Results from STA performed by MCL on iron oxide and AP particles.

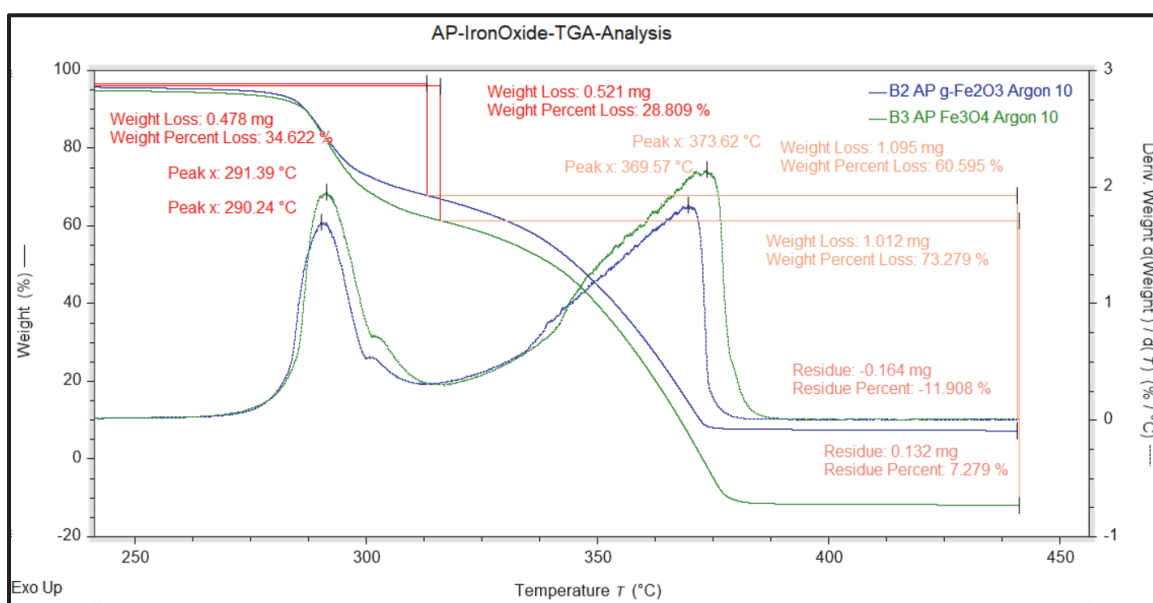


Figure B.3: More results from STA (TGA and DSC) analysis performed by MCL on iron oxide and AP particles.

Appendix C: Standard Operating Procedures

This appendix includes all standard operating procedures (SOP) developed for using equipment and less formal procedures followed for sample preparation. The order of these procedures are as follows: SOP for MTI 25kW SP-25A Desktop induction heater, SOP for the UltraFlex SB 3/1200 induction heater, procedure for mixing and casting fuel/propellant samples, procedure for manufacturing HTPB films filled with magnetite particles that are encapsulated in AP.

C.1 MTI 25kW Desktop Induction Heater SOP

PROCEDURE FOR GENERAL OPERATION OF AND HEATING VARIOUS SAMPLE TYPES WITH AN MTI SP25 DESKTOP INDUCTION HEATER

High-Pressure Combustion Laboratory
Department of Mechanical Engineering
The Pennsylvania State University

Authored By: Kirstin Walz
Master Student

Date: August 15th, 2023

THE PENNSYLVANIA STATE UNIVERSITY
UNIVERSITY PARK, PA 16802

I. INTRODUCTION

i. Purpose

The purpose of this document is to establish safe operating procedures for operating an induction heater and performing heating tests on various sample types using the induction heater. The induction heater is the MTI SP25 Desktop Induction Heater. Sample types include films composed of a polymer and magnetic nanoparticles (MNP), casted strands of hydroxyl terminated polybutadiene (HTPB) and MNP, and casted strands of HTPB, ammonium perchlorate (AP), and MNP.

ii. Scope

This standard operating procedure (SOP) applies to general operation of the MTI SP25 Desktop Induction Heater and heating tests of various samples using the induction heater. Sample preparation is discussed in a separate SOP.

iii. Applicability

This SOP applies to all those involved with the High-Pressure Combustion Laboratory who assist in the operation of the MTI SP25 Desktop Induction Heater, including students, staff, visiting personnel, and any other personnel.

iv. Responsibility

Professor Richard A. Yetter is responsible for the overall enforcement of this SOP. Prof. Yetter is further responsible for that only trained personnel are assigned to these operations and that all personnel are informed of all the hazards associated with this experimental procedure.

The experimentalists/researchers/graduate students (E/R/GS) are responsible for following this SOP and overall on-site implementation of the experiments, including taking necessary actions to protect all personnel, equipment, and facilities from any explosion, fragmentation, or fire resulting from a process under their control. The individuals in charge of this process ensure that all personnel assigned to this program have been adequately trained. In addition, prior to any operation, all participating personnel must be thoroughly briefed on duties, responsibilities, and hazards that may be involved.

II. SAFETY

i. Personnel Limits

It is recommended that at least two people are present during operations in case a problem, malfunction, or emergency occurs. Due to the size of the test bay, only one person is required to be in the bay during operation.

ii. Hazardous Materials

Samples will contain various materials that produce different exhaust gases when burned. Understanding the products of a combustion reaction for each sample type is important to the health of the operator in the room during testing. As new samples are made, hazardous combustion products shall be researched.

iii. General Safety Requirements

All personnel involved shall have completed the Environmental Health and Safety Laboratory Safety Training and reviewed the separate Hazard Analysis document before performing any processes outlined in this SOP.

Do NOT touch the coil during operation. To generate a magnetic field, the induction heater flows an alternating current ranging from 200-1000 Amps through the coil.

Do NOT place metal inside or near the coil during operation. The magnetic field produced by the coil will heat up magnetic and most metal objects to a high enough temperature to burn a person in a matter of seconds.

A foot pedal will be used to operate the induction heater from a distance. The pedal will have a safety mechanism to ensure the coil cannot be accidentally turned on while a person is near the coil.

An exhaust fan shall be running while testing is in progress to quickly remove any gases produced by the combustion of a sample from the room.

iv. Personal Protective Equipment (PPE) Requirements

While operating the induction heater, the following PPE is required.

- Safety glasses
- Lab coat
- Closed-toed shoes
- Long pants

v. Malfunction or Emergency

- For a life-threatening emergency such as an explosion, fire, etc., dial 911 for emergency response and contact Dr. Boyer at 814-826-8017 and EHS at 814-865-6391.
- For non-life-threatening emergencies, notify Prof. Yetter, Dr. Boyer, and EHS. The appropriate medical attention should be sought if warranted by the responder for the persons exposed to the hazard.
- EHS will begin an investigation into the circumstances of the event. The system in question shall remain out of service pending the investigation results and completion of any corrective actions if needed.

vi. Emergency Procedures

1. In the case of a **SMALL FIRE**:
 - 1.1. Call Dr. Boyer, Dr. Yetter, and EHS. Their phone numbers can be found under the Malfunction or Emergency section.
 - 1.2. If the fire is deemed small enough to safely extinguish, use flooding amounts of water. If flooding amounts of water is unavailable, a CO₂ or dry chemical fire extinguisher may be used.
 - 1.3. If the fire is too large to safely extinguish, do NOT open any doors to the bay with the fire. Alert all personnel in the building to the fire. Call 911, pull the fire alarm, and evacuate the building.
2. In the case of **ELECTRICAL SHOCK**:
 - 2.1. Unplug the induction heater from the wall outlet located in room 127 by the door between rooms 127 and 128, shown in Figure C.1.4.
 - 2.2. Call 911 if medical attention is required.
 - 2.3. Call Dr. Boyer, Dr. Yetter, and EHS. Their phone numbers can be found under the Malfunction or Emergency section.

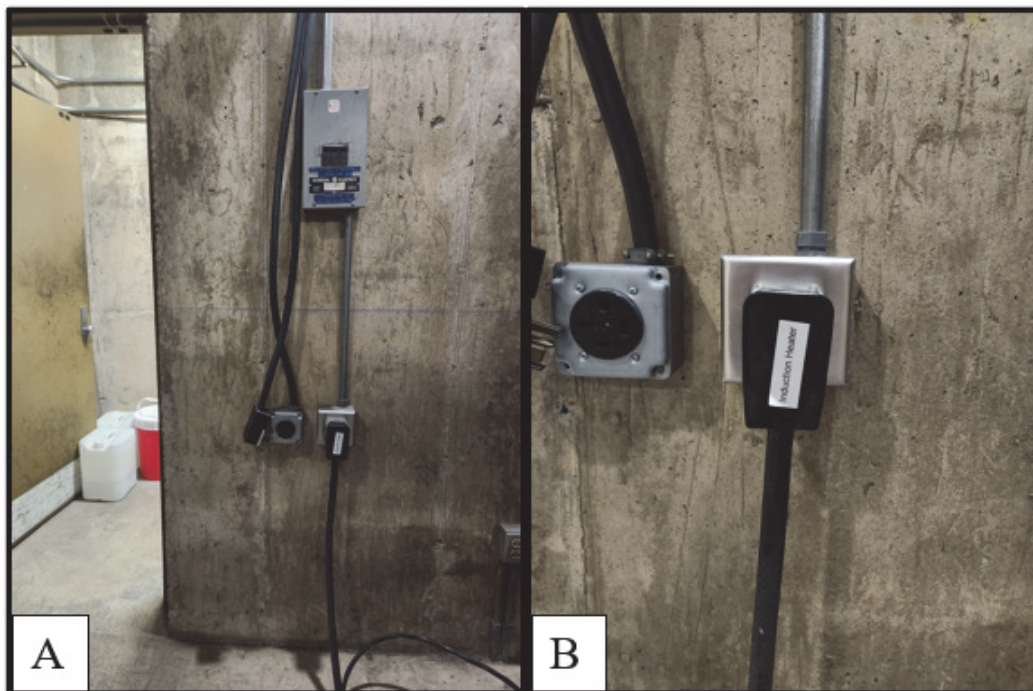


Figure C.1.4: A. Location of induction heater outlet inside room 127, by the door between rooms 127 and 128. B. A close-up of the outlet, the correct plug is labeled "induction heater."

III. MATERIALS

i. Testing Equipment

- PPE See section *iv. Personal Protective Equipment (PPE) Requirements*
- Samples
- Sample holder
- MTI SP25 Desktop Induction Heater
- Micro-Epsilon TIM 160 IR camera (or comparable IR camera)
- Sony DCR SX85 video camera (or comparable video camera)
- Two tripods for the cameras
- Laptop with TIMConnect Software for the IR camera
- “MURI – Induction Heating Datasheets” binder with the “Heat Test Log”

IV. SEQUENCE OF OPERATIONS

i. Initial Setup

1. Check the test setup for hazards.
 - 1.1. Ensure no metal is touching the coil.
 - 1.2. Ensure all water lines are attached.
 - 1.3. Ensure there is a clear walkway between the operator's seat and the exits.
2. Ensure the main power switch on the back of the heater is switched off. See Figure C.1.5.

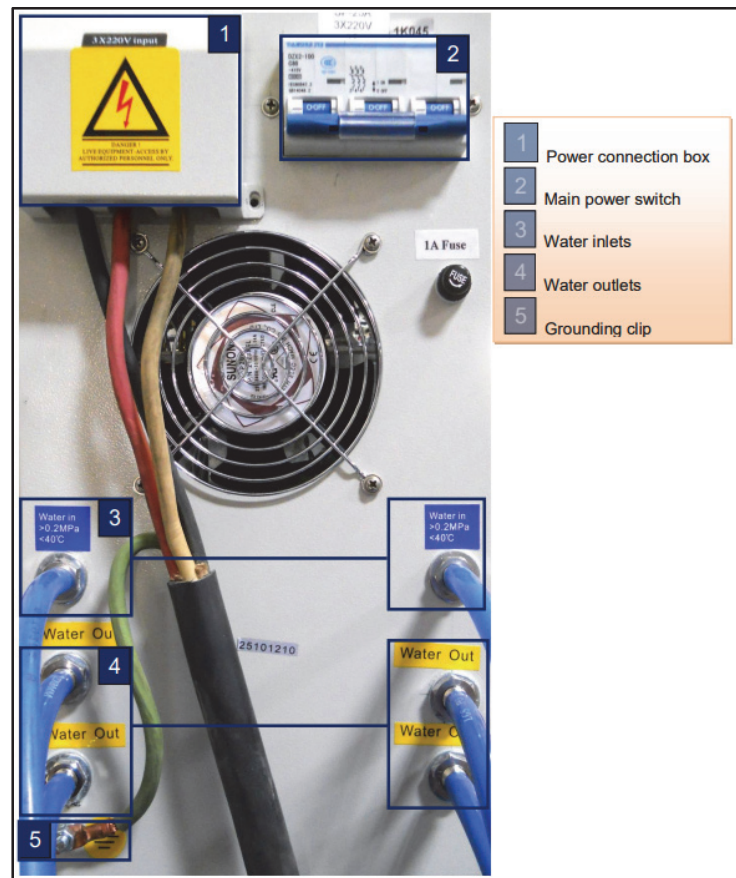


Figure C.1.5: Back panel of the MTI SP25 Desktop Induction Heater. [1]

3. Ensure the power switch on the front of the heater is switched off. See Figure C.1.6.

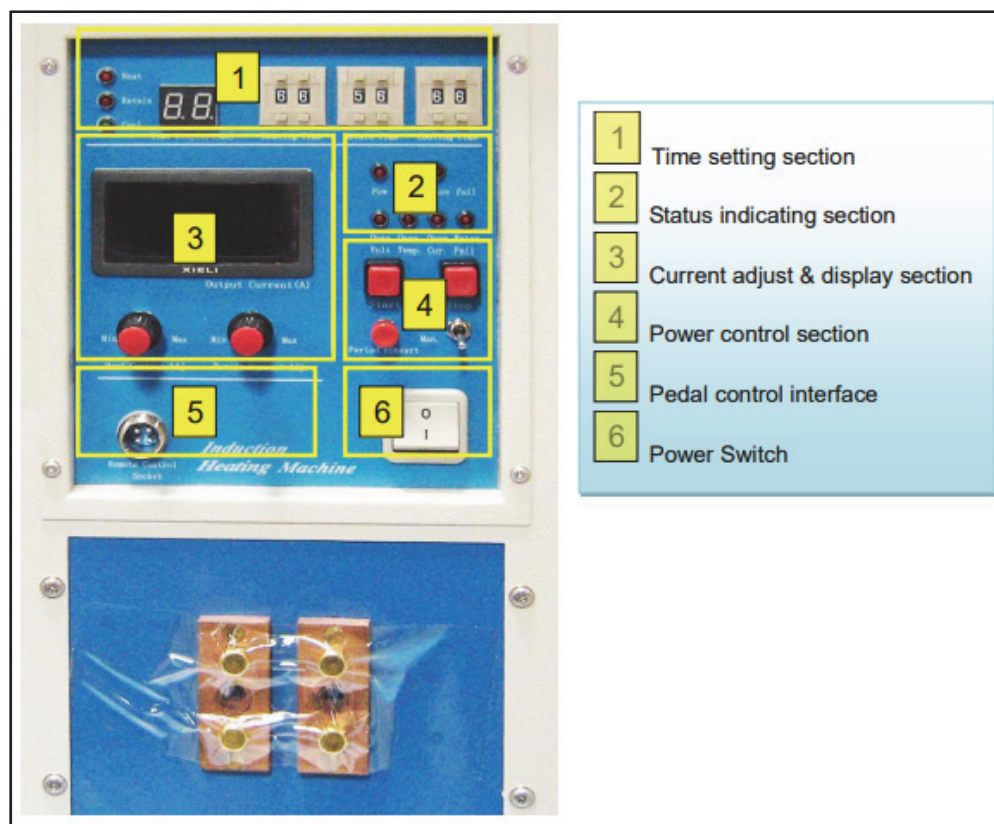


Figure C.1.6: Front panel of the MTI SP25 Desktop Induction Heater. [1]

4. Turn on the exhaust fan in room 128.
5. Check that the video camera is charged and set up on a tripod.
6. Plug in and turn on the laptop. Make sure TIMConnect software is installed.
7. Plug the IR camera into the computer, remove the lens cap, and focus the camera.
 - 7.1. Check that the ambient temperature reading makes sense.
 - 7.2. Set the emissivity to that of your sample to be tested. For more information about the IR camera or the TIMConnect software see the manuals listed in the references section. [2] [3] [4]

ii. General Operating Instructions

1. Complete section *i. Initial Setup* before operating the induction heater.
2. Turn on the water. See Figure C.1.7.

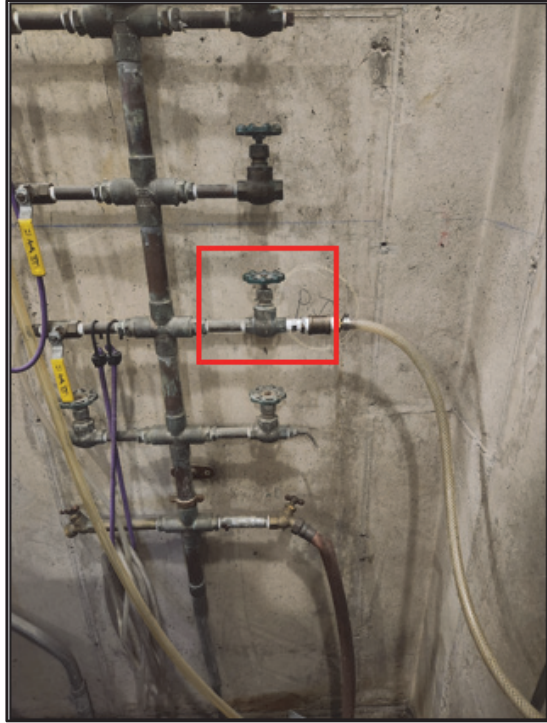


Figure C.1.7: The red box is around the water valve for turning on and off the cooling water for the induction heater.

3. Make sure the flow meter reads about 2. See Figure C.1.8.



Figure C.1.8: This flow meter will read 2, when the metal cylinder inside is aligned with the 2.

4. Check for leaks. If there is a very small drip leak, it is ok to continue. If there is a bigger leak, turn off the water and fix the issue before continuing.
5. Plug in the induction heater. The outlet is in room 127, by the door between rooms 127 and 128. See Figure C.1.4.
6. Turn on the main power switch on the back of the heater. See Figure C.1.5.
7. Ensure the foot pedal has a safety block in place. See Figure C.1.9A.

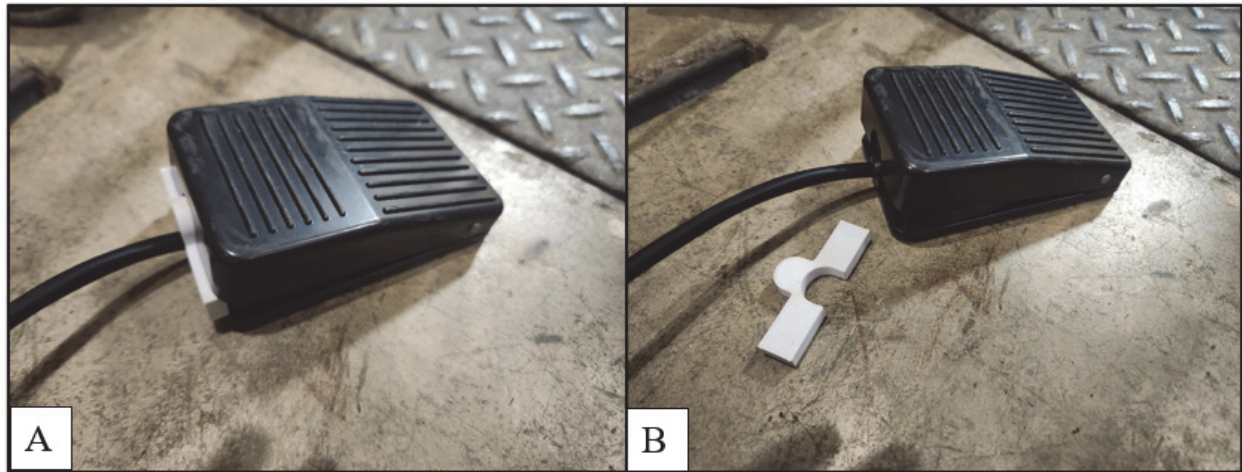


Figure C.1.9: A. Foot pedal with safety block in place. B. Foot pedal with safety block removed.

8. Turn on the power switch on the front of the heater. See Figure C.1.6.
9. The current adjustment knob is used to set the output current. See Figure C.1.10. The minimum setting is about 185 Amps (A) the maximum setting is about 1100A. **For the health of the internal circuitry of the induction heater, it is recommended that the current does not exceed 800A. The heater should also not be run for more than 60 seconds when using 600-800A.** To see what current is being used the coil must be running. The best process is to guess a setting and then check by running the coil for a few seconds. The next few steps will discuss how to run the coil.



Figure C.1.10: Current adjustment knobs and current display screen.

10. To operate in manual mode with the foot pedal:

10.1. Ensure the foot pedal is attached and the heater is set to manual. See Figure C.1.11.

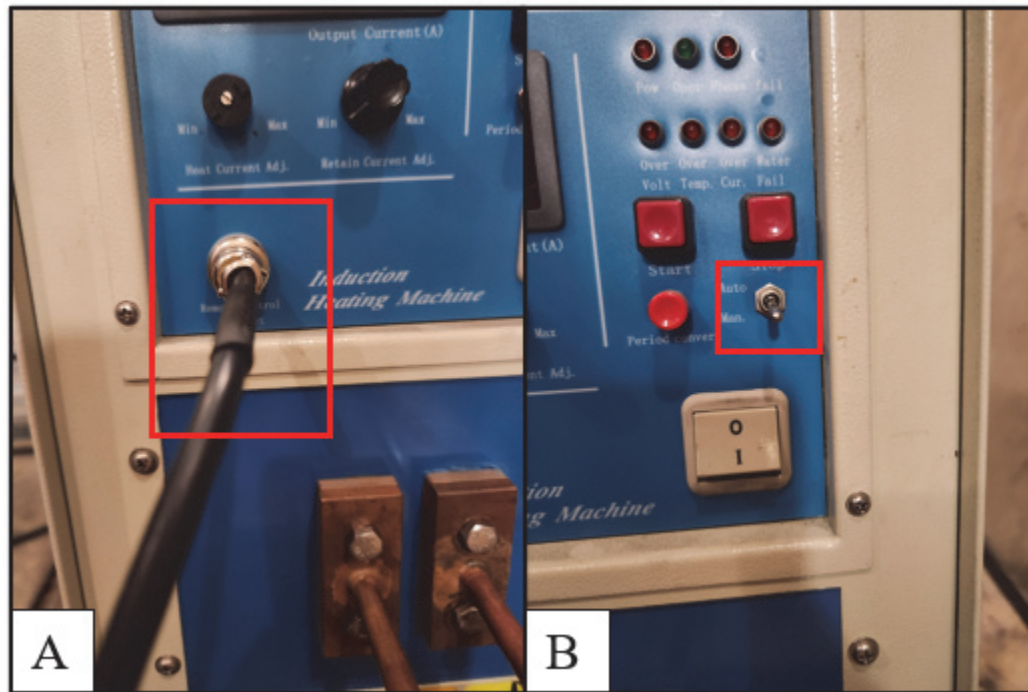


Figure C.1.11: A. Shows the correct attachment for the foot pedal. B. Shows the switch for automatic vs manual operating mode.

10.2. Remove the safety block from the foot pedal. See Figure C.1.9B.

10.3. Press and hold down the foot pedal to run current through the coil. Releasing the pedal will stop the operation. Pressing the stop button will also stop the operation if needed.

10.4. There is a timer displayed on the front panel of the heater. See Figure C.1.12. **If operating at currents of 600A-800A, do NOT run more than 60 seconds at a time.**



Figure C.1.12: Induction heater timer and operation indicator lights. [1]

11. To operate in automatic mode, with the foot pedal:

11.1. Ensure the foot pedal is attached and the heater is set to automatic. See Figure C.1.11.

- 11.2. Use the heat current adjustment knob to set the current while heating. See Figure C.1.10.
- 11.3. Use the retain current adjustment knob to set the current during the retain time. See Figure C.1.10.
- 11.4. The time can be set using the time setting section of the front panel. See Figure C.1.13. The unit of the time setter is seconds. **If operating at currents of 600A-800A, do NOT set the sum of the heat and retain times for more than 60 seconds.**

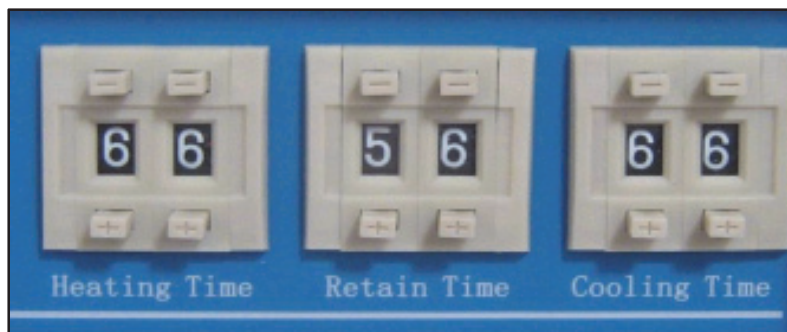


Figure C.1.13: Time setting section of the heater. [1]

- 11.5. Remove the safety block from the foot pedal. See Figure C.1.9B.
- 11.6. To start the automatic operation press and release the foot pedal. The timing will run automatically. There are three lights next to the time display that light up to show which part of the operation is being performed (heat, retain, or cooling). See Figure C.1.12.
 - 11.6.1. If the foot pedal is not in use, the operation can also be started by pressing the start button on the front panel of the heater.
- 11.7. If it becomes necessary to stop the operation before it is complete, hit the stop button on the front panel.
12. For directions on how to properly power off the heater, see section *iv. Power Off and Cleanup*.
13. For further instructions about the operation, information about the MTI SP25 Desktop Induction Heater, or guidance on troubleshooting, see the operation manual [1].

iii. Testing Procedure: Test Type 1 (surface temperature only)

1. Complete section *i. Initial Setup* before operating the induction heater.
2. Complete steps 2 through 10.1 from section *ii. General Operating Instructions*.
3. Make sure the coil is NOT running and then use the appropriate sample holder to place the sample in the coil.

4. Record the test number, batch number, sample number, operating current, and test duration in the “Heat Test Log”. Also record any other important information about the test, sample, or environmental conditions in the comments section.
5. Start recording on the regular video camera. Be sure to state the test number, batch number, sample number, and target operating current.
6. Press the record button on the IR camera software. See Figure C.1.14.

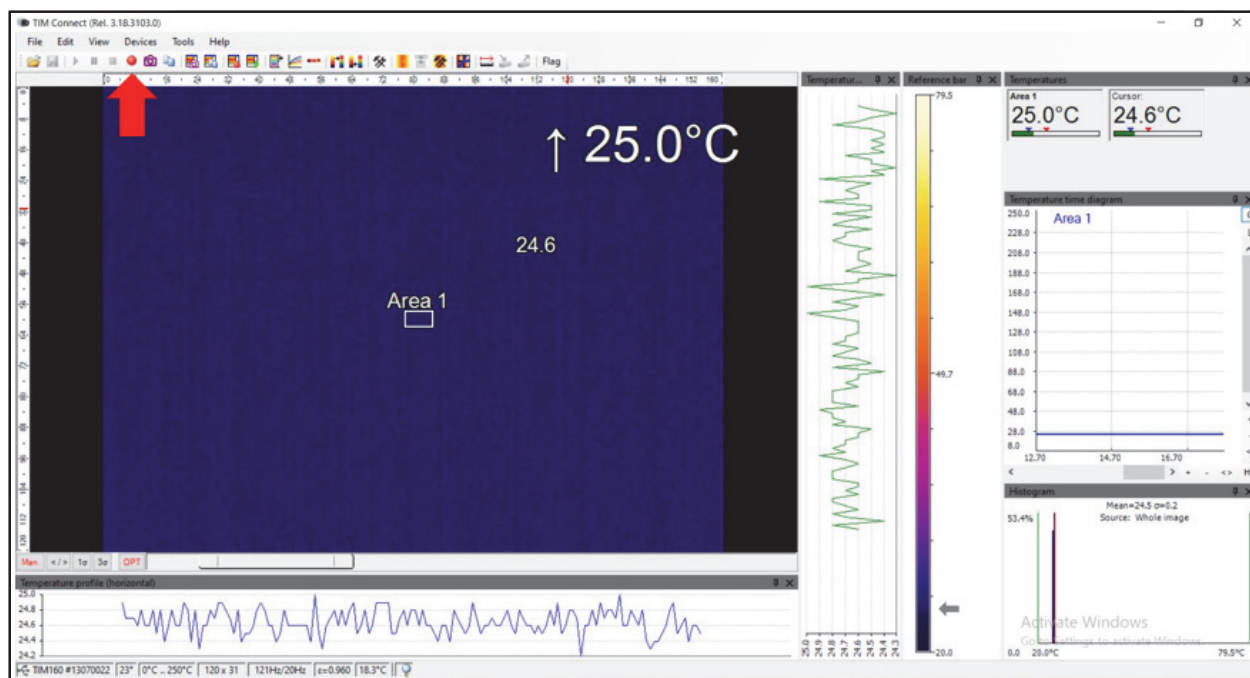


Figure C.1.14: TIMConnect Software. The red arrow is pointing to the record button.

7. Remove the safety block from the foot pedal. See Figure C.1.9B.
8. Press and hold the foot pedal for the desired test duration. Release the foot pedal to end the test. **If operating at currents of 600A-800A, do NOT set the sum of the heat and retain times for more than 60 seconds.**
9. Place the safety block back on the foot pedal. See Figure C.1.9A.
10. Stop the recording on the normal video camera.
11. Stop recording on the IR camera and save the file to the data drive. Use the following naming convention: T#_B#_S# See Figure C.1.15. Record the file name in the testing log.

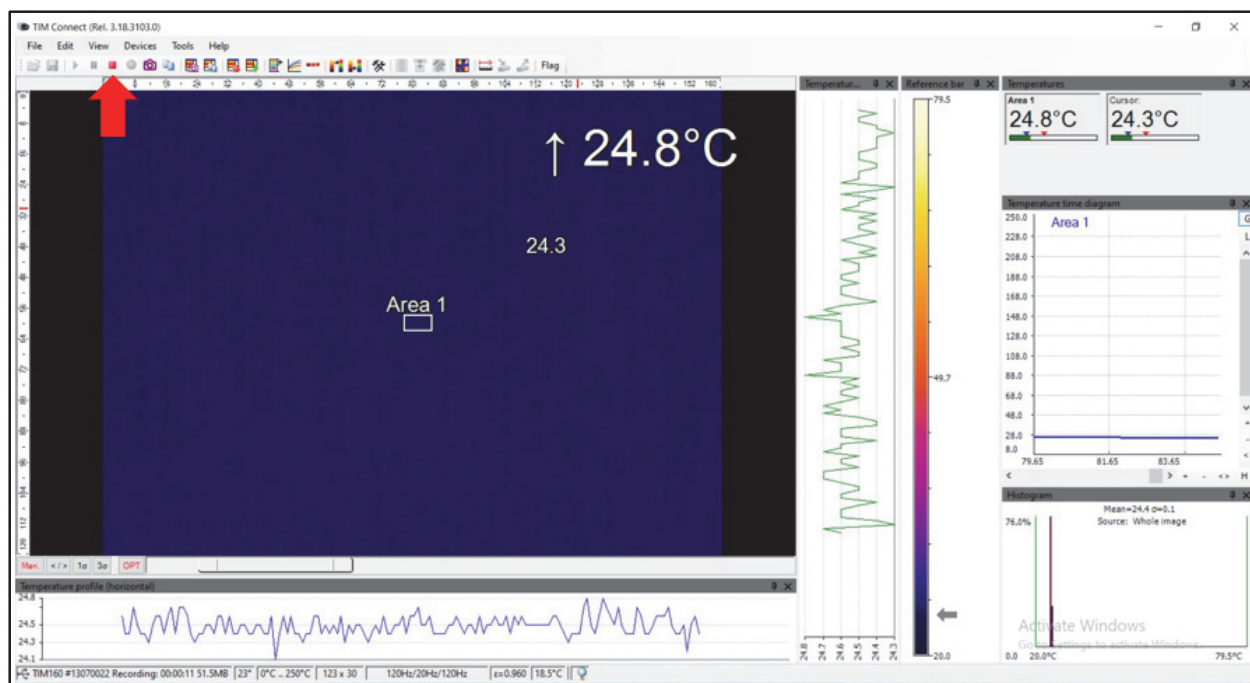


Figure C.1.15: TIMConnect Software. The red arrow is pointing to the stop recording button. This will automatically bring up a window to save the .ravi file.

12. Make sure the coil is not running, and then remove the sample from the coil.
13. If testing another sample, repeat steps 3 through 12 from section *iii. Testing Procedure: Test Type 1 (surface temperature only)*. For the health of the internal circuitry of the induction heater, give the heater a break after about half an hour of repeated testing. Follow section *iv. Power Off and Cleanup* for power down procedures.
14. If testing is complete, follow section *iv. Power Off and Cleanup* for power down procedures.

iv. Power Off and Cleanup

1. Turn off the power switch on the front panel of the heater. See Figure C.1.6.
2. Turn off the main power switch on the back panel of the heater. See Figure C.1.5.
3. Turn off the water. See Figure C.1.7.
4. Unplug the induction heater from the wall. The outlet is in room 127 by the door between rooms 127 and 128. See Figure C.1.4.
5. Place the lens cap back on the IR camera. Unplug the camera from the computer.
6. Time and temperature data can be exported from the .ravi file as a .dat file. This must be performed on a computer that has the TIMConnect software to open the .ravi file properly. The .dat type can be read

by Excel or Notepad. All files can be transferred via USB from the laptop used for testing to a computer with access to the Y drive. Save all files to the Y drive. Further data analysis can be performed as needed.

7. Turn off the video camera. The USB attached to the camera can be used to transfer video files to a computer.
8. Put all samples tested back in the proper, labeled storage container.
9. Ensure the “Heat Test Log” was properly updated. Return the “MURI – Induction Heating Datasheets” binder to the conference room table or the office.
10. Perform any other necessary clean-up, such as drying water from a small drip leak or wiping off sample holders.

REFERENCES

- [1] M. Corporation, *Desk-Top Induction Heater 30-80 KHz, 25KW (220V 3 Phase) EQ-SP-25A Operation Manual*, Richmond, California: MTI Corporation.
- [2] Micro-Epsilon, *thermoImager TIM Compact Thermal Imager*, Ortenburg, Germany: Micro-Epsilon.
- [3] Micro-Epsilon, *Operating Instructions thermoImager TIM*, Ortenburg, Germany: Micro-Epsilon.
- [4] Micro-Epsilon, *Operating Instruction thermoImager TIMConnect*, Ortenburg, Germany: Micro-Epsilon.

C.2 UltraFlex SB3/1200 Induction Heater SOP

PROCEDURE FOR GENERAL OPERATION OF AN ULTRAFLEX SB-3/1200 INDUCTION HEATER

Dr. Qing Wang's Laboratory
Millennium Science Complex
And
High Pressure Combustion Laboratory
Department of Materials Science and Engineering
The Pennsylvania State University

Authored By: Kirstin Walz
Master Student

Date: September 13th, 2023

THE PENNSYLVANIA STATE UNIVERSITY
UNIVERSITY PARK, PA 16802

I. INTRODUCTION

i. Purpose

The purpose of this document is to establish safe operating procedures for operating an induction heater and performing heating tests on various sample types using the induction heater. The induction heater is the UltraFlex SB-3/1200 Induction Heater. Sample types include films composed of polymer and magnetic nanoparticles (MNP), casted fuel grains of hydroxyl terminated polybutadiene (HTPB) and MNP, and casted propellant grains of HTPB, ammonium perchlorate (AP), and MNP.

ii. Scope

This standard operating procedure (SOP) applies to general operation of the UltraFlex SB-3/1200 Induction Heater and heating tests of various samples using the induction heater. Sample preparation is discussed in a separate SOP.

iii. Applicability

This SOP applies to all those involved with the MURI project who assist in the operation of the UltraFlex SB-3/1200 Induction Heater, including students, staff, visiting personnel, and any other personnel.

iv. Responsibility

Professor Richard A. Yetter and Professor Qing Wang are responsible for the overall enforcement of this SOP. Prof. Yetter and Prof. Wang are further responsible for that only trained personnel are assigned to these operations and that all personnel are informed of all the hazards associated with this experimental procedure.

The experimentalists/researchers/graduate students (E/R/GS) are responsible for following this SOP and overall on-site implementation of the experiments, including taking necessary actions to protect all personnel, equipment, and facilities from any explosion, fragmentation, or fire resulting from a process under their control. The individuals in charge of this process ensure that all personnel assigned to this program have been adequately trained. In addition, prior to any operation, all participating personnel must be thoroughly briefed on duties, responsibilities, and hazards that may be involved.

II. SAFETY

i. Personnel Limits

It is recommended that at least two people are present during operations in case a problem, malfunction, or emergency occurs.

ii. Hazardous Materials

The purpose of testing is to heat samples until decomposition occurs. The samples will contain various materials that produce different exhaust gases when burned.

Possible Exhaust Gases:

- Ammonia
- Chlorine
- Nitrogen Oxides
- Carbon Dioxide

iii. General Safety Requirements

All personnel involved shall have completed the Environmental Health and Safety Laboratory Safety Training and reviewed the separate Hazard Analysis document before performing any processes outlined in this SOP.

Do NOT touch the coil during operation. To generate a magnetic field, the induction heater flows an alternating current through the coil.

Do NOT place metal inside or near the coil during operation. The magnetic field produced by the coil will heat up magnetic and most metal objects to a high enough temperature to burn a person in a matter of seconds.

An exhaust fan shall be running while testing is in progress to quickly remove any gases produced by the combustion of a sample from the room.

iv. Personal Protective Equipment (PPE) Requirements

While operating the induction heater, the following PPE is required.

- Safety glasses
- Lab coat
- Closed-toed shoes
- Long pants

III. MATERIALS

i. Testing Equipment

- PPE See section *iv. Personal Protective Equipment (PPE) Requirements*
- Samples
- Sample holder
- UltraFlex SB-3/1200 Induction Heater
- Micro-Epsilon TIM 160 IR camera (or comparable IR camera)
- Laptop with TIMConnect Software for the IR camera
- “MURI – Induction Heating Datasheets” binder with the “Heat Test Log”

IV. SEQUENCE OF OPERATIONS

i. Initial Setup

8. Check the test setup for hazards.
 - 8.1. Ensure no metal is touching the coil.
 - 8.2. Ensure all water lines are attached.
 - 8.3. Ensure there is a clear walkway between the operator's seat and the exits.
9. Turn on the exhaust fan.
10. Plug in and turn on the laptop. Make sure TIMConnect software is installed.
11. Plug the IR camera into the computer, remove the lens cap, and focus the camera.
 - 11.1. Check that the ambient temperature reading makes sense.
 - 11.2. Set the emissivity to that of your sample to be tested. For more information about the IR camera or the TIMConnect software see the manuals listed in the references section. [1] [2] [3]

ii. General Operating Instructions

14. Complete section *i. Initial Setup* before operating the induction heater.
15. Turn on the UltraFlex Cooler. This circulates cooling water through the coil.
16. Check for leaks. If there is a very small drip leak, it is ok to continue. If there is a bigger leak, turn off the water and fix the issue before continuing.
17. Turn on the main power switch on the back of the UltraFlex Power Supply.
18. Following the instructions from the UltraFlex manual, adjust the output settings to the desired testing condition. Frequency, current, power, and voltage are able to be modified. The test duration can also be set.

iii. Power Off and Cleanup

11. Turn off the power switch on the back of the UltraFlex Power Supply.
12. Turn off the UltraFlex Cooler.
13. Place the lens cap back on the IR camera. Unplug the camera from the computer.
14. Time and temperature data can be exported from the .ravi file as a .dat file. This must be performed on a computer that has the TIMConnect software to open the .ravi file properly. The .dat type can be read by Excel or Notepad. All files can be transferred via USB from the laptop used for testing to a computer with access to the Y drive. Save all files to the Y drive. Further data analysis can be performed as needed.

15. Put all samples tested back in the proper, labeled storage container.
16. Ensure the “Heat Test Log” was properly updated. Return the “MURI – Induction Heating Datasheets” binder to the conference room table or the office.
17. Perform any other necessary clean-up, such as drying water from a small drip leak or wiping off sample holders.

REFERENCES

- [1] Micro-Epsilon, *thermoImager TIM Compact Thermal Imager*, Ortenburg, Germany: Micro-Epsilon.
- [2] Micro-Epsilon, *Operating Instructions thermoImager TIM*, Ortenburg, Germany: Micro-Epsilon.
- [3] Micro-Epsilon, *Operating Instruction thermoImager TIMConnect*, Ortenburg, Germany: Micro-Epsilon.

C.3 Mixing and Casting Procedures

C.3.1 Procedure for Mixing and Casting Fuel Samples

1. Wear appropriate PPE:
 - a. Safety glasses
 - b. Lab coat
 - c. Rubber gloves
2. Gather all equipment listed below:
 - a. Scale
 - b. Mix sheet
 - c. Pipet
 - d. Metal chemical spoon
 - e. Stir rod
 - f. Weight boats
 - g. Vacuum jar and vacuum pump
 - h. Enamel coated 3D printed PLA mold
3. Gather all ingredients listed below:
 - a. Firefox Enterprises Inc. Hydroxyl Terminated R-45M Poly-Butadiene Resin
 - b. Thermo Scientific Isophorone Diisocyanate 98%+ (Cat: 428602500)
 - c. Sigma-Aldrich® Bis(2-ethylhexyl) adipate (DEHA) 97%+
 - d. TCL America Dibutyltin Dilaurate >95% (Stock# D0303)
 - e. TCL America Dibutyl Phthalate >97.0% (Stock# P0292)
 - f. NanoAmor® 30nm Fe₃O₄ 99% (Stock#2654WJ) (magnetite) or desired wires
4. Fill out the mix sheet for desired solids loading, weight percentage of ingredients, and volume of the mold, it will calculate the necessary mass of each ingredient.
5. Place a weight boat on the scale and tare it. Mass out the desired amount of HTPB resin and record the value in the mix sheet.
6. Place another weight boat on the scale and tare it again. Mass out the desired amount of magnetite and record the value on the mix sheet. When making wired fuel samples, skip this step.
7. Add the magnetite to the HTPB resin. Using the stir rod slowly incorporate the magnetite. If making wired fuel samples skip this step.
8. Place the weight boat with the HTPB and magnetite on the scale and tare it. Using a pipet add the plasticizer. Record the value.
9. Tare the scale again and add the IPDI. Record the value.
10. Slowly stir until homogenous.
11. Place the weight boat in the vacuum jar and pull vacuum for 15-20 minutes.
12. For wired fuel samples, pour part of the mix into the mold, then string the wires through the mold, make sure they are taut. Then pour the rest of the mix and proceed to step 14.
13. Pour the mixture into the enamel coated mold. If necessary, place back in the vacuum jar and outgas again.
14. Place in the oven at 60 degC until cured.

C.3.2 Procedure for Mixing and Casting Propellant Samples

1. Wear appropriate PPE:
 - a. Safety glasses
 - b. Lab coat
 - c. Rubber gloves
2. Gather all equipment listed below:
 - a. Pink ESD container with normal lid and lid with vacuum port (Figure C.3.1)
 - b. Scale
 - c. Mix sheet
 - d. Pipet
 - e. Metal chemical spoon
 - f. LabRAM Resodyne Acoustic Mixer outfitted with vacuum pump option.
 - g. Weight boats
 - h. Enamel coated 3D printed PLA mold
 - i. Electrical tape
 - j. Multimeter



Figure C.3.1: Pink ESD container with both lids. The normal lid has no holes the vacuum lid has two holes.

3. Gather all ingredients listed below:
 - a. Valimet H-95 spherical aluminum powder
 - b. PyroChem Source 90- μm Ammonium Perchlorate
 - c. PyroChem Source 200- μm Ammonium Perchlorate
 - d. Firefox Enterprises Inc. Hydroxyl Terminated R-45M Poly-Butadiene Resin
 - e. Thermo Scientific Isophorone Diisocyanate 98%+ (Cat: 428602500)
 - f. Sigma-Aldrich® Bis(2-ethylhexyl) adipate (DEHA) 97%+
 - g. TCL America Dibutyltin Dilaurate >95% (Stock# D0303)
 - h. TCL America Dibutyl Phthalate >97.0% (Stock# P0292)
 - i. NanoAmor® 30nm Fe_3O_4 99% (Stock#2654WJ) (magnetite) or wires
4. Fill out the mix sheet for desired solids loading, weight percentage of ingredients, and volume of the mold, it will calculate the necessary mass of each ingredient. Note that when mixing on the LabRAM, the mixing containers fill should be between 50-70% to allow for enough material to adhere to the walls that shear layers are created while maintaining enough empty space inside the container for movement.
5. Place empty pink ESD container on the scale and tare it.

6. Add the desired amount of R45M HTPB resin and record the mass.
7. Place a weight boat on the scale, tare it again, and add the 200 μ m AP. Pour this into the pink ESD container with the HTPB resin.
8. Repeat step 7 with the 90 μ m AP.
9. Give the container a small shake to allow the AP to compact.
10. Repeat step 7 with the magnetite nanoparticles. When making wired propellant samples, skip this step.
11. Repeat step 7 with the H-95 aluminum.
12. Place the pink ESD container on the scale and tare it again. Slowly add the plasticizer in a way that wets as much of the surface of the aluminum particles as possible. This will reduce the chance of static build up.
13. Seal the container with the normal lid and tape around the edge to seal it.
14. Take the container to the LabRAM and secure it in place by clamping down on the container with the best fitting top and bottom plates.
15. Using a multimeter, check the grounding wire on the LabRAM to ensure it is properly grounded.
16. Put the LabRAM's lid on (Figure C.3.2)

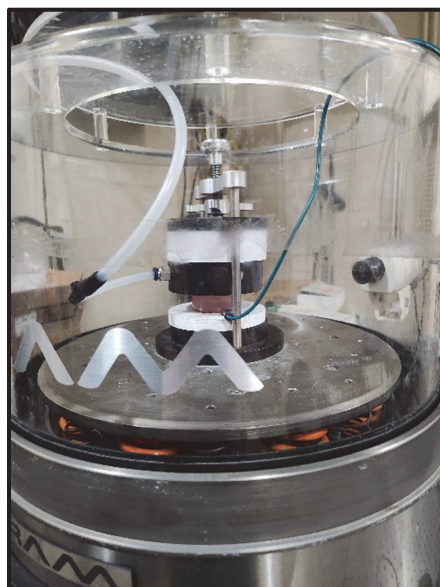


Figure C.3.2: Pink ESD container secured on the LabRAM with the lid in place. The vacuum port is in place, but this piece is not necessary unless mixing under vacuum.

17. Ensure all personnel leave the room and close the bay door.
18. Log on to the computer and open the LabRAM program.
19. Slowly ramp up the intensity percentage while checking to make sure there is nothing moving that should not be. This slow ramp allows for the mixture to become wetted before reaching high accelerations, resulting in a reduced risk of static build-up.
 - a. Start with 10%
 - b. Increase to 20%
 - c. Increase to 40%
 - d. Increase to 50% and allow to mix at this intensity for a while, making sure to check for unexpected movement.
20. Continue slowly increasing until about 80%. This equates to 70-90Gs depending on the weight percentage of nanoparticles in the mix (more nanoparticles will need higher Gs).

21. Mix for 10-20 minutes keeping an eye on the intensity vs time plot inside the software looking for fluctuations.
22. When the plot begins to flat-line with minimal oscillations it is homogenous. At this point pause the LabRAM program, lock the computer, and enter the bay.
23. Turn off the LabRAM and remove the container from the LabRAM.
24. Open the lid, use a spoon to make a small hole in the middle of the mix. Add the IPDI using a pipet to the hole, then cover the IPDI with material from the mix. This process will keep the IPDI from splashing around the container when mixing.
25. Add the vacuum lid to the ESD container and place it back on the LabRAM, make sure the vacuum pump is attached properly (Figure C.3.3).

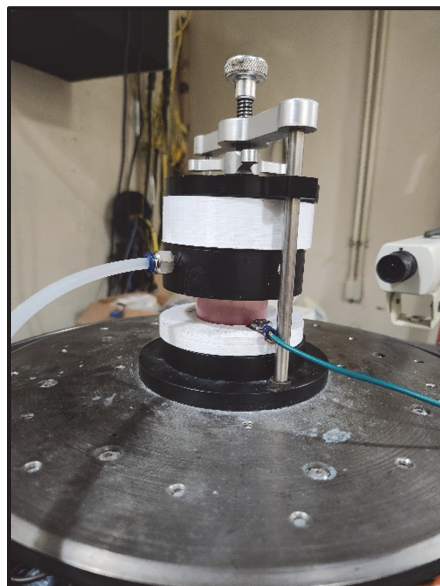


Figure C.3.3: ESD container secured on the LabRAM with vacuum port correctly attached. The lid to the LabRAM is not placed on top in this image.

26. Ensure all personnel leave the bay and shut the door.
27. Go over to the computer, log back in to the software, and begin mixing. Slowly ramp up intensity as in steps 19-20.
28. Continue mixing until homogenous, this will take a while.
29. Turn on the vacuum pump and continue mixing until homogenous.
30. Once homogenous, stop the LabRAM program, lock the computer, turn off the vacuum pump.
31. Enter the bay with the LabRAM, turn it off and remove the container. It will be warm. (in the future it would be nice to have thermocouples monitoring mix temperature)
32. When making wired fuel samples, pour part of the mix into the enamel coated mold (avoid using a spoon because that will add air bubbles), string the wires through the mold. Make sure the wires are taut and secured, then pour the rest of the mix into the mold. Skip to step 34.
33. Pour the mix from the container into the enamel coated mold. Avoid using a spoon because that will add air bubbles.
34. Place mold in an oven at 60 degC until fully cured, depending on mold size could be 3-7 days.

C.4 Procedure for Manufacturing HTPB Films with AP Encapsulations

1. Wear appropriate PPE:
 - a. Safety glasses
 - b. Lab coat
 - c. Rubber gloves
2. Gather all materials listed below:
 - a. 3D printed PLA film molds
 - b. Primer
 - c. Enamel
 - d. Mix sheet
 - e. HTPB R45M resin
 - f. IPDI
 - g. AP encapsulations
 - h. Disposable pipet
 - i. Stir rod
 - j. At least 2 weigh boats
 - k. 2 metal chemical spoons
 - l. Spatula
 - m. Scale
 - n. Vacuum pump
 - o. Vacuum jar
 - p. Chem wipes
 - q. Oven with temperature control
 - r. Acetone or Ethanol for cleaning
3. Prepare the molds by applying 2 coats of primer followed by 1-2 coats of enamel. Allow 15-20 minutes between coats for drying time. Allow for 30 minutes of wait time before casting a film into the mold.
4. Set up the mix sheet for desired solids loading and the volume of the mold. It will calculate the mass of each ingredient needed. This is also where the actual masses will need to be recorded.
5. Turn on the fume hood exhaust fan.
6. Place one weigh boat on the scale and tare the scale.
7. Using a metal chemical spoon, measure out the desired amount of HTPB R45M resin. Record this mass in the Mix Sheet. Set this weigh boat aside.
8. With the second weigh boat, perform a wet tare with the AP encapsulations. The following steps explain how to perform a wet tare:
 - a. Using the second chemical spoon, place some material in the weigh boat.
 - b. Move the weigh boat around to spread the material along the surface.

- c. Carefully pour the excess material back into the stock. There should still be a layer of material stuck to the surface of the weigh boat.
 - d. Place the weigh boat on the on the scale and tare.
9. Mass out the desired amount of AP encapsulations. Record this mass in the Mix Sheet.
10. Carefully pour the AP encapsulations into the weigh boat with the R45M resin and mix thoroughly. This will take a few minutes.
11. When all material appears to be combined. Place the weigh boat back on the scale and tare.
12. Add the desired amount of IPDI using the disposable pipet. Record the mass in the Mix Sheet.
13. Mix with the stir rod until all ingredients are fully combined. This will take a few minutes.
14. Label the film mold with batch number and % nanoparticles.
15. Carefully pour/scoop the mixture into the film mold. Fill the mold as evenly as possible. This can be tedious and take time.
16. When the mold is filled, place it in the vacuum jar and pull a vacuum for 10-20 minutes. This step can be repeated as necessary to remove bubbles.
17. Then place the mold in an oven at 60 degrees Celsius until cured (2-3 days).
18. Clean up the area and put away all chemicals properly. Be sure to purge the IPDI jar with nitrogen.
19. After the films have cured, use a 1/4" punch to punch out 4-5 circular samples from each film. Be sure to label each sample with batch number and sample number as these will be massed, measured, and tested individually.

Appendix D: Sample Formulation Mix Sheet

Provided in this section are images of the mix sheet used for all batches of propellant and fuel samples. It calculates the needed mass of each ingredient based on desired weight percentage by using recorded mold volume and ingredient densities (Figures D.1, D.3, D.4). The actual mass of each ingredient is recorded (Figure D.1). These values are used to calculate properties of the mix (Figure D.2). The sheet is modified slightly for each batch depending on sample type and desired mix characteristics. All images shown here are from hysteresis propellant batch 42.

	A	B	C	D	E	F	G	H	I	J
1	Batch Number	Chemical	Lot Number	Nominal Wt (%)	Nominal Wt (g)	Check Sum	Actual Wt (g)	Actual Wt (%)	W/EW	Actual W/EW
2	43	HTPB R45 M	1	14.80%	8.06		8.060	14.8%	0.00588	0.00588
3		Water		0.00%	0.00		0.000	0.0%	0.00000	0.00000
4		IPDI	A0449383	1.20%	0.65		0.660	1.2%		
5		DEHA		4.50%	2.45		2.460	4.5%		
6		T12 - 10%		1 drop				0.0%		
7		H-95 Al		10.00%	5.45		5.45	10.0%		
8		AP 200 um		44.25%	24.10		24.10	44.2%		
9		AP (90 um)	B7	22.75%	12.39		12.39	22.7%		
10		Fe3O4		2.50%	1.36		1.36	2.5%		
11		Total		100.00%	54.46		54.480	100.0%		

Figure D.1: Portion of mix sheet for calculating and recording the mass of each ingredient. The numbers displayed are from batch number 42.

K	L	M	N	O	P	Q	R	S	T	U
Desired Cure Ratio	Actual Cure Ratio	Calc Mix Density (g/cc)	Actual Mix Density (g/cc)	AP Coarse/Fine	Target Solids	Act% Solids	O/F	Target O/F	% TMD	Volume of Mix [cc]
1.0007		1.89	1.89	1.95	79.50%	79.48%	2.20	2.20	88%	28.754

Figure D.2: Portion of mix sheet used for calculating Cure Ratio, Mix Density, Solids Loading, O/F Ratio, and %TMD. This is from the mix sheet for batch 42.

Appendix E: Fiber Optic Break Wire Burning Rate Measurement Technique

Image analysis of video captured by a Photron FASTCAM SA4 and a multiple break wire configuration was developed with help from Ramirez [81] to measure the propellant burning rates. For testing with IH, the magnetic field interferes with traditional fine-gauge lead break wires; a novel approach using 0.7mm PMMA fiber optic wires to measure burning rates in the induction coil section was attempted. For the fiber optic break wire, a halogen lamp coupled to the fiber optic to transmit light through the fiber into a ThorLabs DET 210 photodetector. Five total break wires measured the burning rate of the propellant; two lead break wires (1, 2) outside the coil provided a nominal burning rate, while three fiber optic break wires (3-5) provided an induction heated burning rate (Figure E.1).

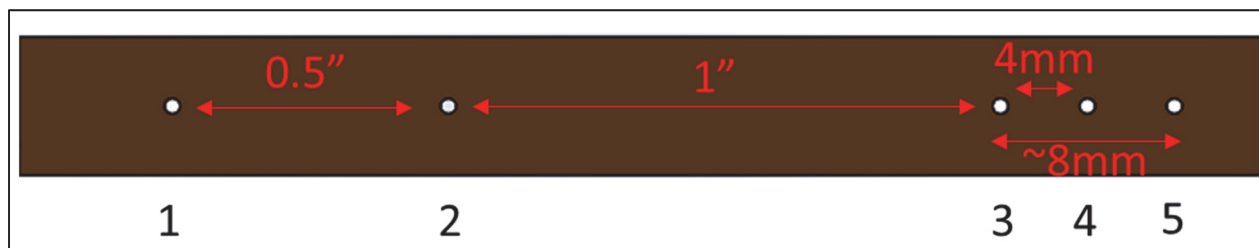


Figure E.1: Propellant strand burning rate configuration.

A LabVIEW program with data acquisition and electrical interfaces was developed to enable the control of the induction heater while monitoring lead and fiber optic break wires. Burning rate tests of Advanced Solid Rocket Motor (ASRM) [82] propellant samples were performed to validate the experimental setup. A Photron FASTCAM SA4 high-speed camera was used to track the burning rate visually and confirm break wire operation. While the fiber optic break wires operated as expected, the standard deviation between the burning rate in the fiber optic section was too significant compared to the lead break wires (Figure E.2). The propellant burning rate using lead break wires is 1.129 ± 0.036 mm/s, whereas the propellant burning rate using fiber optic break wires is 1.298 ± 0.213 mm/s. An explanation for this is that the diameter of the fiber optic break wires is too significant (0.7mm); not only is it on the order of the propellant burn rate, but it is also contributing to changes in the oxidizer-to-fuel ratio. The lead break wires have a diameter of 0.26mm, resulting in a cross-sectional area 86% smaller than the fiber break wires. The optical data from the Photron FASTCAM confirmed break-wire operation but also validated the induced error in the measurement from the fiber wires. It is proposed that fiber optic break wires could accurately measure the burning rate if they have a smaller diameter are used.

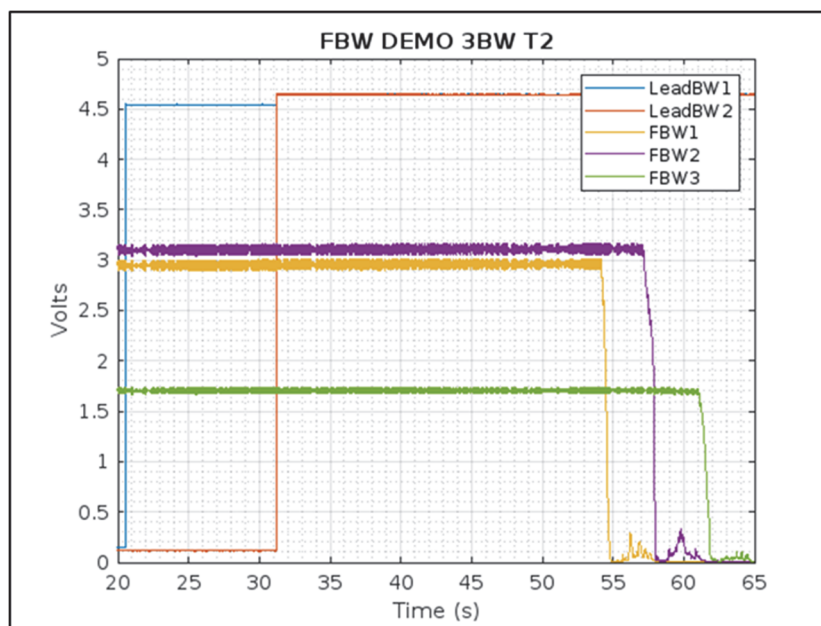


Figure E.2: Response from break wires captured by LabVIEW. The lead break wires show high signal when broken and the fiber optic wires show a low signal when broken.

Thinner fiber optic wires could not be acquired in time to complete testing for this study, so other methods were used to characterize the burning rate. A second method using the 0.7mm fiber optic wires was attempted. The fiber optic break wires were mated to the propellant strand surface rather than run through the sample. The idea was that when the propellant strand was burning, the light emission from the flame front would provide a light source that would flow through the fiber optic wires to the photodiode and would serve as a time stamp. However, the strands could not pick up a valid signal due to charring of the inhibitor halocarbon grease on the edge of the sample. The final decision was made to only measure burning rate optically with the Photron FASTCAM.